UAB
Universitat Autònoma de Barcelona

Cost-effective electrochemical heavy metal sensors in environmental monitoring and healthcare: from *in-situ* monitoring to a wearable format

Qiuyue Yang

Ph.D. Thesis

Ph.D. in Material Science

Director:
Prof. Arben Merkoçi

Department of Chemistry

Science Faculty

2022

1.3 Electrochemical Sensors for *In-situ* Heavy Metal Measurements and Interference Issues

1.3.1 *In-situ* HMIs Detection by ASV in Environmental Monitoring and Healthcare

With the increase of industrialization and urbanization, water pollution becomes one of the most concerning issues. In particular, heavy metal pollution is a worldwide concern, posing the risk on public health and the ecosystem. Heavy metal ions (HMIs) primarily originate from anthropogenic wastes such as industrial wastes, agricultural wastes, sewage, *etc.* Also, HMIs are released from natural events such as weathering of metal-bearing rocks, volcanic eruptions, *etc.*[185] The HMIs can transfer into water sources from these sites, and may cause a wide dispersion in the environment.[186] One infamous example occurs in the Los Frailes mine in Seville Province in Spain, in 1998. A big amount of mine tailing suspension ($\sim5\times10^6$ m^3) was accidentally discharged due to the burst of the holding dam. Multiple HMIs at the dangerous concentration level quickly contaminated nearby rivers and traveled through waterways for 40 km in length. The removal of HM pollutants costs three years and €240 million approximately. Despite this, the catastrophe harms the vulnerable ecosystem of Doñana. Even now, some alluvial aquifers close to the mine tailing pond are still polluted by HMIs such as Al^{3+}, Cd^{2+} and Zn^{2+} ions, which flow into nearby streams and surface water.[187]

Once released into the environment, HMIs are able to accumulate in soil and surface water but they are not biodegradable.[188] Therefore, they can be retained in the ecosystem persistently. Furthermore, HMIs are reported to adsorb on the surfaces of microplastics, resulting in the deterioration of microplastic pollution at this stage.[189] Additionally, HMIs could also induce antibiotic resistance of pathogenic microbes in natural waters, which may further pose the risk to public safety.[190] Apart from these negative effects on the environment, HMIs are harmful to human health upon extensive intake (Figure 1.3.1a). HMIs can accumulate in human bodies *via* the food chain, disrupt intracellular homeostasis and induce oxidative stress which is a state that the generated reactive oxygen species (ROS) overwhelms body antioxidant protection and thus causes damage to lipids, proteins, enzymes, and DNA.[191] Further, quenching ROS can inhibit the activity of enzymes (catalase, peroxidase, and superoxide dismutase) in human bodies, which may cause intellectual disabilities in children, dementia in adults, central nervous system disorder, *etc.*[192,193]

As such, the maximum contaminant levels of diverse HMIs have been carefully defined for drinking water by several organizations. In Table 1.3.1, the guidelines recommended by the World Health Organization (WHO) and Environmental Protection Agency (EPA) for HMIs in drinking water are summarized based on the correlated scientific studies for toxicity.[194–196]
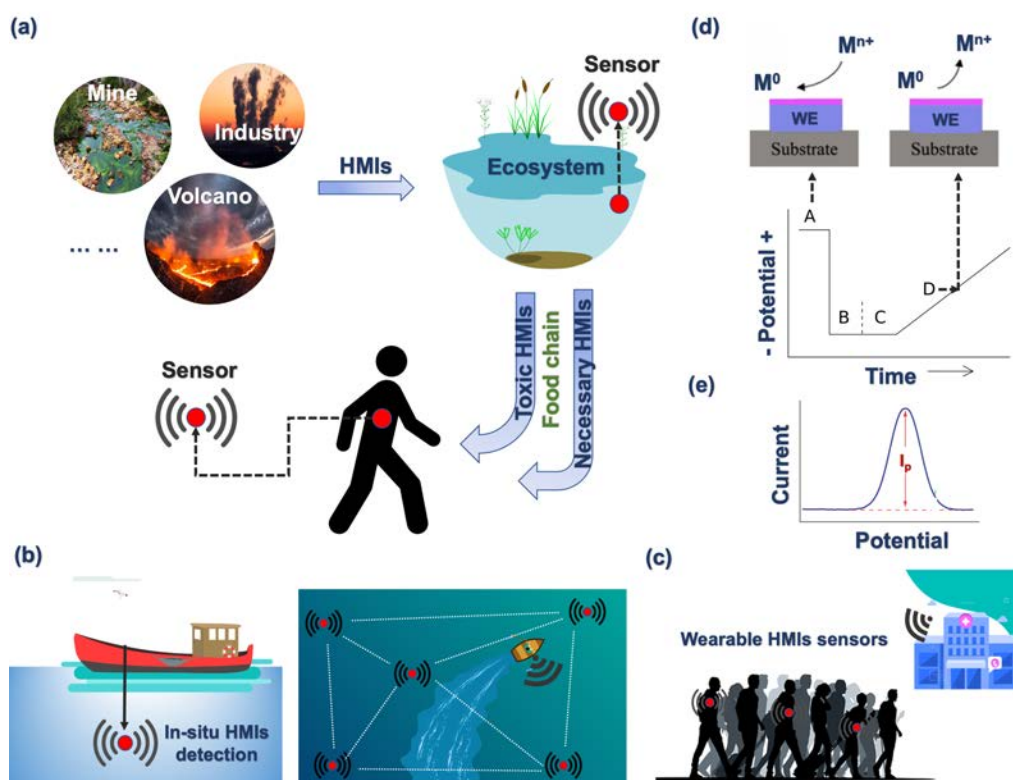
Figure 1.3.1. Schematic illustration of (a) HMIs accumulation in the ecosystem and human body, *in-situ* sensor/sensing network constructed for (b) environmental monitoring and (c) healthcare. (d) The working principle of ASV and (e) obtained voltammograms.

In Table 1.3.1, some of the HMIs are found highly toxic such as Hg^{2+}, Cd^{2+} and Pb^{2+}, which have extremely low maximum contaminant levels (at ppb level). On the other hand, certain HMIs (*e.g.*, Cu^{2+} and Zn^{2+}) are nutritionally necessary for health in a small quantity; thus, a higher maximum contaminant level (at ppm level) can be tolerated. However, the extensive intake may cause severe diseases. For example, Cu^{2+} ions play an important role in forming red blood cells, and maintaining nerve cells and the immune system.[197] The amount of Cu^{2+} acts as an indicator in the diagnosis of rheumatoid arthritis,[198] Wilson's disease,[199,200] and liver cirrhosis.[201–203] Furthermore, Cu^{2+} and other heavy metals in sweat show important variations related to physical exercise, heat stress, and diet.[201–204] The Cu/Zn ratio may also be correlated to coronary heart disease,[32] and extensive Cu^{2+} ions may cause hepatitis, liver cirrhosis, jaundice, and hemolytic crisis.[192]

Table 1.3.1 The maximum tolerated HMIs concentration in water

Metal	WHO (ppm)	EPA (ppm)
Ni^{2+}	0.07	0.04
Cu^{2+}	2	1.3
Zn^{2+}	3	5
Cd^{2+}	0.003	0.005
Hg^{2+}	0.001	0.002

Pb^{2+}	0.01	0.015
As^{3+}	0.01	0.01
Sb^{3+}	0.02	0.006

Given the risk of HMIs in the ecosystem and health, it is critical to detect trace HMIs in the environment under their maximum contaminant level and to monitor HMIs in biofluids to prevent extensive intake or exposure. Accordingly, *in-situ* sensing networks in natural waters are highly needed for environmental monitoring (Figure 1.3.1b). Also, wearable HMIs sensors to provide information for public hospitals are useful for the prognosis of certain potential diseases (Figure. 1.3.1c).

Standard techniques for HMIs detection (*e.g.*, ICP-MS) feature high sensitivity, accuracy and specificity for the analytes as low as part per trillion (ppt) level.[194] However, they require long-testing time, complicated sample pretreatment, professional personnel, and expensive and bulky equipment in laboratories. For example, to monitor the concentration of HMIs in natural waters, the conventional method, so-called spatial distribution, typically involves 1) high cost of human labor, complicated manual operation, 2) inaccurate results originating from the additional storage and transfer of samples to laboratories. Improper storage and transfer may change HMIs configurations which are sensitive to the change in pH, UV exposure and temperature.[205] With the increasing demand for *in-situ* sensing networks as discussed in Chapter 1.1, user-friendly or even fully automatic sensing strategies are preferred; however, these standard techniques cannot satisfy this preference.

Exploration of new sensing techniques with rapid and simple measurements has been ongoing. In particular to low-cost sensors, their use is expected to spread throughout resource-limited regions. Accordingly, electrochemical sensors become good candidates due to their low cost together with rapid tests, high portability and simplicity as discussed in section 1.2. Even more excitingly, many studies have shown that the fabrication of electrochemical sensors is compatible with printing techniques and nanomaterials, which further decreases the sensing cost and enhances their sensing performance.[194]

Amongst various electrochemical sensing techniques, the stripping voltammetry is able to detect multiple HMIs simultaneously with high sensitivity and simplicity. It is a collection of electrochemical techniques including anodic stripping voltammetry (ASV), cathodic stripping voltammetry (CSV), and adsorptive stripping voltammetry (AdSV). ASV is regarded as the most used technique to detect HMIs.[206]

ASV primarily consists of two steps (Figure 1.3.1d): 1) Deposition step: A negative constant potential is applied on the working electrode so that HMIs are reduced and deposited on the surface of the working electrode; 2) Stripping step: the reduced heavy metals are oxidized/stripped by a released potential to zero. The released potential is in a specific waveform such as linear sweep, staircase sweep, differential pulse sweep, and square-wave

sweep. Meantime, the potential and current are recorded, generating a voltammogram where an oxidative peak provides information of HM species by peak potential (Figure 1.3.1e). To obtain quantitative results, the calibration is established between concentrations and the oxidative peak current or area in the voltammogram. As such, when the sensor is tested with an unknown solution, the concentration can be determined by the fitted calibration curve.

Based on its working principle, detecting HMIs by ASV is found to match most of the criteria for *in-situ* measurements (proposed by J. Holmes et al.), namely high sensitivity, high selectivity, high testing speed, continuous testing ability, the safety of sensing materials and portability.[207]

First, in terms of high sensitivity, the LOD *via* ASV has been reported down to ppt level.[208] The high sensitivity is derived from the deposition step, in which the target HMIs can be pre-concentrated on the surface of the WE effectively by trading off a small amount of testing time.

Second, good selectivity is possible to achieve by ASV, for the oxidative peak are typically discrete, which potential can be corresponding to different HMIs species. By tuning deposition potential, target HMIs with interest can be identified. However, in practical use, mutual interference between multiple HMIs may influence the selectivity *via* peak splitting or overlapping, which brings troubles to identification and quantification. The state-of-art solutions will be discussed in the next section of 1.3.4. Fortunately, the alkali metal ions *e.g.* Na^+, K^+, Ca^{2+}, Mg^{2+} commonly appearing in natural waters and biofluids, have minimal interference on the sensing signals by ASV.[209,210] It can be attributed to the difficulty of depositing alkali metal ions requiring much more negative potential than typical HMIs such as Cd^{2+}, Cu^{2+}, and Hg^{2+}.[211]

Third, ASV techniques typically offer a rapid detection of HMIs. The deposition time ranges from 60 to 300s, and the quiescent and stripping time is minimal.[212] This feature is useful for *in-situ* investigation of natural waters, whose aqueous chemistry can change from minute to minute dynamically, responding to natural tides, storms and effluent discharges.[207]

Moreover, long-term stability for continuous monitoring can reduce the cost and inconvenience of replacing electrodes. In this sense, inert carbon-based electrodes can be reused for decades times. Compared to metallic materials (such as Bi, Sn, Hg, and Sb) which may form amalgam and alloy during depositing, inert carbon materials could sustain in reused cycles with better stability.[213]

Additionally, the ASV technique allows for high portability with the development of microfabrication in the past few years as we discussed in section 1.2.2, which facilitates its use in *in-situ* measurements. The fabricated micro/nanoelectrodes possess low IR (voltage) drop and high signal-to-noise ratio, which are able to detect HMIs in the original sample at low ionic strength without requiring any additional supporting electrolytes.[47] In particular,

printing planar electrodes in the micro or even nanoscale range further boosts their application in *in-situ* systems.[207] Also, the associated sensing system including potentiostat, battery, wireless communication module, *etc.*, tend to be more integrated. An ideal format is a wearable device, which has been reported to be worn on the skin for the detection of HMIs in sweat.[214] Therefore, electrochemical sensors using ASV seem to satisfy most criteria of *in-situ* HMIs measurements.

However, it is noteworthy that *in-situ* HMIs sensors should exclude manual sample collection, which is the imperative difference from on-site and field-deployable measurements. Necessary functions based on ASV's working principle, such as sampling, pretreatment (*e.g.*, filtration) and mixing with supporting electrolytes must be integrated into a sensing system and can be realized in an unmanned way. Accordingly, a fluidic sensing system has been commonly used to control testing solutions and supporting electrolytes in its channels. With the assistance of embedded sensing probes and a potentiostat, it can transmit commands and signals to users.[215]

With this aim, we review the studies about electrochemical *in-situ* HMIs detection operated by ASV in both environmental natural waters and biofluids.

1.3.2 State-of-Art Studies of *In-situ* HMIs Detection in Environmental Monitoring

The studies of *in-situ* heavy metal sensors by ASV are summarized In Table 1.3.2. As expected, most of the studies are carried out by fluidic systems *e.g.*, flow/sequential injection analysis (FIA/SIA) and batch injection analysis (BIA). In FIA and SIA, the sample is injected into a hydraulic system and forced (by syringe, peristaltic pump, *etc.*) to be processed on its way to the sensor mechanically. With the use of multiple port valves based on FIA, SIA allows the complicated handling of multiple samples and reagents in one device (Figure 1.3.2).

Table 1.3.2. The studies of *in-situ* HMIs sensors by ASV

Electrode	Fabrication techniques	Targets	LOD (ppb)	Deposition time (s)	Technique	Platform	REF	Other
Bi-film GCE	Electroplating	Cd^{2+}	2	180	SWASV	FIA	216	Simultaneous detection
		Pb^{2+}	1					
Nafion-coated Bi film on GCE	Electroplating	Zn^{2+}	2	160	SWASV	FIA	217	Simultaneous detection
		Cd^{2+}	2					
		Pb^{2+}	6					
rGO-coated Au electrode	Spin coating and screen printing	Pb^{2+}	4	240	SWASV	BIA	218	Simultaneous, Including pretreatment of sediment
Hg-plated Au microelectrode	Photolithography	Zn^{2+}	3.4	150	DPASV	FIA	219	Simultaneous detection
		Cd^{2+}	0.2					
		Pb^{2+}	0.5					
		Cu^{2+}	1.8					

Electrode	Fabrication techniques	Targets	LOD (ppb)	Deposition time (s)	Technique	Platform	REF	Other
Bi microelectrode	Photolithography	Cd^{2+}	9.3	90	SWASV	Microfluidic system	220	Individual detection, Customized readout circuits
		Pb^{2+}	8	60				
Au microelectrode	Photolithography	Hg^{2+}	3	120	DPASV	Microfluidic system	221	
AuNPs and Au nanofilaments electrodes	Photolithography	Hg^{2+}	3	600	SWASV	Submersible probe	222	Field validation
Bi/Nafion modified carbon electrode	Screen printing	Cd^{2+}	0.79	100	SWASV	FIA	223	Automatic cleaning
Au SPE	Screen printing	Pb^{2+}	4	90	SWASV	BIA	224	Simultaneous detection
		Cu^{2+}	2					
		Hg^{2+}	4					
Graphite foil electrode	Cutted by craft cutting printer	Cd^{2+}	6	180	SWASV	Paper fluidic system	225	Simultaneous detection
		Pb^{2+}	6					
Carbon electrode	Screen printing	Pb^{2+}	7	120	SWASV	Paper fluidic system	226	Individual detection
		Cd^{2+}	11					
Carbon electrode	Screen printing	Pb^{2+}	0.5	230	SWASV	Microfluidic system	227	GO-PDMS for adsorption/accumulation
Bi electrode	Photolithography	Zn^{2+}	0.08	120	SWASV	Microfluidic system	228	Field validation
Hg-film GCE	Electroplating	Pb^{2+}	-	180	DPASV	FIA	229	Field validation, All-in-one sensing machine
		Cu^{2+}	-					
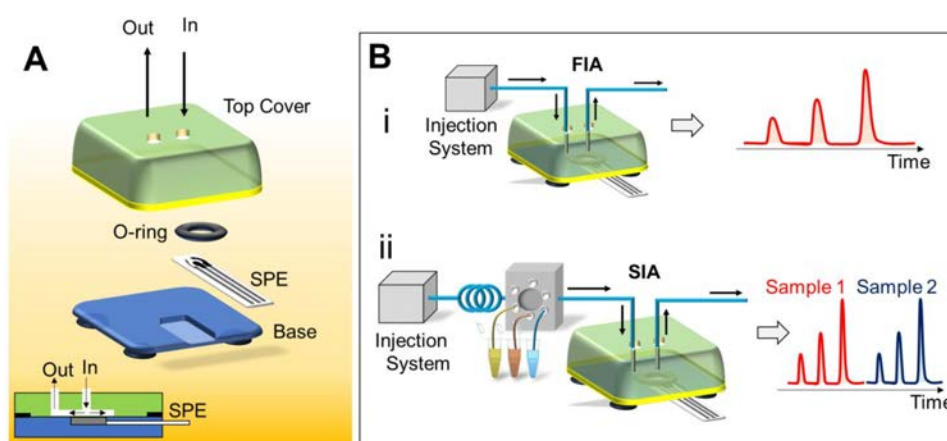
Figure 1.3.2. (a) Schematic illustration of the flow cells used in FIA and SIA systems. (b) Illustration of the basic working principle of (i) FIA and (ii) SIA systems. The sample is introduced into the flow stream using an injector (left) and the corresponding signal is recorded over time (right).[230]

An exemplary study reported an automatic sensing system to detect Cd^{2+} ions in natural water samples.[223] Henríquez et al. fabricated a testing loop based on FIA consisting of a flow cell

(with an embedded electrode), a potentiostat, multiple channels, a pump and several valves to control the testing solution. This system further enhanced the sensing signal of Cd^{2+} ions, for the continuous flow of testing solution renders more HMIs to preconcentrate on the electrode in the deposition step than in the static system. Besides, the FIA system realized multiple functions such as mixing, *in-situ* plating Bi film on the electrode and cleaning between measurements. This study demonstrates the merits of using a fluidic system— automatic sample extraction and sensing, showing great potential for *in-situ* HMIs detection.

In practical use, the access to the natural environment (*e.g.,* lake, river) is inconvenient to operate *in-situ* measurements, which always requires automobiles with human labor on deck. As shown in Table 1.3.2, although most reported sensing systems were portable and able to extract samples and sense HMIs automatically, they were operated in laboratories or in the field with the lack of field validation for this reason.

To solve this issue, Tercier-Waeber et al. proposed a submersible sensing probe equipped in a boat to detect Hg^{2+} pollution in seawater by a gold-based microelectrode array.[228] Field validation was successfully performed in Arcachon Bay in France. However, this study still involved trained personnel on deck to assist in the measurement. Hence, to further eliminate the involved manual processes, Wang et al. presented an unmanned kayak to detect Zn^{2+} in seawater based on a microfluidic system, where a liquid crystal polymer-modified Bi electrode was embedded. The kayak was driven to measure Zn^{2+} in seawater under the commands of an operator *via* remote control. However, some issues remained such as poor portability of the kayak, high reliance on the operator, and sensing instability caused by the bubble issue in the fluidic system.

In summary, even though many publications have presented innovative sensing systems for HMIs detection based on FIA, SIA and BIA, field validation has rarely been reported for environmental monitoring. Particularly, the fully unmanned vehicle equipped with an automatic, portable and robust sensing system has never been reported as far as we know. Besides, the fabrication of most electrodes in Table 1.3.2 relies on cleaning-room techniques, which could be altered by other low-cost methods. Moreover, the electrodes' sensing materials are metals *e.g.*, Au and Bi with good affinity to HMIs; however these metals result in high cost of fabrication, possible recycling issues, and limited repeatability caused by the formed alloys with electrode material in the deposition step. Additionally, sustainable sensing platforms, for example, paper-based fluidic sensors are emerging.

1.3.3 Wearable Devices for HMIs Detection in Sweat for Healthcare

Apart from environmental monitoring, HMIs also play important roles in physiological reactions in the human body, and thus, several point-of-care sensing devices for the detection of HMIs in sweat and urine have been reported.[33,210,231,232] Amongst those sensors, the HMIs sensor in a wearable format offers a user-friendly, convenient and potential real-time

detection for the prognosis of certain diseases and the risk evaluation under extensive HMIs exposure.

As the definition of a wearable sensor indicates, a wearable sensor should be worn on the surface of the human body targeting non-invasive sampling. Interstitial fluid, tears, and sweat are typical samples for wearable sensors. In particular to sweat, it is abundant with simple composition, containing many biomarkers for pathologies, which has been utilized to be tested in wearable sensors.[233–239] Electrochemical sensors have been reported to detect the biomarkers in sweat such as electrolyte ions, bacteria, and hormones.[240] However, only a few publications about wearable electrochemical sensors for HMIs detection in sweat have been presented.

An exemplary study was presented In 2016. Gao et al. reported Au and Bi microelectrodes fabricated by photolithography to detect Zn^{2+}, Cu^{2+}, Cd^{2+}, Pb^{2+}, and Hg^{2+} cations in sweat simultaneously. Thanks to a microchamber where the sensing microelectrode was embedded in a wristband, sweat samples were collected from the glands, stored and tested (Figure 1.3.3a-c). The on-body HMIs detection in real time has been performed successfully lastly (Figure 1.3.3d). In this sensing system, a commercial potentiostat was employed, which is not either portable or conformable to be wearable.[214]
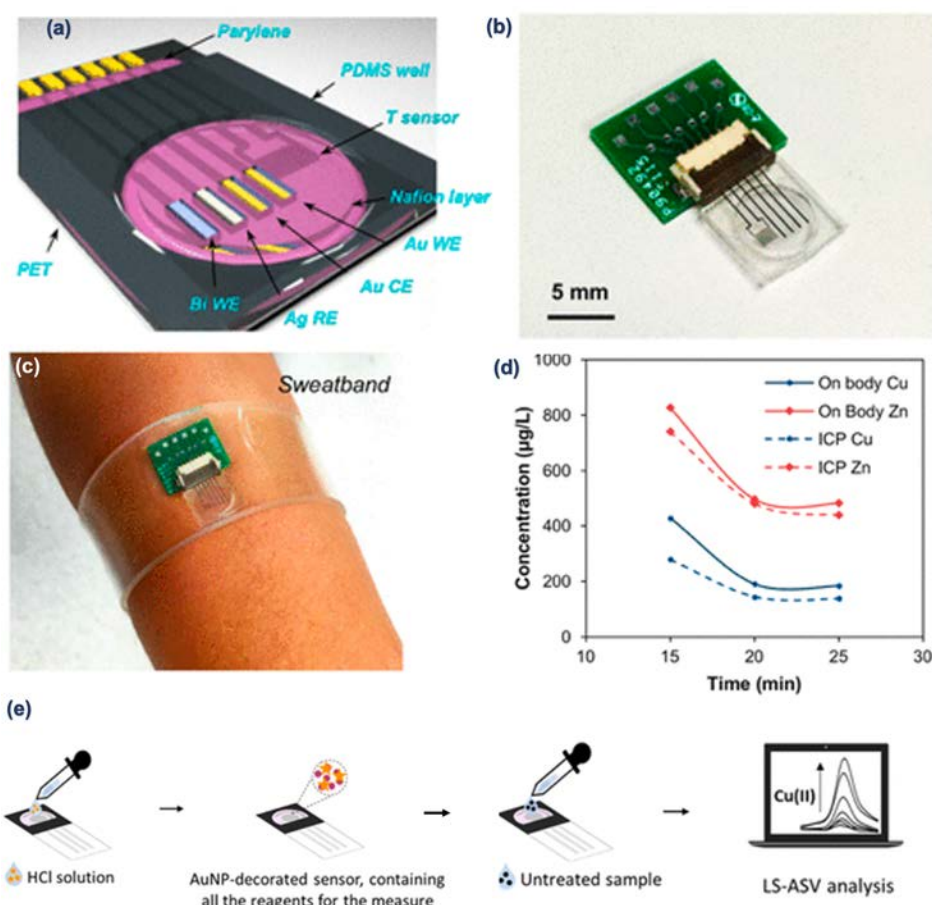

Figure 1.3.3. Wearable electrochemical sensors to detect Cu^{2+} and Zn^{2+} in sweat: (a) Schematic of wearable sensing electrodes including a T-sensor(temperature sensor). (b) Digital photo of

the wearable sensor with its connector and (c) sweatband where wearable sensor embedded. (d) Validation of wearable sensor tested on skin with the reference of ICP-MS.[214] (e) Paper-based reagentless electrochemical sensor to detect Cu^{2+} in sweat. [241]

Unlike the previous study of using a microchamber to guide the tested sweat, Bagheri et al. proposed an approach of AuNPs decorated paper for highly sensitive detection of Cu^{2+} ions in sweat and serum based on the SWASV technique. The disposal paper fluidic system was patterned by hydrophobic wax that was printed by the wax printing technique. The three-electrode system was created by screen printing carbon ink (as the WE and CE) and Ag/AgCl (as the RE). Besides, the reagents for measurements were pre-stored in the paper so that the real sample was tested directly without any treatment (Figure 1.3.3e). The system was able to detect Cu^{2+} ions with LOD of 3 ppb and a linear range up to 400 ppb. The recovery was between 93% and 101% in the spiked sweat. Most interestingly, due to the nature of cellulose, the testing paper is sustainable for the environment. Despite these very promising characteristics, this system has a similar problem of integration and conformity, lacking a wearable readout system.[241]

Additionally, sampling sweat in most presented sensing platforms relied on passive sweat excretion which requires subjects to stay in high-temperature condition or do physical exercises. The volume of sweat is not constant and difficult to be controlled, and it is different from subject to subject. Besides, the sweat volume at a specific time, namely sweat rate, could unproperly dilute or concentrate the target HMIs,[242] but the normalization of sweat rate has not been complemented in the presented studies in wearable HMIs sensors.

In 1.3.2 and 1.3.3, we briefly introduced the state of the art of *in-situ* HMIs sensors/sensing systems by ASV applied for environmental monitoring and wearable HMIs sensors in healthcare. Besides the remained issues that we discussed above, HMIs measurements by ASV also face open issues: the interference from other targets (mutual interference) and the sample matrix. It is even more challenging to solve them for *In-situ* measurements which require direct sampling from natural waters or biofluids with minimal sample treatment. Hence, herein we focused on the strategies to eliminate mutual interference and sample matrix interference in section 1.3.4.

1.3.4 Mutual Interference Issues of Multiple HMIs

1.3.4.1 Issues of mutual interference: the cause and appearance

Mutual interference is a common problem when detecting multiple species of HMIs by ASV. It is generally considered to be caused by the formation of intermetallic compounds or alloys, and the competition of target ions during the deposition step (shown in Figure 1.3.4a-c). All the HMIs targets are expected to be reduced to their elemental metals in the deposition step, but in fact, they also form alloys or intermetallic compounds. For example, Cd^{2+} and Cu^{2+} are known to form their alloy on the surface of boron-doped diamond electrodes (BDD) when co-

depositing.[243] Moreover, metallic electrodes could form alloys or intermetallic compounds with target HMIs similarly, which is frequently believed to provide high sensitivity to HMIs;[244] however, in some cases, the stripping peak of the metallic sensing material has a close potential to the one of target HMIs, resulting in two overlapping stripping peaks corresponding to target analytes and electrode's material. For example, bismuth (Bi) electrodes are reported difficult to detect Cu^{2+} ions for this reason.[245] Additionally, ions' competition also contributes in mutual interference, which frequently occurs when using unmodified carbon-based electrodes (*e.g.* SPCEs) due to their limited surface area and heterogeneous nature.[108]
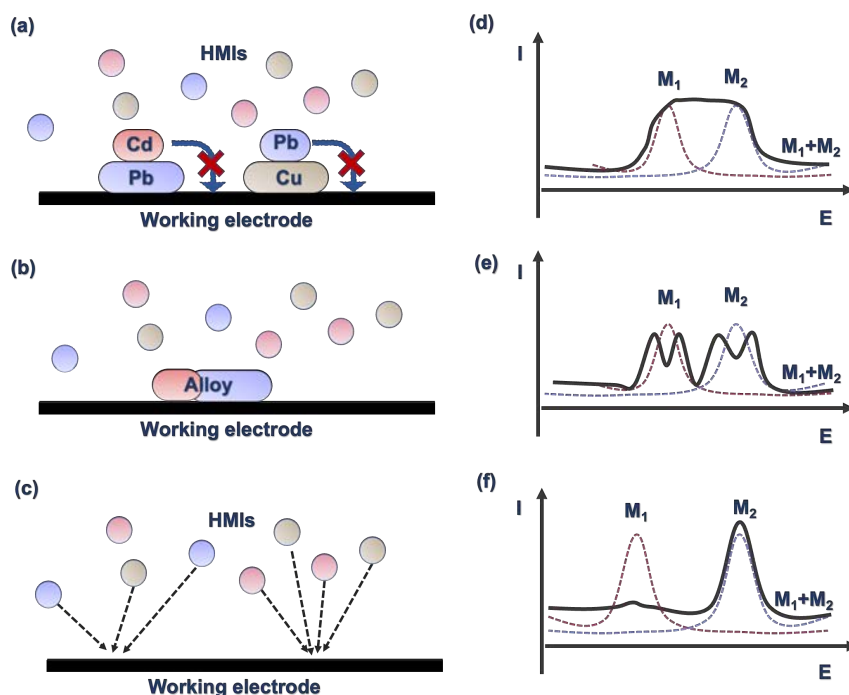

Figure 1.3.4 Schematic illustration of mutual interference caused by the formation of (a) intermetallic compounds and (b) alloys, and (c) ions competition. Typical phenomena of (c)peak overlapping, (d)splitting, and (e) sensing signal loss.

Mutual interference results in two main problems in the simultaneous detection of multiple HMIs 1) the problem of identifying target HMIs due to the shift, overlap, and split of HMIs' oxidative peaks (Figure 1.3.4 d,e); 2) the problem of quantification, attributed to the changed peak intensity/area by the varied ratio of other HMIs' concentrations—a variation in the concentration of one type of HM may lead to a variation in the response of the others. In the worst case of the latter problem, the sensing signal of a specific HM could be diminished (signal loss) by the presence of others, making it impossible to detect HMIs even at their dangerous level (Figure 1.3.4f). It frequently happens to carbon-based electrodes detecting the HMIs requiring more negative deposition potential such as Zn^{2+} and Cd^{2+}, with the presence of HMIs with less negative deposition potential such as Pb^{2+}, Cu^{2+}, and Hg^{2+}.[246-248] A study proposed an explanation that the former HMIs (*e.g.* Zn^{2+} and Cd^{2+}) tend to deposit on the surface of the latter ones (*e.g.*, Pb^{2+} and Cu^{2+}) besides on the surface of the electrode

surface, consequently, the substance loss of the former HMIs is induced by the stripping step.[243] In Figure 1.3.4 a, Cd^{2+}, Pb^{2+}, and Cu^{2+} ions are used to be demonstrated based on it.

Due to the toxicity of Hg, the use of HMDEs is eliminated; instead, carbon-based electrodes such as GCE, BDD, and SPCEs are favorable in the recent decade.[108,246,249] However, compared to HMDEs or other metallic film electrodes, mutual interference is severe for carbon-based electrodes, attributed to less affinity of HMIs to the surface of carbon electrodes. Hence, the state-of-art strategies to address mutual interference are summarized below, with a special focus on carbon-based electrodes.

1.3.4.2   State-of-art strategies for addressing mutual interference effects

1)   Algorithm and mathematical analysis

The peak overlapping issue shows a merged and broad peak rather than discrete peaks, which cannot be identified. To overcome it, a mathematical transformation can be employed to deconvolute the broad peak as several separate peaks. More efficiently, the artificial neural network (ANN) including the input, hidden and output layers is trained to recognize the HMIs' species and determine the concentration automatically in Figure 1.3.5. The input layer of ANN is responsible for collecting the data to create a data space obtained from standard heavy metal solutions with known concentrations and various combinations. The hidden layer renders the collected data get processed through a specific algorithm such as principal component analysis (PCA), discrete Fourier transform, wavelet transform (WT), *etc*. The output layer decides how to proceed based on the hidden layer so that the simultaneous quantification of metal species can be achieved.
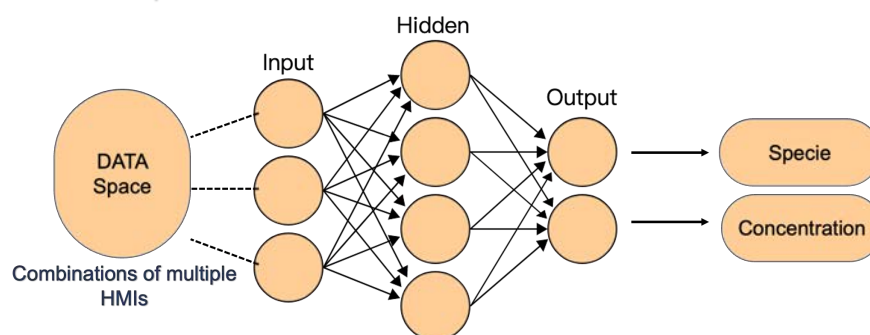

Figure 1.3.5. Schematic illustration of typical artificial neural networks for HMIs detection

Based on it, a study reported by Gutierrez et al. shows an example using an algorithm to reduce the interference of peak overlapping. Because the oxidative peaks of Tl^+ and In^{3+} had similar peak potentials with the one of Cd^{2+}, when these three species of cations co-existed in the same solution, the overlap of peaks influenced the recognition of Cd^{2+}. However, the presented algorithm successfully detected Cd^{2+}, Pb^{2+}, and Cu^{2+} with the existence of Tl^+ and In^{3+}, only using graphite-epoxy composite electrode without any chemical modification. Wavelet neural network was employed, in which the hidden layer used nonlinear wavelet basis functions in order to achieve a good recovery. In the validation step, the quantification

of Cd^{2+}, Pb^{2+} and Cu^{2+} even at the sub-ppm level was able to be determined with the interference of Tl^+ and In^{3+} with the uncertainty below 5%.[250]

Besides addressing the peak overlapping issue, mathematic models can also alleviate the inaccuracy of varied sensing signals by different HMIs' species and ratios of HMIs' concentrations. Machine learning and deep learning have been widely used in this case, to be trained by abundant data collected from different combinations of concentrations and species.[251–253] In this way, the quantification is more accurate.

Liu et al. reported a mathematic model to improve the accuracy when detecting Cd^{2+}, and Pb^{2+} with the presence of Cu^{2+} and Zn^{2+} as interferents by machine learning.[252] In this study, the 2-D correlation spectroscopy method, which is typically used for spectroscopy analysis, was employed to analyze the obtained voltammograms. It gained insight into the change of peak currents, acquired from various HMIs with different combinations of concentration ratios. The current intensity of identified oxidative peaks was used as the feature in the training process of two machine learning models, namely, Feature-RF (Random Forest) and Feature-SVR (support vector regression) models. Consequently, this method was validated to detect Cd^{2+} and Pb^{2+} in a soil extract solution, which achieved a recovery of nearly 100% compared to the gold standard method of ICP–MS as a reference.

2) *Chemical modification of carbon-based electrode by nano/micro materials*

The WE has a great impact on the sensing performance of HMIs, for its interface controls the deposition of target analytes, and thus functionalizing the WE surface is effective to improve sensing capabilities.

Unlike the mathematical strategy to address the peak overlapping issue and improve accuracy, chemical modification aims to recover the diminished sensing signal/sensitivity by mutual interference, which cannot be solved by algorithms. With this aim, two strategies are typically found in literature: 1) one is to enhance all the sensing signals of target HMIs, and 2) the other is to improve specific selectivity toward one HM that suffers from diminished sensitivity. Modifying nanomaterials on WE can achieve both due to its high surface-to-volume ratio, fantastic catalytic properties, and tunable interface chemistry (in section 1.2.3). Generally, two types of nanomaterials have been used for chemical modification: 1) using elemental metals, mainly post-transition metals (Figure 1.3.6 a-c); 2) non-metallic materials such as carbon-based materials or organic materials enriched in S, N, F and O (Figure 1.3.6 d). Post-transition metals (e.g, Hg, Bi, Sn, and Sb) feature low melting temperatures and have relatively weak metallic bonds, which facilitates the formation of their alloys with target HMIs (Figure 1.3.6b).[206] For example, Hg is the most famous to enhance HMIs detection based on the reactions:

$$Hg + M^{n+} + ne^- \rightarrow M(Hg) \qquad (1.1)$$

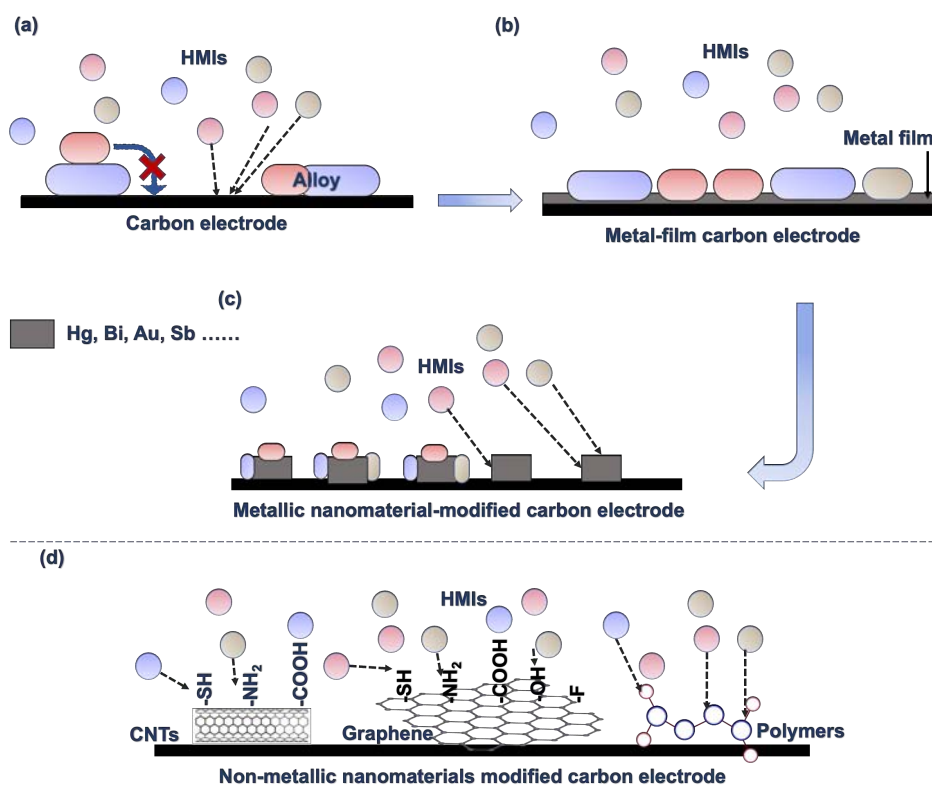$$M(Hg) \rightarrow Hg + M^{n+} + ne^- \qquad (1.2)$$
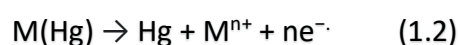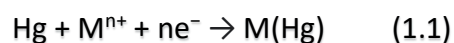
Figure 1.3.6. Schematic illustration of mutual interference occurs on the surface of (a) carbon-based electrodes, (b) metallic film modified electrodes, (c) metallic nanomaterials modified electrodes and (d) non-metallic nanomaterials modified electrodes.

As such, great enhancement of sensitivity can be achieved *via* reducing intermetallic compounds on carbon-based electrodes (Figure 1.3.6a). Besides, the higher surface area of nanomaterials may increase the adsorption of HMIs and reduce the ions' competition. (Figure 1.3.6b) To date, diverse morphologies of nanomaterials such as nanowires, nanoparticles, nanostars, and their corresponding composites have been reported to alleviate mutual interference.[206]

a. Metallic nanomaterials and their composites

Hg is typically electroplated on the carbon-based electrode to substitute for traditional HMDE.[254] Due to the deposited Hg film, the modified carbon-based electrodes have similar features to HMDE, and thus reduce the effect of mutual interference.[255,256] Due to the higher surface area, Hg nanoparticles can reach the same performance as the deposited Hg film but only require a much smaller amount as Laia et al. reported.[257] They presented a new synthesizing approach of Hg nanoparticles assisted by polydiallyldimethylammonium chloride (PDDA). The synthesized composite was dropcasted on the working surface of SPCE. Better sensitivity to Cd^{2+}, Pb^{2+}, and Cu^{2+} ions in the simultaneous detection was achieved by the modified electrode. Also, the diminished sensitivity toward Cd^{2+} of SPCE was found to be recovered. Hg nanoparticles modified SPCE showed anti-interference features, for the

sensitivity toward Cd^{2+} in simultaneous detection of Cd^{2+}, Pb^{2+} and Cu^{2+} (8.4×10^{-4} A/ppm) was almost the same as the one in individual detection of only Cd (5.3×10^{-4} A/ppm).

However, even though the Hg nanoparticles have been proven to alleviate mutual interference with a wide potential window, there is a concern about its toxicity which limits its use.[258]

Bismuth (Bi), as an alternative to Hg, has been used to be deposited on various working electrodes such as a pencil-drawn electrode, SPCE, BDD, and GCE.[259,260] For example, Bi-electroplated GCE has shown the enhanced sensitivity of Zn^{2+} and Cd^{2+}, which reduces the mutual interference influence from Pb^{2+}.[245]

Furthermore, Bi-based nanomaterials are deposited on the WE by sparking processes, dropcasting, and being mixed with the ink of the WE, showing better sensitivity than electroplated Bi film.[260,261] For example, electroplating Bi particles(~100 nm) on GCE was able to effectively enhance the sensitivity toward Zn^{2+}, which was diminished by the presence of Pb^{2+} and Cd^{2+}.[262]

Besides, single-walled bismuth nanotubes (SW-BiNTs) showed their capacity to recover the Cd^{2+} sensitivity that was diminished by the interference of Pb^{2+}(Figure 1.3.7). SW-BiNTs were synthesized *via* self-assembled octa(3-aminopropyl) silsesquioxane (OA-POSS) as nano-templates. The precursor bismuth nitrate ($Bi(NO_3)_3$) was adsorbed on the surface of OA-POSS, followed by the reduction *via* sodium boron hydride ($NaBH_4$). After washing, the achieved slurry of SW-BiNTs was applied on the surface of GCE with Nafion to obtain better adherence. The bare GCE, Nafion-modified GCE, and SW-BiNTs-modified GCE were tested in the mixed solution containing Pb^{2+} and Cd^{2+} (5 μM). The results showed that Cd^{2+} was undetectable by bare GCE, however, SW-BiNTs boosted the Cd^{2+} signal to be observable.[263]
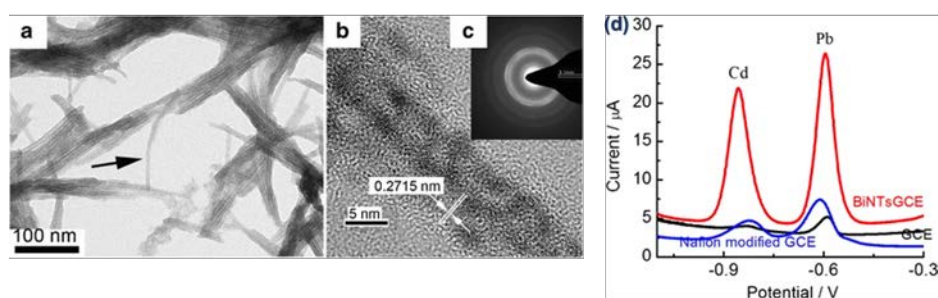
Figure 1.3.7. (a) TEM images, (b) HRTEM photographs, (c) selected-area electron diffraction (SAED) pattern, and (d) stripping voltammograms of bare GCE, Nafion modified GCE and SW-BiNTs modified GCE in a 0.2 M acetate buffer solution (pH 4.0) containing 5 μM of Pb^{2+} and Cd^{2+}. [263]

To realize the mass production of Bi-based nanomaterials modified electrodes, in 2005, an approach of mixing Bi powder with printable carbon paste was presented. Bi particles were mixed with carbon paste and printed as the WE to detect Cd^{2+} and Pb^{2+}. The Cd sensitivity of

SPCE was selectively boosted by the modification of Bi powder. The sensing signal of Cd^{2+} was even better than the one of the screen-printed Bi-metallic electrode.[261]

Even though Bi-modified electrodes seem promising to recover the sensing signal loss of Zn^{2+} and Cd^{2+} with the presence of other metals *via* boosting their sensitivities, Bi-modified electrodes are difficult to detect Cu^{2+} ions which are very common in natural waters and sweat, for the oxidative peak of Bi could overshadow the one of Cu.[245] Additionally, the released Bi^{3+} cations from the working electrode during stripping may react with other analytes in natural water and form insoluble compounds.[263]

Additionally, Au film-modified electrodes are commonly used for HMIs sensing, mainly fabricated by electroplating,[264] sputter,[265], and screen printing.[192] Au-based electrodes are reported to have a good affinity with As^{3+} and alleviate its mutual interference issue.[266] If the stripping peak of interfering metal ions is at a similar potential to the one of As^{3+}, the As^{3+} peak could merge with the interfering peak. In particular to Cu^{2+}, it imposes a serious problem in As^{3+} detection for Cu^{2+} is abundant at a relatively high concentration level in natural waters, causing inaccuracy results.[266] Hence, Au nanomaterials such as AuNPs,[192] Au nanostars,[267] and Au nanoflowers[268] have been harnessed to reduce mutual interference in simultaneous detection.

For example, Au nanostars (shown in Figure 1.3.8a) with a diameter of ~20 nm were modified on the working surface of SPCE to alleviate the peak overlapping issue of As^{3+} and Cu^{2+} when detecting both As^{3+} and Cu^{2+} simultaneously.[267] After being modified with Au nanostars, SPCE was able to detect As^{3+} at 2.9 ppb and its sensitivity was not influenced by the presence of highly concentrated Cu^{2+} (1.3 ppm).
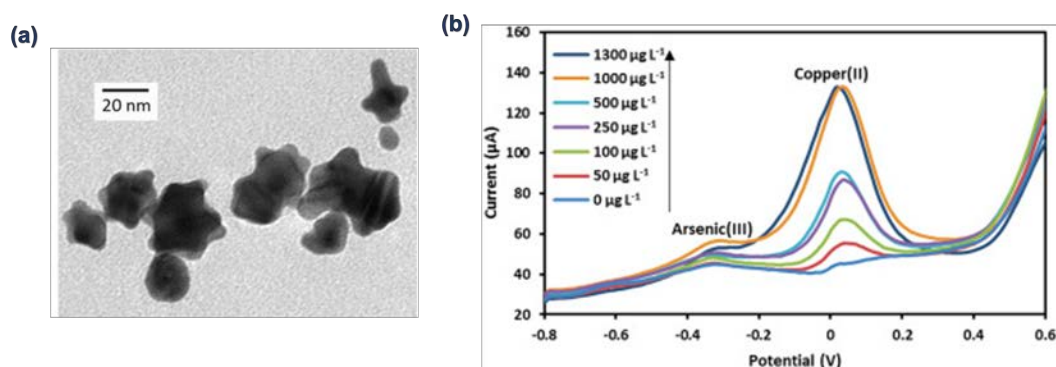
Figure 1.3.8 (a) TEM image of Au nanostars. (b) The stripping voltammograms of Au nanostars modified SPCE when detecting various concentrations of As and Cu simultaneously.[267]

Besides, AuNPs were also reported by Wan et al. to alleviate mutual interference between Cu^{2+} and Pb^{2+} of screen-printed gold electrodes. [192] Bare gold electrodes and AuNPs modified electrodes were tested in the mixed solution of Cu^{2+} and Pb^{2+} (300 ppb). Without AuNPs, the oxidative peaks of Cu^{2+} and Pb^{2+} were broad and ambiguous to be identified; after modification, distinct stripping peaks were achieved. The larger active surface area of AuNPs could be responsible for the promotion of sensitivity and selectivity.

Antimony (Sb) is also one of the commonly used post-transition metals to modify carbon-based electrodes. In 2007, Hocevar et al. firstly utilized Sb film-based electrodes for the determination of HMIs.[269] The Sb-modified GCE and SPCE appeared similar to the ones modified by Bi and Hg, which recovered the diminished Cd^{2+} signal by the presence of Pb^{2+} ions.[248,270] Besides, the deposited Sb film improved the accuracy of GCE toward Hg^{2+}, whose signal was influenced by the presence of Cu^{2+} due to the formation of amalgam. It could be attributed that Sb could form the alloy with Cu^{2+} relatively easier than with Hg^{2+} ions; as such, Hg^{2+} ions formed less Hg-Cu intermetallic compound.[271]

Sb nanoparticles have been reported to enhance the sensitivity of a CNTs electrode toward both Cd^{2+} and Pb^{2+} in simultaneous detection.[272] Consequently, the sensing signal loss of Cd^{2+}, which occurred to the CNTs electrode, was alleviated. In a comparative study, Sb nanoparticles demonstrated more enhancement of the sensitivities than the Sb film-based CNTs, which could be attributed to the higher working surface of nanomaterials. Finally, the Sb nanoparticles modified CNTs electrode can detect down to 0.77 ppb of Cd and 0.65 ppb of Pb simultaneously.

Besides metallic nanomaterials, nanocomposites containing conductive carbon-based nanomaterials and metallic materials have been applied for HMIs detection to reduce mutual interference via enhancing sensitivity. The composites take advantage of the high surface area of metallic nanoparticles and conductive percolated networks of these carbon-based nanomaterials, showing a synergetic effect.[273]

Tan et al. utilized an innovative composite of fluorinated graphene (GraF) and Au nanocages to modify GCE (in Figure 1.3.9a).[274] In Figure 1.3.9b, before modification, GCE cannot detect the unobservable sensing signals of Zn^{2+}, Cd^{2+} and Pb^{2+}, which were diminished by the presence of Cu^{2+} and Hg^{2+}. However, after the modification of either GraF or Au nanocages, the signals toward Zn^{2+}, Cd^{2+}, and Pb^{2+} initiated to be detectable. More surprisingly, the signals of Zn^{2+}, Cd^{2+}, and Pb^{2+} were further enhanced by the composite of GraF and gold nanocages modified on GCE, indicating a synergetic effect. Lastly, extremely low LOD was obtained in the simultaneous detection, i.e., 0.08, 0.09, 0.05, 0.19, and 0.01 ppb for Zn^{2+}, Cd^{2+}, Pb^{2+}, Cu^{2+}, and Hg^{2+} ions, respectively.
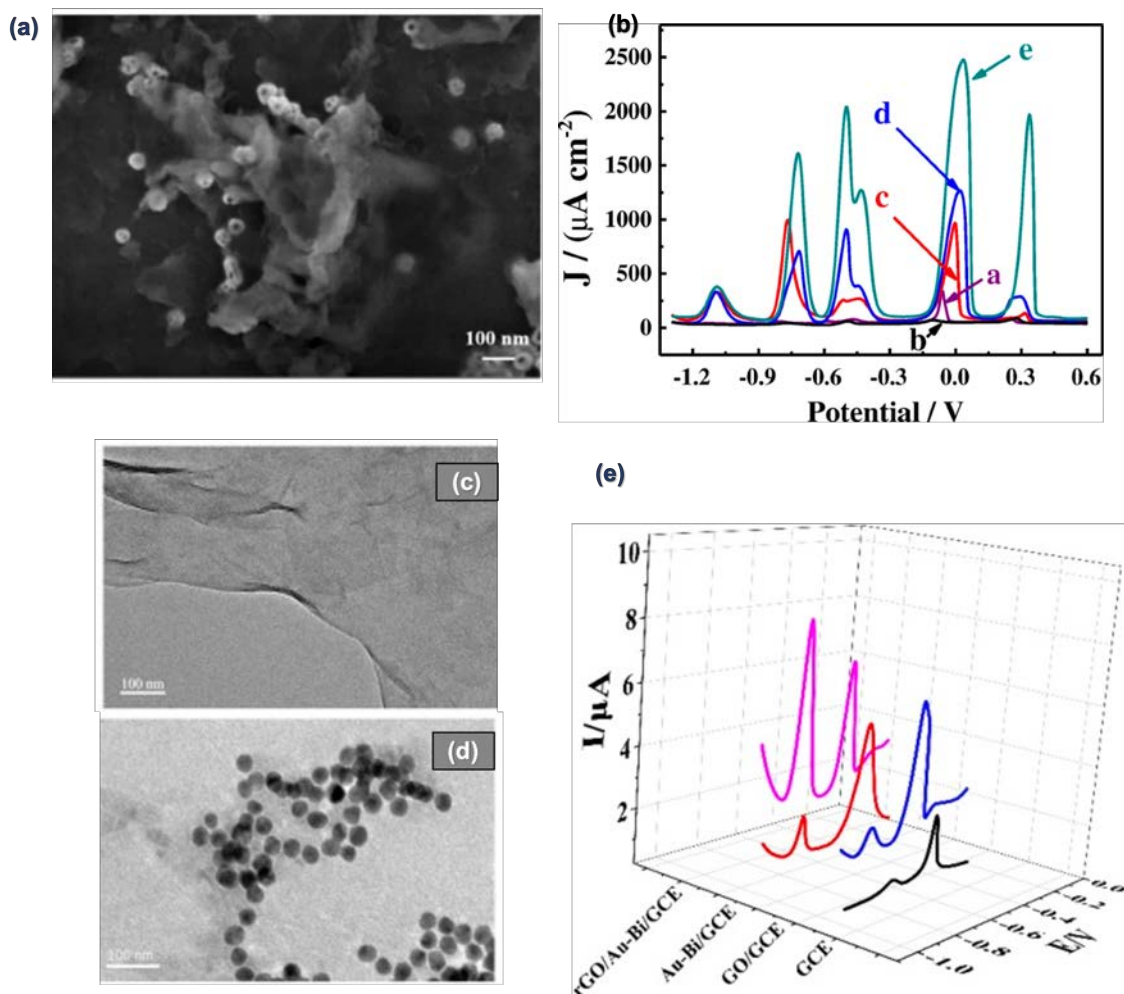
Figure 1.3.9 (a) High-magnified SEM image of GraF/Au nanocage. (b) SWASV voltammograms of a. bare GCE, b. graphene, c. GraF, d. Au nanocage, and e. GraF/Au nanocage electrode for simultaneous determination of 2 ppm Zn^{2+}, Cd^{2+}, Pb^{2+}, Cu^{2+}, and Hg^{2+} in 0.1 M HAc-NaAc solution (pH=5.0).[274] SEM images of (c) rGO sheet and (d) rGO/Au-Bi. (e) DPASV responses of bare GCE, GO/GCE, Au-Bi/GCE, and rGO/Au-Bi/GCE in 0.1 M HAc-NaAc (pH=4.5) buffer containing 100 ppb Pb^{2+} and Cd^{2+}.[275]

Similarly, Wang et al. reported a composite of Au-Bi bimetallic nanoparticles supported by rGO (Figure 1.3.9c-d) and modified the composite on GCE. Due to the presence of Pb^{2+}, the sensitivity of bare GCE toward Cd^{2+} was drastically decreased (Figure 1.3.9e). However, after the modification of the composite, the Cd^{2+} stripping peak started to be observable. Also, the synergetic phenomenon was found that either Au-Bi nanoparticles or rGO modified GCE had a lower Cd^{2+} signal compared to the composite. The ultra-low LOD was obtained as 0.05 and 0.02 ppb for Pb^{2+} and Cd^{2+} in simultaneous detection.[275]

b. Non-metallic nanomaterials

Besides harnessing the metallic nanomaterials/composites to alleviate mutual interference, using non-metallic nanomaterials with enriched N, S, F and O elements is a second possible strategy *via* their high electronegativity and affinities toward HM cations. Since it does not

require any metallic materials, the following issues such as recycling, secondary pollution and potential toxicity could be avoided.

Carbon-based nanomaterials such as CNTs,[276] carbon nanofibers,[277] rGO,[278] and g-C$_3$N$_4$ [279] are the major choice to modify GCEs and SPCEs. However, due to the inert and hydrophobic nature of carbon, the intrinsic carbon-based nanomaterials possess less adsorption capacity for HMIs compared to the tailored ones with various functional groups or doped with other foreign atoms.[280] Amongst these tailored carbon materials, the introduction of heteroatom (N, S, O, *etc.*) with strong electronegativity has great potential to solve the mutual interference issue *via* enhanced adsorption.

Taking CNTs as one example, Wei et al presented a new type of functionalized MWCNTs *via* NH$_3$-plasma treating, resulting in enriched amino groups on the surface of MWCNTs (MWCNTs-NH$_2$, Figure 1.3.10a).[281] They compared the simultaneous sensing performance toward Zn^{2+}, Cd^{2+}, Cu^{2+} and Hg^{2+} of bare GCE, MWCNTs-modified GCE, and MWCNTs-NH$_2$ modified GCE (Figure 1.3.10b). When using GCE, all oxidative peaks of Zn^{2+}, Cd^{2+}, Cu^{2+}, and Hg^{2+} were unobservable due to mutual interference. In the same condition, the stripping peaks of Cd^{2+}, Cu^{2+}, and Hg^{2+} started to appear when using MWCNTs-GCE, but Zn^{2+} was still undetectable. When using MWCNTs-NH$_2$ modified GCE, all the oxidative peaks were identified, and Zn^{2+} ions have an observable and discrete oxidative peak, which cannot be found in the other cases. The enhanced sensitivity toward Zn^{2+} by MWCNTs-NH$_2$ is not only attributed to the better charge transfer due to the graphite-like structure of MWCNTs-NH$_2$, but also to the enrichment of target HMIs particularly Zn^{2+}, which has a good affinity with the functionalized amino groups. Finally, MWCNTs-NH$_2$ modified GCE demonstrated LOD of 0.31, 0.027, 0.22, and 0.14 nM toward Zn^{2+}, Cd^{2+}, Cu^{2+}, and Hg^{2+}, respectively.

Besides carbon-based nanomaterials, polymers are also employed to overcome the mutual interference issue through tunable chemical properties. Particularly, numerous studies reported the modification of sensing electrodes with carbon nanomaterials and conductive polymer nanocomposites such as polypyrrole (Ppy),[282] poly (sodium 4-styrene sulfonate),[283] poly(l-glutamic acid),[284] PEDOT[285] and polyaniline (PANI).[277] Besides, these polymers facilitated the dispersion of carbon-based materials and prevented their aggregation.

In 2015, Promphet et al. investigated a graphene/PANI/polystyrene (G/PANI/PS) nanocomposite, which was deposited on SPCE by electrospinning. The synthesized G/PANI/PS had a fiber-like morphology in the microscale, including a nanoporous structure on the fiber surface, which is shown in Figure 1.3.10c-d.[277] G/PANI/PS assisted the Cd^{2+} sensing signal to recover from the interference of Pb^{2+} compared to the bare SPCE (Figure 1.3.10e). To investigate the influence of the introduced polymers (PANI and PS), the sensing performance was compared between the bare SPCE and PANI/PS-modified SPCE in simultaneous detection of Cd^{2+} and Pb^{2+}. It was found that PANI/PS assisted Cd^{2+} to recover its sensing signal from the signal loss caused by Pb^{2+}. Even more surprisingly, G/PANI/PS achieved a higher sensing signal

than PANI/PS, underlining the significance of graphene. Finally, with the *in-situ* deposition of Bi, G/PANI/PS-modified SPCE achieved the LOD down to 3.3 and 4.3 ppb for Pb^{2+} and Cd^{2+} respectively.
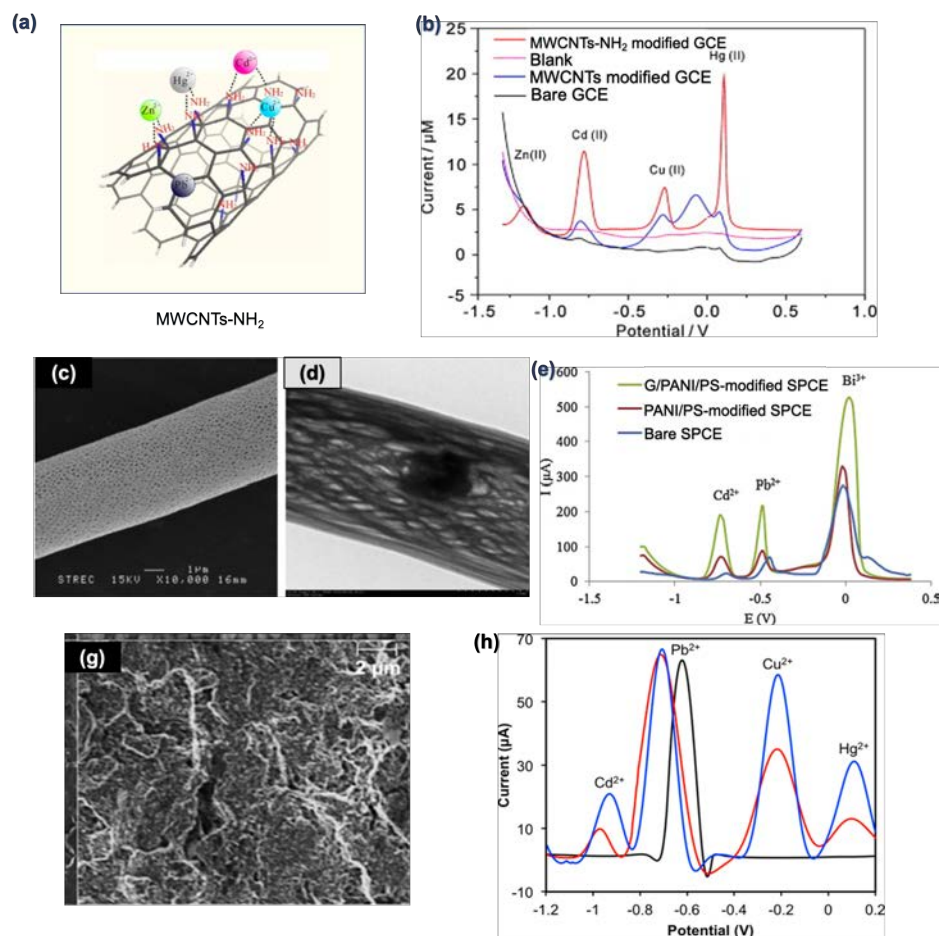

Figure 1.3.10. (a) Schematic representation of the possible interactions between HMIs and MWCNTs-NH$_2$ for sensing HMIs. (b) Stripping voltammetry of the bare, MWCNTs, and MWCNTs-NH$_2$ modified GCE in 0.1 M NH$_4$Cl/NH$_3$ solution (pH 7.0) containing 0.3 μM Zn^{2+}, 0.15 μM Cd^{2+}, 0.25 μM Cu^{2+} and 0.15 μM Hg^{2+}, and MWCNTs-NH$_2$ modified GCE in blank sample (0.1 M NH$_4$Cl/NH$_3$ solution (pH 7.0)) in the absence of any HMIs.[281] (c) SEM images of the G/PANI/PS nanoporous fibers and (d) TEM images of random distribution of graphene in the G/PANI/PS nanoporous fiber. (e) Voltammograms of 200 ppm Pb^{2+} and Cd^{2+} with 900 ppb Bi^{3+} in 0.1 M HCl (pH 1.0), measured by the bare SPCE, PANI/PS-modified SPCE, and G/PANI/PS-modified SPCE.[277] (g) SEM images rGO/PPy-modified SPCE. (h) Voltammograms of 14 ppm Pb^{2+} at rGO/PPy-modified SPCE in the absence (black line) and in the presence (red line) of 0.15 ppm of Cd^{2+}, 0.2 ppm of Cu^{2+}, and 0.3 ppm of Hg^{2+} and (blue line) 14 ppm of Cd^{2+}, Cu^{2+}, and Hg^{2+} each.[282]

Another nanocomposite of cysteine-functionalized rGO/Ppy was used to modify the SPCE to detect Pb^{2+} under the interference from other HMIs, namely Cd^{2+}, Cu^{2+}, and Hg^{2+}. Pb^{2+}, requiring more negative potential to be deposited, was frequently influenced when co-existing with Cu^{2+} and Hg^{2+} requiring less deposition potential. In this study, GO was first functionalized with cysteine *via* hydroxylic groups on its surface and carbonyldiimidazole as

mediate.[282] Then, CV was operated by SPCEs in pyrrole and cysteine-functionalized GO solution so that the rGO/Ppy nanocomposite was deposited on the WE of SPCE. The morphology of the composite was shown in Figure 1.3.10f. When detecting Pb^{2+} with and without the interferents of Cd^{2+}, Cu^{2+} and Hg^{2+}, the current intensity of the Pb^{2+} oxidative peak was minimally influenced, demonstrating the anti-interference capacity of rGO/Ppy in Figure 1.3.10h. The introduction of a great number of thiol groups, carboxylic groups, and amide groups assisted Pb^{2+} adsorption and reduced the ions' competition.

Additionally, the composites of silicon-based materials (with 3-D nanostructure) and conductive polymers have been used as sensing materials due to their high crystallinity, large specific surface area, and good chemical and physical stability.[286]

For example, Abdulla et al. presented a composite comprising thiol (–SH) grafted poly (3,4-proplenedioxythiophene) (PProDOT(MeSH)$_2$) and porous silicon spheres (Si), which was modified on GCE to detect HMIs of Cd^{2+}, Pb^{2+}, and Hg^{2+}. [285] The poly(3,4-proplenedioxythiophene) (PProDOT) is a conjugated polymer with high electron richness. In this study, a different monomer including thiol moieties was employed to polymerize and form its variant—PProDOT(MeSH)$_2$, which was expected to have a better affinity with target HMIs. Cd^{2+} had a relatively lower sensing signal when using Si-modified GCE than Pb^{2+} and Hg^{2+}; however, when using PProDOT(MeSH)$_2$@Si composite-modified GCE, the peak current of Cd^{2+} was enhanced. This behavior could be related to the introduced thiol groups PProDOT(MeSH)$_2$. Additionally, with the support of the nanoporous structure of Si spheres, the exposed surface of PProDOT(MeSH)$_2$ was further increased, with LOD of 0.00575, 0.0027, and 0.0017 µM toward Cd^{2+}, Pb^{2+} and Hg^{2+}, respectively.

Non-metallic nanomaterials including the composites of carbon, conductive polymers, and nanoporous silicon have been harnessed to eliminate the mutual interference effect, through the affinity of introduced electronegative atoms with target HMIs. Compared with the addition of metallic materials, this strategy benefits from relatively low toxicity without recycling issues. However, the presented experimental results still cannot support a clear mechanism and the relation between a specific functional group and certain HMIs specie is still ambiguous, which needs further investigation in the future.

c. Other emerging nanomaterials

Apart from those typically used materials, emerging nanomaterials such as Mxenes, semiconductor oxides, and metal-organic framework (MOFs) have been reported to solve the mutual interference issue.

As a new family in 2DNMs, Mxenes feature good electrical conductivity and hydrophilicity, with relatively simple and environmental-friendly synthesis.[287] MXenes are synthesized from the precursor of $M_{n+1}ZX_n$ (n=1-3), where M represents an early transition metal (from group IIIA to VIIA), Z represents an element from group IIIA or IVA in the periodic table, and X is C or

N. The Z-layer of $M_{n+1}AX_n$ can be selectively etched, and the layered hexagonal transition metal carbides or nitrides are formed. MXenes inherit many properties of 2DNMs *e.g.,* the large surface area and tunable interface property. Given that they are terminated by oxygen-containing groups (*e.g.,* hydroxyls) and fluorine (F) atoms forming in the etching process, these functionalized groups could facilitate the adsorption of HMIs,[288] and thus Mxenes may enhance the sensitivity and reduce the mutual interference effect.

Zhu et al. synthesized a layered MXene, namely Ti_3C_2, for simultaneous detection of Cd^{2+}, Pb^{2+}, Cu^{2+} and Hg^{2+}.[289] The pristine Ti_3C_2 was synthesized from the precursor of Ti_3AlC_2 by the etching process (shown in Figure 1.3.11a,b), and deposited on GCE. It was found to enhance the sensitivity of GCE toward Cu^{2+} and Pb^{2+}, compared to the bare GCE whose sensing signals were ambiguous and poor. However, Cd^{2+} and Hg^{2+} were still undetectable by the pristine Ti_3C_2. Hence, it was tailored through an alkalization process, in which Ti_3C_2 power was dispersed and soaked in a KOH solution (5 wt%). Consequently, alkalization-intercalated Ti_3C_2 (alk-Ti_3C_2) was achieved with the typical layered morphology with pristine Ti_3C_2 (Figure 1.3.11b). Based on previous studies, the cation-exchanged surface chemistry of Ti_3C_2 can be tuned by the alkalization process. Therefore, alk-Ti_3C_2 was tested on GCE in the same solution containing Cd^{2+}, Pb^{2+}, Cu^{2+} and Hg^{2+} with the pristine Ti_3C_2. In this case, the oxidative peaks of Cd^{2+} and Hg^{2+} were observed with alk-Ti_3C_2-modified GCE (Figure 1.3.11c).

Besides, the nanomaterials of semiconductor oxides (such as tin oxide (SnO_2),[290] manganese dioxide(MnO_2),[291] magnesium oxide (MgO),[292] ferroferric oxide (Fe_3O_4)[293], *etc*) have oxygen-enriched surfaces that could serve as active sites for HMIs' electrodeposition.[206] The ferroferric oxide (Fe_3O_4) withdraws attention due to ease of preparation, low toxicity and the magnetic feature.[294,295]

For example, Li et al. synthesized an innovative nanoplate-stacked Fe_3O_4 and utilized this material to modify GCE to detect five multiple HMIs (*i.e.* Zn^{2+}, Cd^{2+}, Pb^{2+}, Cu^{2+} and Hg^{2+} ions) simultaneously. The Fe_3O_4 nanoplates were found to have a good affinity with Pb^{2+}, for it enhances the selectivity of GCE toward Pb^{2+}.[296] Interestingly, different crystal planes originated from different phases of Fe_3O_4 (*i.e.,* (100)-bound cubic and (111)-bound octahedral nanocrystals) also determine the selectivity toward Pb^{2+}. (111)-bound octahedral Fe_3O_4 nanocrystal demonstrated the highest selectivity toward Pb^{2+} amongst other HMIs such as Zn^{2+}, Cd^{2+}, Cu^{2+} and Hg^{2+}. Besides, (111)-bound octahedral Fe_3O_4 also presented a higher sensing signal of Pb^{2+} compared to (100)-bound cubic Fe_3O_4 nanocrystal, which may be caused by the selective adsorption of Pb^{2+} on different crystal planes.[293]
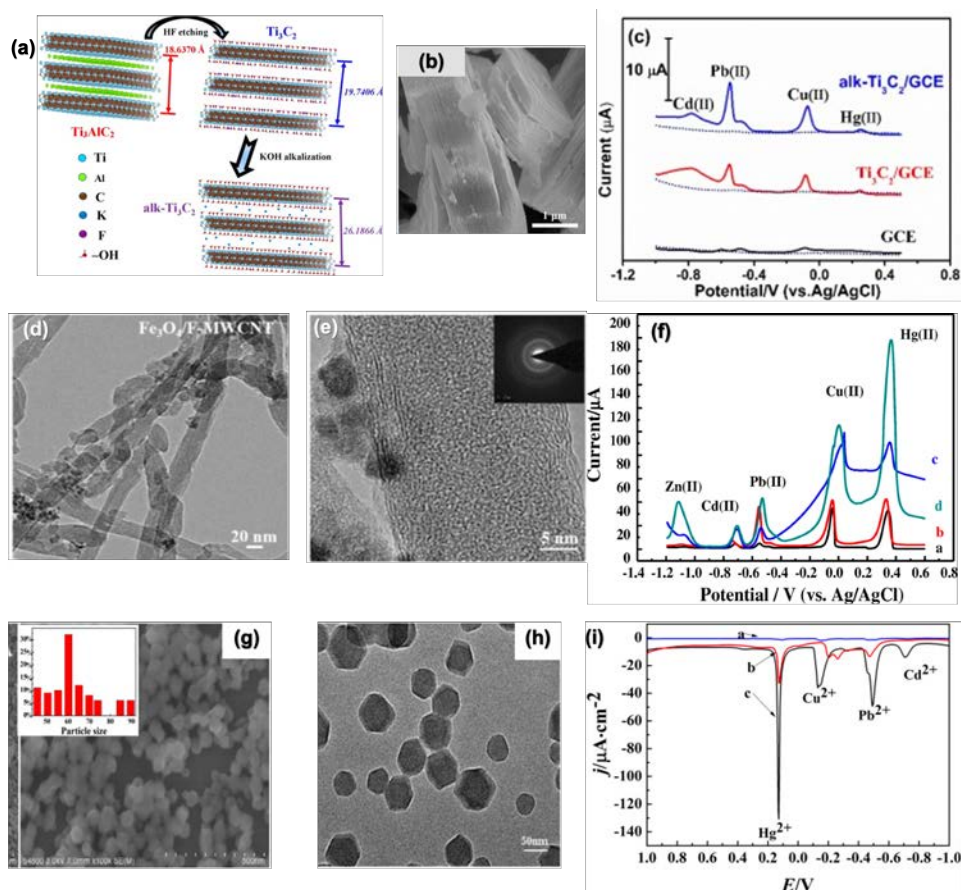
Figure 1.3.11 (a) Schematic illustrations of the Ti_3AlC_2 and the post-etching MXene before and after alkalization treatment; (b) SEM images of alk-Ti_3C_2; (c) Voltammograms of these three different electrodes detecting 0.5 μM Cd^{2+}, Pb^{2+}, Cu^{2+} and Hg^{2+} in HAc-NaAc (pH = 5.0) simultaneously.[289] (d)TEM image of Fe_3O_4/F-MWCNTs and (e) its HRTEM image with corresponding selected area electron diffraction pattern. (f) The stripping voltammograms of 10 μM five HMIs detected by a. GCE, b. Fe_3O_4-modified GCE, c. fluorinated MWCNT(F-MWCNTs)-modified GCE and d. Fe_3O_4/F-MWCNTs -modified GCE in 0.1 M HAc-NaAc buffer solution (pH = 5.0).[297] (g) SEM image and (h)TEM image of ZIF-8. The inset in (g) is the bar chart of ZIF-8 size distribution; (i) Sensing response of a. without and c. with 0.01 mM HMIs (namely Hg^{2+}, Cu^{2+}, Pb^{2+}, and Cd^{2+}) on ZIF-8/Chitosan-modified GCE in 0.1 M HAc-NaAc (pH 3.0). Curve b is the sensing curve of 0.01 mM HMIs (namely Hg^{2+}, Cu^{2+}, Pb^{2+}, and Cd^{2+}) on the control electrode of Chitosan-modified GCE.[298]

The composites of metal oxides and carbon-based materials are preferable to achieve better electrochemical sensing performance due to the synergetic effect, rather than only metal oxides themselves.[208] For example, Wu et al. presented a Fe_3O_4/fluorinated MWCNT(F-MWCNTs) composite and modified GCE with this composite in order to detect HMIs (*i.e.*, Zn^{2+}, Cd^{2+}, Pb^{2+}, Cu^{2+}, and Hg^{2+} ions).[297] Compared with the pristine MWCNTs, the F-MWCNTs have stronger electronegativity because of the introduced fluorine(F) atoms, which facilitates the adsorption of HMIs. In this study, the authors took advantage of both F-MWCNTs and Fe_3O_4 nanoparticles (Figure 1.3.11d-e) to alleviate the mutual interference effect. When using the bare GCE, only Cu^{2+} and Hg^{2+} were able to be detected in the mixed solution of Cd^{2+}, Pb^{2+},

Hg^{2+}, Zn^{2+} and Cu^{2+} at the concentration of 10 µM (Figure 1.3.11f). When being modified by Fe_3O_4 nanoparticles, GCE was able to detect Pb^{2+} besides Cu^{2+} and Hg^{2+}, which may be attributed to the specific affinity between Pb^{2+} and Fe_3O_4. More interestingly, F-MWCNTs further increased the sensing signals of Cd^{2+}, Zn^{2+}, and Pb^{2+} slightly without influencing the signals of Cu^{2+} and Hg^{2+} compared to the results by the bare GCE. As expected, all the oxidative peaks identified as Cd^{2+}, Pb^{2+}, Hg^{2+}, Zn^{2+} and Cu^{2+} were detectable by the composite of Fe_3O_4/F-MWCNTs. Therefore, this composite rendered Zn^{2+}, Cd^{2+}, and Pb^{2+} to be detectable together with Cu^{2+} and Hg^{2+} simultaneously, which is impossible for the bare GCE at the same concentration.

Besides, Li et al. reported a bimetal oxide, *i.e.*, porous Ce-Zr oxide nanospheres, which was used to modify the GCE. The modified GCE showed anti-interference ability when detecting Pb^{2+} in the mixed solution containing other HMIs of Cd^{2+}, Cu^{2+}, Zn^{2+} and Hg^{2+}. Typically, the sensitivity of Pb^{2+} will decrease in the presence of Cu^{2+}, for Pb^{2+} ions require a more negative deposition potential, which may tend to deposit on the surface of Cu (requiring less negative potential) instead of on the surface of the carbon electrode.[299] In this study, the selective enrichment of Pb^{2+} ions was achieved by the Ce-Zr oxide nanospheres, which were validated by the results of XPS characterization.[300] Consequently, Pb^{2+} ions detection in the presence of other HMIs was not influenced. The sensitivity of Pb^{2+} in the individual testing was close to the one in the simultaneous detection, proving the capacity of the Ce-Zr oxide nanospheres to prevent the influence of mutual interference on Pb^{2+}.

Besides the porous inorganic materials providing a large surface area for HMIs detection, MOF, a new class of porous polymeric materials consisting of metal ions linked with organic bridging ligands, has been studied for HMIs detection in the latest two decades due to its tunable surface chemistry and high active surface area.[301] Amongst various MOFs, zeolitic imidazolate framework (ZIF) is a family comprising tetrahedrally-coordinated transition metal ions (*e.g.*, Fe^{3+}, Co^{2+}, Cu^{2+} and Zn^{2+}) connected by imidazolate or its derivatives linkers. ZIF has good chemical stability, particularly in the aqueous phase, showing great potential in electrochemical HMIs detection in waters.[302]

In 2019, Chu et al. presented a composite of ZIF-8 (Zn^{2+} linked by imidazolate framework)/chitosan which was used to modify GCE to detect Cd^{2+}, Pb^{2+}, Cu^{2+} and Hg^{2+} simultaneously.[298] The diameter of ZIF-8 was 60 nm approximately in Figure 1.3.11g-h. The obtained sensing results were compared to the ones using chitosan-modified GCE. ZIF-8 demonstrated the enhancement of Cd^{2+} sensitivity with the presence of Pb^{2+} and Cu^{2+}. The oxidative peak which should have been identified as Cd^{2+} was undetectable by the chitosan-GCE or bare GCE due to mutual interference; however, with the addition of ZIF-8, Cd^{2+} was able to be detected, indicating that the ZIF-8 reduced the mutual interference effect in simultaneous detection (Figure 1.3.11i).

3) Selective complexing with interfering ions

The strategies mentioned above are mainly based on facilitating heavy metal adsorption and thus deposition on the sensing electrode *via* chemical modification. The other strategy for reducing mutual interference is converse *via* removing the interfering cations away from the sensing electrodes.

For example, Huang et al. utilized a AuNPs/Nafion composite to modify the GCE to detect As^{3+}. Even though the AuNPs/Nafion-modified electrode was highly sensitive toward As^{3+} individually, the As^{3+} sensitivity dramatically decreased with the presence of Cu^{2+} and Hg^{2+}. To recover the As^{3+} sensitivity, the chelating agent ethylenediaminetetraacetate (EDTA) was utilized to pretreat the sample solution, for its complexation with these interfering metal ions (*i.e.*, Hg^{2+} and Cu^{2+}) was easier than that with As^{3+},[303] and the formed complexes were excluded from the WE. To examine the analytical performance with EDTA addition, the AuNPs/Nafion-modified GCE was tested in the mixed solution of 10 ppb As^{3+} with the addition of either Cu^{2+} or Hg^{2+} ranging from 100 to 1000 ppb as interferents. With the presence of 0.1 M EDTA, the stripping peak of As^{3+} at −0.03 V maintained the same peak potential and current intensity upon the increasing interferents concentration. However, when EDTA was absent in the testing solution, the stripping peak of As^{3+} was suppressed by the oxidation of Cu^{2+} and Hg^{2+}.[304] Similarly, Czop et al. attempted to utilize EDTA to detect Tl^+ ions by removing the interferents of Cd^{2+} ions *via* complexation, for the stripping peaks of Cd^{2+} and Tl^+ have very close potential which causes the peak overlapping issue for specie identification.[305]

Besides EDTA, ferricyanide ($[Fe(CN)_6]^{3-}$) anions are another common mask reagent,[299,306] to remove Cu^{2+} ions in samples and prevent its mutual interference on other HMIs—suppressing sensing signals of Zn^{2+}, Pb^{2+} and Cd^{2+}. With the addition of potassium ferricyanide ($K_3[Fe(CN)_6]$, 0.03 mM), the sensing signals of Zn^{2+}, Pb^{2+} and Cd^{2+} were recovered, with the presence of interferent Cu^{2+} ions up to 500 ppb. However, the excessive addition of $K_3[Fe(CN)_6]$ could also decrease the sensing signals of target HMIs (*e.g.,* Zn^{2+}). The optimum condition of this strategy must be investigated before validation.

1.3.5 Addressing Water Matrix Interference issues

In addition to mutual interference, the real sample matrix also influences analytical signals of *in-situ* measurements. For example, dissolved oxygen and organic matters in natural waters lead to fouling on sensing probes, which substantially decreases sensitivity.[207]

To resist this effect, nanoporous silica serving as a typical filtration material has been used in *in-situ/-vivo* sensing applications in natural waters and biofluids in tissue.[307,308] Interferents such as proteins, cells, and bacteria were filtered by the nanoporous silica, and only the small target analytes were able to access the surface of the WE through the vertical nanochannels of nanoporous silica.

For example, Cheng et al. presented a vertically-ordered mesoporous silica film (VMSF) to modify the indium tin oxide (ITO) electrode in order to reduce the interference from large

organic compounds in real samples of soil leaching solution and proteins from blood serum (Figure 1.3.12 a).[309] Comparison study was carried out by VMSF-modified ITO and bare ITO, which were tested in the same solutions spiked with Pb^{2+} and Cu^{2+}. In simultaneous detection of Pb^{2+} and Cu^{2+}, the bare ITO exhibited poor and distorted sensing signals in both serum and soil leaching solution; while VMSF-modified ITO demonstrated detectable and clear oxidative peaks of Pb^{2+} and Cu^{2+}, denoting that VMSF possessed the anti-fouling capacity.

Besides large proteins and bacteria that may foul the WE, some organic molecules commonly appear in natural waters such as fulvic acid and humic acid (HA) also suppress the sensing signals of HMIs.[205] Aiming to address this issue, Liu et at. proposed a strategy of adding Fe^{3+} ions in tested real samples to complex with HA.[310] First, the current intensity of As^{3+} stripping peak by the Au electrode was found to decrease gradually upon the increasing concentration of HA (from 0 to 40 mg/L, Figure 1.3.12b-d). Then, a variety of Fe^{3+} solutions (at 0, 20, 40 mg/L) were added to the testing sample (Figure 1.3.12e). When adding 20 mg/L Fe^{3+}, only an 8.5% decrease of the As^{3+} peak intensity was observed in the presence of 20 mg/L HA, compared to the one of 21.3% without any addition of Fe^{3+}. With increasing Fe^{3+} amount (40 mg/L), the sensing signal was further recovered with minimal signal loss as low as 3.2%. Hence, the addition of Fe^{3+} ions prevented the sensing signal of As^{3+} from decreasing caused by HA.

In contrast to the strategy of removing the interfering matters from the real sample, filtering and accumulating target HMIs from the sample has been investigated, too. For example, GO includes various functional groups such as hydroxy (-OH) and carboxyl (-COOH), which could promote HMIs adsorption in the optimum condition due to the strong electronegativity, and thus GO has been used as an adsorbent for HMIs.[311] In reversible desorption, target HMIs can be re-dissolved into the artificial buffer from the GO adsorbent, ensuring the removal of interferents in the real sample matrix.

Combining the merits of GO and *in-situ* microfluidic devices, Chałupniak et al. designed and fabricated a novel microfluidic system as a new strategy to reduce the interference from saline seawater. The microfluidic system consisted of two microfluidic chips: 1) a GO–PDMS composite microfluidic chip for reversible adsorption/desorption of heavy metals, followed by 2) a second microfluidic chip (normal PDMS) with an SPCE embedded for electrochemical detection toward Pb^{2+}. GO–PDMS composite was synthesized feasibly *via* blending GO with silicon monomer in tetrahydrofuran (THF), then was polymerized triggered by a curing agent. The microfluidic chip based on GO-PDMS was able to accumulate Pb^{2+} cations from the continuous testing flow on the surface of the microfluidic channel and drive the accumulated Pb^{2+} cations to dissolve in an injected artificial supporting electrolyte (0.1 M HCl, Figure 1.3.12f). Afterward, Pb^{2+} cations in the supporting electrolyte were detected in the second PDMS-based microfluidic by SPCE (Figure 1.3.12g-h). Unlike the normal PDMS microfluidic limited to high baseline and poor sensing signals of SPCE caused by high salinity in seawater, the proposed strategy prevented the interference from the seawater matrix, showing improved sensitivity toward Pb^{2+}. [227]
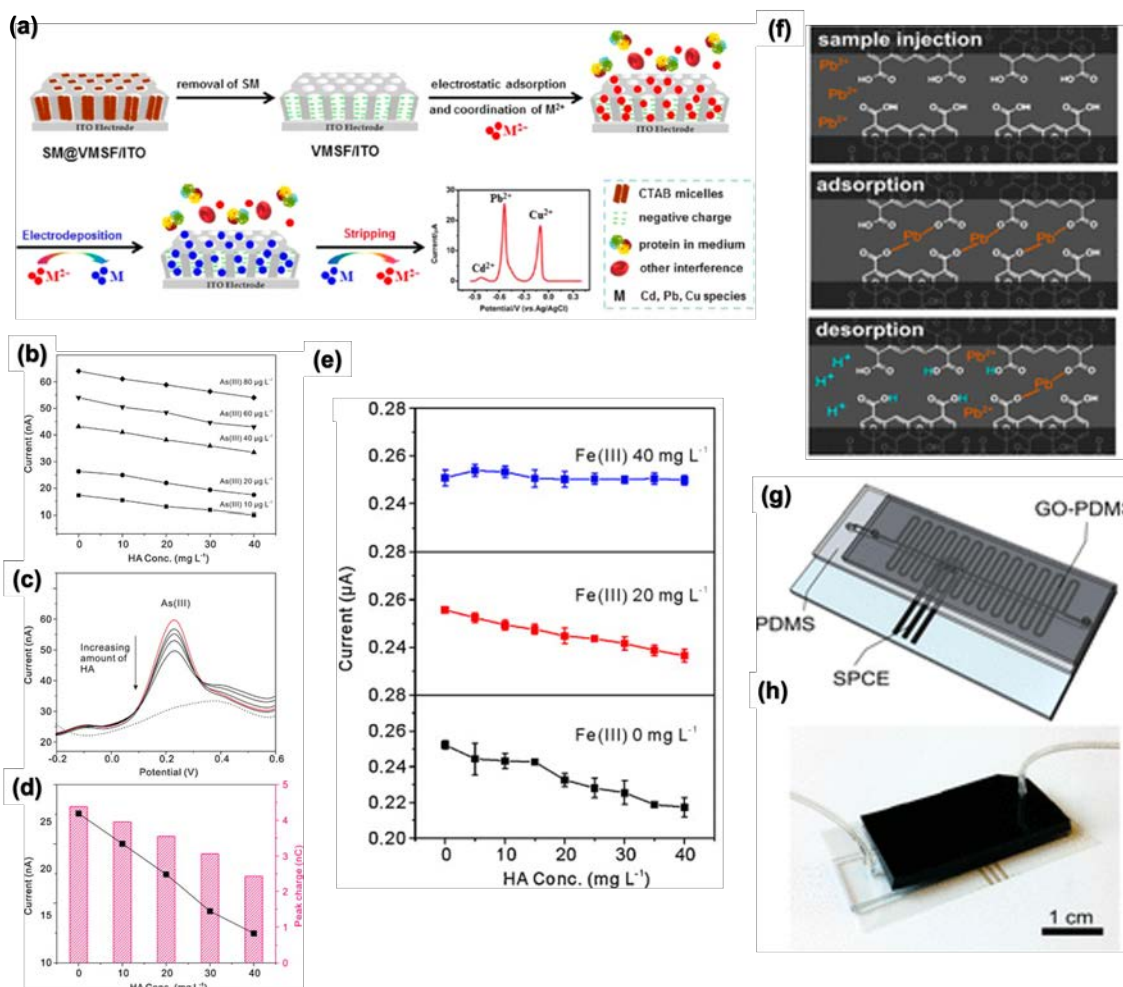
Figure 1.3.12. (a) Schematic illustration of the preparation of VMSF/ITO sensor and its simultaneous detection of Pb^{2+}, Cu^{2+} and Cd^{2+}.[309] SM denotes CTAB surfactant micelles. (b) Dependence of oxidative peak current of As^{3+} on the concentration of humic acid. (c) Voltammograms of 20 ppb As^{3+} without (red line) and with humic acid (ranging from 10 to 40 ppm) (black lines). (d) Dependence of oxidative peak current and corresponding peak charge of 20 ppb As^{3+} on the concentration of humic acid. Electrolyte, $N_2H_4 \cdot 2HCl$ solution (pH 0.5); deposition potential, −0.35 V; deposition time, 90 s. (e) Dependence of oxidative peak current of 20 ppb As^{3+} on the concentration of humic acid with different concentrations of Fe^{3+}.[310] (f) Reactions occurring in the chip: Pb^{2+} was adsorbed onto GO–PDMS; 0.1 M HCl was injected to perform desorption and detection. A sample was passed from GO–PDMS chip to PDMS electrochemical chip, where SWASV was performed. (g) the scheme of the GO–PDMS chip and PDMS chip. (h) Image of the full LOC device with polymeric tubes connected to the inlet and outlet.[227]

Additionally, even though the dissolved oxygen has minimal effect on the analysis using the SWASV technique, mechanical vibration can remove dissolved oxygen *in situ*, providing a universal way for other ASV techniques. For example, ultrasound is able to alleviate dissolved oxygen. Also, it can remove the bubbles generated by hydrogen evolution reaction on the

metallic electrode during the deposition step, and significantly improve both sensitivity and reproducibility.[312]

1.3.5   Conclusion and Future Perspectives

In-situ heavy metal measurement is critically important for public safety particularly in the application of environmental monitoring. Moreover, a wearable sensor as a special example of *in-situ* analysis in healthcare plays an important role in monitoring physiological signals including HMIs such as Zn^{2+} and Cu^{2+} in the human body. Amongst diverse electrochemical techniques, ASV is promising to fit most criteria of *in-situ* measurements, with great potential in fully automatic and low-cost detection of a wide range of HMIs. In the field of environmental monitoring, portable sensing probes have been investigated for validation in the laboratory and in the field but require human labor due to the lack of automation. Few *in-situ* HMIs measurement has been validated yet. A natural progression is to construct a huge sensing network to respond to HMIs at their dangerous level automatically, which can be realized by integrating sensors with an automatic boat or implanting numerous submersible sensors with long-term chemical stability. In general, portability, automation, and long-term stability deserve to be further improved besides sensitivity and selectivity. Moreover, emerging technologies *e.g.* ANN could be involved to improve the accuracy and predict pollutant concentration in natural waters.[313]

Wearable sensors, on the other hand in healthcare, can perform sampling and detection of HMIs in sweat on the skin; however, several limitations can be further improved. First, the whole sensing systems detecting HMIs in sweat (including conductive connections, potentiostat, and readout devices) are not highly integrated and wearable. The presented studies about wearable HMIs sensors mainly focused on the testing performance of the sensor itself but ignored the performance of the integrated system including analysis and readout modules. The communication module in the sensing system is wired with a readout device, and a commercial potentiostat is not wearable on the skin, which is inconvenient for practical use. Second, continuous monitoring of HMIs in sweat by wearable sensors has rarely been reported. Well-manipulating sweat excretion and testing flow for good accuracy and robustness need to be achieved in the future. Third, high-cost fabrication techniques (*e.g.,* photolithography) have been widely employed to manufacture wearable HMIs sensors in most presented studies. Various printing techniques can be applied in the fabrication to reduce the cost.

Additionally, open issues *i.e.,* mutual interference and sample matrix interference are still hampering the progress in practical use. Considering that *in-situ* measurements naturally require simple or even zero sample pretreatment, mathematical models and chemical modification could be more favorable in this sense. Chemical modification using metallic nanomaterials and their composites is very effective to address the mutual interference issue, particularly to recover the diminished sensing signal with the presence of other interferents.

Due to the potential pollution, high cost, and recycling issues, non-metallic materials such as graphene, CNTs, and polymers initiated to appear and alleviate mutual interference *via* the enriched O, S, and N with good affinity to HMIs. The tunable chemistry of these materials is fascinating to reveal their specific binding affinity with specific HMIs based on experimental validation. Besides, to be compatible with the other strategy of removing interfering ions, a more robust microfluidic sensing system with various functions such as preconcentrating, washing and sensing should be explored in the future.

Furthermore, the power source is a general issue for many sensing systems, particularly for *in-situ* sensing systems, as the replacement of *in-situ* sensors is very inconvenient and influences the duration time. The battery may pose a second pollution risk to the environment. The battery-free sensing system is appealing, for example, several reports about HMIs sensing tag, charged by a mobile phone through RFID technology, have been presented.[314,315] New energy technologies may be useful to solve this issue in the future, such as solar cells, biofuels, and wireless charge by radio frequency.

1.4 Motivation and Objectives

Portable, low-cost, and *in-situ* sensors are massively demanded in the fields of environmental monitoring and healthcare; however, the standard methods by bulky equipment (*e.g.*, ICP-MS) rely on laboratory condition and trained personnel with high expense, which is difficult to fulfill this need. For this aim, electrochemical techniques are used to produce a simplified sensing platform. In their fabrication, printing techniques can further decrease the size of sensors with massive production and low cost. Besides, the employment of nanomaterials in electrochemical sensors demonstrates a better sensing performance, which could alleviate the sensitivity and selectivity issues of electrochemical sensors.

Hence, this thesis aims for exploring electrochemical sensing platforms for *in-situ* measurement that can be preferably fabricated by printing techniques. HMIs are selected as the targets, as they are pollutants in environmental monitoring and indicators for healthcare. To be more detailed, the objectives of this thesis are listed as follows:

i.   The development of an integrated sensing system for *in-situ* monitoring of heavy metal pollutants in natural waters by electrochemical detection. Due to the high cost of human labor, this thesis also aims to increase the automation of this sensing tool.

ii.   The Investigation of the sensing performance by using graphene derivatives aims for mitigating the effect of an open issue of electrochemical heavy metal detection, *i.e.*, mutual interference problem between multiple ions.

iii.   The exploration of multiple printing technologies to fabricate an all-printed wearable device applied in healthcare with the interest of detecting HMIs in sweat.

Reference

(1)   Fraden Jacob. *Handbook of Modern Sensors: Physics, Designs, and Applications*, 4th ed.; 1998.

(2)   Morales-Narváez, E.; Dincer, C. Introduction. In *Wearable Physical, Chemical and Biological Sensors*; Morales-Narváez, E., Dincer, C., Eds.; Elsevier, 2022; pp 1–3.

(3)   Trung, T. Q.; Lee, N.-E. Flexible and Stretchable Physical Sensor Integrated Platforms for Wearable Human-Activity Monitoringand Personal Healthcare. *Adv. Mater.* **2016**, *28* (22), 4338–4372. https://doi.org/https://doi.org/10.1002/adma.201504244.

(4)   R.Sempionatto, J.; Gao, W. Wearable Chemosensors. In *Wearable Physical, Chemical and Biological Sensors*; Morales-Narvaez, E., Dincer, C., Eds.; Elsevier, 2022; pp 219–234.

(5)   Surya, S. G.; Raval, H. N.; Ahmad, R.; Sonar, P.; Salama, K. N.; Rao, V. R. Organic Field Effect Transistors (OFETs) in Environmental Sensing and Health Monitoring: A Review. *TrAC Trends Anal. Chem.* **2019**, *111*, 27–36. https://doi.org/https://doi.org/10.1016/j.trac.2018.11.027.

(6)   Drexelius, A.; Yuan, Y.; Friedel, M.; DeBrosse, M.; Heikenfeld, J. Wearable Biosensors. In *Wearable Physical, Chemical and Biological Sensors*; Morales-Narvaez, E., Dincer, C., Eds.; Elsevier, 2022; pp 235–253.

(7)   Bănică, F.-G. *Chemical Sensors and Biosensors: Fundamentals and Applications*; John Wiley & Sons, Ltd, 2012. https://doi.org/10.1002/9781118354162.

(8)   ReportLinker. The global sensor market is expected to reach an estimated $267.8 billion by 2026 with a   CAGR   of   12.5%   from   2020   to   2026   https://www.globenewswire.com/news-release/2021/12/02/2344740/0/en/The-global-sensor-market-is-expected-to-reach-an-estimated-267-8-billion-by-2026-with-a-CAGR-of-12-5-from-2020-to-2026.html.

(9)   MordorInteligence. WEARABLE SENSORS MARKET - GROWTH, TRENDS, COVID-19 IMPACT, AND FORECASTS (2022 - 2027).

(10)   Borgia, E. The Internet of Things Vision: Key Features, Applications and Open Issues. *Comput. Commun.* **2014**, *54*, 1–31. https://doi.org/https://doi.org/10.1016/j.comcom.2014.09.008.

(11)   MordorIntelligence. WIRELESS SENSORS NETWORK MARKET - GROWTH, TRENDS, COVID-19 IMPACT, AND FORECASTS (2022 - 2027).

(12)   Kaur, N.; Khunger, A.; Wallen, S. L.; Kaushik, A.; Chaudhary, G. R.; Varma, R. S. Advanced Green Analytical Chemistry for Environmental Pesticide Detection. *Curr. Opin. Green Sustain. Chem.* **2021**, *30*, 100488. https://doi.org/https://doi.org/10.1016/j.cogsc.2021.100488.

(13)   Luo, Y.; Xu, L.; Rysz, M.; Wang, Y.; Zhang, H.; Alvarez, P. J. J. Occurrence and Transport of Tetracycline, Sulfonamide, Quinolone, and Macrolide Antibiotics in the Haihe River Basin, China. *Environ. Sci. Technol.* **2011**, *45* (5), 1827–1833. https://doi.org/10.1021/es104009s.

(14)   Chen, M.; Ohman, K.; Metcalfe, C.; Ikonomou, M. G.; Amatya, P. L.; Wilson, J. Pharmaceuticals and Endocrine Disruptors in Wastewater Treatment Effluents and in the Water Supply System of Calgary, Alberta, Canada. *Water Qual. Res. J.* **2006**, *41* (4), 351–364. https://doi.org/10.2166/wqrj.2006.039.

(15)   Vulliet, E.; Baugros, J.-B.; Flament-Waton, M.-M.; Grenier-Loustalot, M.-F. Analytical Methods for the Determination of Selected Steroid Sex Hormones and Corticosteriods in Wastewater. *Anal. Bioanal. Chem.* **2007**, *387* (6), 2143. https://doi.org/10.1007/s00216-006-1084-z.

(16)   Kolodziej, E. P.; Gray, J. L.; Sedlak, D. L. Quantification of Steroid Hormones with Pheromonal Properties in Municipal Wastewater Effluent. *Environ. Toxicol. Chem.* **2003**, *22* (11), 2622–2629. https://doi.org/https://doi.org/10.1897/03-42.

(17)   Harrison, J. P.; Ojeda, J. J.; Romero-González, M. E. The Applicability of Reflectance Micro-Fourier-Transform Infrared Spectroscopy for the Detection of Synthetic Microplastics in Marine Sediments. *Sci. Total Environ.* **2012**, *416*, 455–463. https://doi.org/https://doi.org/10.1016/j.scitotenv.2011.11.078.

(18)   Long, C.; Xu, H.; Shen, Q.; Zhang, X.; Fan, B.; Wang, C.; Zeng, B.; Li, Z.; Li, X.; Li, H. Diagnosis of the Coronavirus Disease (COVID-19): RRT-PCR or CT? *Eur. J. Radiol.* **2020**, *126*, 108961. https://doi.org/https://doi.org/10.1016/j.ejrad.2020.108961.

(19)   Beutel, S.; Henkel, S. In Situ Sensor Techniques in Modern Bioprocess Monitoring. *Appl. Microbiol. Biotechnol.* **2011**, *91* (6), 1493–1505. https://doi.org/10.1007/s00253-011-3470-5.

(20)   Ahsan, M. M.; Hasanuzzaman, M.; Olabi, A. G.; Hashmi, M. S. J. 13.23 - Review of the Reliability and Connectivity of Wireless Sensor Technology; Hashmi, S., Batalha, G. F., Van Tyne, C. J., Yilbas, B. B. T.-C. M. P., Eds.; Elsevier: Oxford, 2014; pp 571–588. https://doi.org/https://doi.org/10.1016/B978-0-08-096532-1.01327-3.

(21)   Senouci, M. R.; Mellouk, A. *Deploying Wireless Sensor Networks*; 2016. https://doi.org/https://doi.org/10.1016/C2015-0-01311-9.

(22)   G. D. Hutcheson. *Into The Nano Era: Moore's Law Beyond Planar Silicon CMOS*; Howard R. Huff, Ed.; Springer.

(23)   Wang, J. *ANALYTICAL ELECTROCHEMISTRY*, Third Edit.; Wiley-VCH, 2006. https://doi.org/10.1002/0471790303.

(24)   Fahmy Taha, M. H.; Ashraf, H.; Caesarendra, W. A Brief Description of Cyclic Voltammetry Transducer-Based Non-Enzymatic Glucose Biosensor Using Synthesized Graphene Electrodes. *Appl. Syst. Innov.* **2020**, *3* (3). https://doi.org/10.3390/asi3030032.

(25)   Costa-Rama, E.; Fernández-Abedul, M. T. Signal Detection Techniques. In *Wearable Physical, Chemical and Biological Sensors*; Moráles-Narvaez, E., Dincer, C., Eds.; Elsevier, 2022; p 97.

(26)   Umapathi, R.; Ghoreishian, S. M.; Sonwal, S.; Rani, G. M.; Huh, Y. S. Portable Electrochemical Sensing Methodologies for On-Site Detection of Pesticide Residues in Fruits and Vegetables. *Coord. Chem. Rev.* **2022**, *453*, 214305. https://doi.org/https://doi.org/10.1016/j.ccr.2021.214305.

(27)   Zhai, Q.; Yap, L. W.; Wang, R.; Gong, S.; Guo, Z.; Liu, Y.; Lyu, Q.; Wang, J.; Simon, G. P.; Cheng, W. Vertically Aligned Gold Nanowires as Stretchable and Wearable Epidermal Ion-Selective Electrode for Noninvasive Multiplexed Sweat Analysis. *Anal. Chem.* **2020**, *92* (6), 4647–4655. https://doi.org/10.1021/acs.analchem.0c00274.

(28)   Crespo, G. A. Recent Advances in Ion-Selective Membrane Electrodes for in Situ Environmental Water Analysis. *Electrochim. Acta* **2017**, *245*, 1023–1034. https://doi.org/https://doi.org/10.1016/j.electacta.2017.05.159.

(29)   GO Systemelektronik. The BlueBox System https://www.go-sys.de/en/bluebox/.

(30)   Zuliani, C.; Diamond, D. Opportunities and Challenges of Using Ion-Selective Electrodes in Environmental Monitoring and Wearable Sensors. *Electrochim. Acta* **2012**, *84* (Complete), 29–34. https://doi.org/10.1016/j.electacta.2012.04.147.

(31)   Tercier-Waeber, M.-L.; Confalonieri, F.; Abdou, M.; Dutruch, L.; Bossy, C.; Fighera, M.; Bakker, E.; Graziottin, F.; van der Wal, P.; Schäfer, J. Advanced Multichannel Submersible Probe for Autonomous High-Resolution in Situ Monitoring of the Cycling of the Potentially Bioavailable Fraction of a Range of Trace Metals. *Chemosphere* **2021**, *282*, 131014. https://doi.org/https://doi.org/10.1016/j.chemosphere.2021.131014.

(32)   Klevay, L. M. Coronary Heart Disease: The Zinc/Copper Hypothesis. *Am. J. Clin. Nutr.* **1975**, *28* (7), 764–774. https://doi.org/10.1093/ajcn/28.7.764.

(33)   Gao, W.; Nyein, H. Y. Y.; Shahpar, Z.; Fahad, H. M.; Chen, K.; Emaminejad, S.; Gao, Y.; Tai, L. C.; Ota, H.; Wu, E.; Bullock, J.; Zeng, Y.; Lien, D. H.; Javey, A. Wearable Microsensor Array for Multiplexed Heavy Metal Monitoring of Body Fluids. *ACS Sensors* **2016**, *1* (7), 866–874. https://doi.org/10.1021/acssensors.6b00287.

(34)   Lee, H.; Hong, Y. J.; Baik, S.; Hyeon, T.; Kim, D.-H. Enzyme-Based Glucose Sensor: From Invasive to Wearable Device. *Adv. Healthc. Mater.* **2018**, *7* (8), 1701150. https://doi.org/https://doi.org/10.1002/adhm.201701150.

(35)   Adeel, M.; Asif, K.; Rahman, M. M.; Daniele, S.; Canzonieri, V.; Rizzolio, F. Glucose Detection Devices and Methods Based on Metal–Organic Frameworks and Related Materials. *Adv. Funct. Mater.* **2021**, *31* (52), 2106023. https://doi.org/https://doi.org/10.1002/adfm.202106023.

(36)   Kim, J.; Campbell, A. S.; Wang, J. Wearable Non-Invasive Epidermal Glucose Sensors: A Review. *Talanta* **2018**, *177*, 163–170. https://doi.org/https://doi.org/10.1016/j.talanta.2017.08.077.

(37)   Tierney, M. J.; Tamada, J. A.; Potts, R. O.; Jovanovic, L.; Garg, S. Clinical Evaluation of the GlucoWatch® Biographer: A Continual, Non-Invasive Glucose Monitor for Patients with Diabetes. *Biosens. Bioelectron.* **2001**, *16* (9), 621–629. https://doi.org/https://doi.org/10.1016/S0956-5663(01)00189-0.

(38)   Arakawa, T.; Tomoto, K.; Nitta, H.; Toma, K.; Takeuchi, S.; Sekita, T.; Minakuchi, S.; Mitsubayashi, K. A Wearable Cellulose Acetate-Coated Mouthguard Biosensor for In Vivo Salivary Glucose Measurement. *Anal. Chem.* **2020**, *92* (18), 12201–12207. https://doi.org/10.1021/acs.analchem.0c01201.

(39)   Amine, A.; Arduini, F.; Moscone, D.; Palleschi, G. Recent Advances in Biosensors Based on Enzyme Inhibition. *Biosens. Bioelectron.* **2016**, *76*, 180–194. https://doi.org/https://doi.org/10.1016/j.bios.2015.07.010.

(40)   Van Dyk, J. S.; Pletschke, B. Review on the Use of Enzymes for the Detection of Organochlorine, Organophosphate and Carbamate Pesticides in the Environment. *Chemosphere* **2011**, *82* (3), 291–307. https://doi.org/https://doi.org/10.1016/j.chemosphere.2010.10.033.

(41)   Sassolas; Prieto-Simón, B.; Marty, J.-L. Biosensors for Pesticide Detection: New Trends. *Am. J. Anal. Chem.* **2012**, *3*, 210–232. https://doi.org/10.4236/ajac.2012.33030.

(42)   Arduini, F.; Cinti, S.; Caratelli, V.; Amendola, L.; Palleschi, G.; Moscone, D. Origami Multiple Paper-Based Electrochemical Biosensors for Pesticide Detection. *Biosens. Bioelectron.* **2019**, *126*, 346–354. https://doi.org/https://doi.org/10.1016/j.bios.2018.10.014.

(43)   Shu, Y.; Su, T.; Lu, Q.; Shang, Z.; Xu, Q.; Hu, X. Highly Stretchable Wearable Electrochemical Sensor Based on Ni-Co MOF Nanosheet-Decorated Ag/RGO/PU Fiber for Continuous Sweat Glucose Detection. *Anal. Chem.* **2021**, *93* (48), 16222–16230. https://doi.org/10.1021/acs.analchem.1c04106.

(44)   Hwang, D.-W.; Lee, S.; Seo, M.; Chung, T. D. Recent Advances in Electrochemical Non-Enzymatic Glucose Sensors – A Review. *Anal. Chim. Acta* **2018**, *1033*, 1–34. https://doi.org/https://doi.org/10.1016/j.aca.2018.05.051.

(45)   Raymundo-Pereira, P. A.; Gomes, N. O.; Shimizu, F. M.; Machado, S. A. S.; Oliveira, O. N. Selective and Sensitive Multiplexed Detection of Pesticides in Food Samples Using Wearable, Flexible Glove-Embedded Non-Enzymatic Sensors. *Chem. Eng. J.* **2021**, *408*, 127279. https://doi.org/https://doi.org/10.1016/j.cej.2020.127279.

(46)   Tunesi, M. M.; Kalwar, N.; Abbas, M. W.; Karakus, S.; Soomro, R. A.; Kilislioglu, A.; Abro, M. I.; Hallam, K. R. Functionalised CuO Nanostructures for the Detection of Organophosphorus Pesticides: A Non-Enzymatic Inhibition Approach Coupled with Nano-Scale Electrode Engineering to Improve Electrode Sensitivity. *Sensors Actuators B Chem.* **2018**, *260*, 480–489. https://doi.org/https://doi.org/10.1016/j.snb.2018.01.084.

(47)   Wang, J. *ANALYTICAL ELECTROCHEMISTRY*, Third Edit.; 2006.

(48)   Campuzano, S.; Yáñez-Sedeño, P.; Pingarrón, J. M. Electrochemical Affinity Biosensors Based on Selected Nanostructures for Food and Environmental Monitoring. *Sensors* **2020**, *20* (18). https://doi.org/10.3390/s20185125.

(49)   Xu, M.; Yadavalli, V. K. Flexible Biosensors for the Impedimetric Detection of Protein Targets Using Silk-Conductive Polymer Biocomposites. *ACS Sensors* **2019**, *4* (4), 1040–1047. https://doi.org/10.1021/acssensors.9b00230.

(50)   Vidic, J.; Manzano, M. Electrochemical Biosensors for Rapid Pathogen Detection. *Curr. Opin. Electrochem.* **2021**, *29*, 100750. https://doi.org/https://doi.org/10.1016/j.coelec.2021.100750.

(51)   Ganguly, A.; Lin, K. C.; Muthukumar, S.; Prasad, S. Autonomous, Real-Time Monitoring Electrochemical Aptasensor for Circadian Tracking of Cortisol Hormone in Sub-Microliter Volumes of Passively Eluted Human Sweat. *ACS Sensors* **2021**, *6* (1), 63–72. https://doi.org/10.1021/acssensors.0c01754.

(52)   Zhang, Q.; Jiang, D.; Xu, C.; Ge, Y.; Liu, X.; Wei, Q.; Huang, L.; Ren, X.; Wang, C.; Wang, Y. Wearable Electrochemical Biosensor Based on Molecularly Imprinted Ag Nanowires for Noninvasive Monitoring Lactate in Human Sweat. *Sensors Actuators B Chem.* **2020**, *320*, 128325. https://doi.org/https://doi.org/10.1016/j.snb.2020.128325.

(53)   Ozcelikay, G.; Kaya, S. I.; Ozkan, E.; Cetinkaya, A.; Nemutlu, E.; Kır, S.; Ozkan, S. A. Sensor-Based MIP Technologies for Targeted Metabolomics Analysis. *TrAC Trends Anal. Chem.* **2022**, *146*, 116487. https://doi.org/https://doi.org/10.1016/j.trac.2021.116487.

(54)   Li, X.; Yang, J.; Yuan, R.; Xiang, Y. Programming Cascaded Recycling Amplifications for Highly Sensitive and Label-Free Electrochemical Sensing of Transcription Factors in Tumor Cells. *Biosens. Bioelectron.* **2019**, *142*, 111574. https://doi.org/https://doi.org/10.1016/j.bios.2019.111574.

(55)   Altintas, Z.; Akgun, M.; Kokturk, G.; Uludag, Y. A Fully Automated Microfluidic-Based Electrochemical Sensor for Real-Time Bacteria Detection. *Biosens. Bioelectron.* **2018**, *100*, 541–548. https://doi.org/https://doi.org/10.1016/j.bios.2017.09.046.

(56)   Nagarajan, R. D.; Sundramoorthy, A. K. Recent Trends in Fabrication and Applications of Wearable Bioelectronics for Early-Stage Disease Monitoring and Diagnosis BT - Macro, Micro, and Nano-Biosensors: Potential Applications and Possible Limitations; Rai, M., Reshetilov, A., Plekhanova, Y., Ingle, A. P., Eds.; Springer International Publishing: Cham, 2021; pp 357–381. https://doi.org/10.1007/978-3-030-55490-3_18.

(57)   Guo, W.; Zhang, C.; Ma, T.; Liu, X.; Chen, Z.; Li, S.; Deng, Y. Advances in Aptamer Screening and Aptasensors' Detection of Heavy Metal Ions. *J. Nanobiotechnology* **2021**, *19* (1), 166. https://doi.org/10.1186/s12951-021-00914-4.

(58)   Petrucci, S.; Costa, C.; Broyles, D.; Dikici, E.; Daunert, S.; Deo, S. On-Site Detection of Food and Waterborne Bacteria – Current Technologies, Challenges, and Future Directions. *Trends Food Sci. Technol.* **2021**, *115*, 409–421. https://doi.org/https://doi.org/10.1016/j.tifs.2021.06.054.

(59)   Park, M.; Ha, H. D.; Kim, Y. T.; Jung, J. H.; Kim, S.-H.; Kim, D. H.; Seo, T. S. Combination of a Sample Pretreatment Microfluidic Device with a Photoluminescent Graphene Oxide Quantum Dot Sensor for Trace Lead Detection. *Anal. Chem.* **2015**, *87* (21), 10969–10975. https://doi.org/10.1021/acs.analchem.5b02907.

(60)   Rengaraj, S.; Cruz-Izquierdo, Á.; Scott, J. L.; Di Lorenzo, M. Impedimetric Paper-Based Biosensor for the Detection of Bacterial Contamination in Water. *Sensors Actuators B Chem.* **2018**, *265*, 50–58. https://doi.org/https://doi.org/10.1016/j.snb.2018.03.020.

(61)   Qi, J.; Li, B.; Zhou, N.; Wang, X.; Deng, D.; Luo, L.; Chen, L. The Strategy of Antibody-Free Biomarker Analysis by *in-Situ* Synthesized Molecularly Imprinted Polymers on Movable Valve Paper-Based Device. *Biosens. Bioelectron.* **2019**, *142*, 111533. https://doi.org/https://doi.org/10.1016/j.bios.2019.111533.

(62)   Lowe, B. M.; Sun, K.; Zeimpekis, I.; Skylaris, C.-K.; Green, N. G. Field-Effect Sensors – from PH Sensing to Biosensing: Sensitivity Enhancement Using Streptavidin–Biotin as a Model System. *Analyst* **2017**, *142* (22), 4173–4200. https://doi.org/10.1039/C7AN00455A.

(63)   Wang, L.; Estrela, P.; Huq, E.; Li, P.; Thomas, S.; Ferrigno, P. K.; Paul, D.; Adkin, P.; Migliorato, P. Fabrication of BioFET Linear Array for Detection of Protein Interactions. *Microelectron. Eng.* **2010**, *87* (5), 753–755. https://doi.org/https://doi.org/10.1016/j.mee.2009.11.148.

(64)   Wikipedia. Bio-FET.

(65)   Béraud, A.; Sauvage, M.; Bazán, C. M.; Tie, M.; Bencherif, A.; Bouilly, D. Graphene Field-Effect Transistors as Bioanalytical Sensors: Design, Operation and Performance. *Analyst* **2021**, *146* (2), 403–428. https://doi.org/10.1039/d0an01661f.

(66)   Liu, S.; Guo, X. Carbon Nanomaterials Field-Effect-Transistor-Based Biosensors. *NPG Asia Mater.* **2012**, *4* (8), e23–e23. https://doi.org/10.1038/am.2012.42.

(67)   An, J. E.; Kim, K. H.; Park, S. J.; Seo, S. E.; Kim, J.; Ha, S.; Bae, J.; Kwon, O. S. Wearable Cortisol Aptasensor for Simple and Rapid Real-Time Monitoring. *ACS Sensors* **2022**, *7* (1), 99–108. https://doi.org/10.1021/acssensors.1c01734.

(68)   Liu, C.; Wei, X.; Hao, S.; Zong, B.; Chen, X.; Li, Z.; Mao, S. Label-Free, Fast Response, and Simply Operated Silver Ion Detection with a Ti3C2Tx MXene Field-Effect Transistor. *Anal. Chem.* **2021**, *93* (22), 8010–8018. https://doi.org/10.1021/acs.analchem.1c01094.

(69)   Hu, C.; Yu, X.; Li, Y.; Cheng, J.; Li, Q.; Xiao, B. Bandgap Engineering of Strained S-Terminated MXene and Its Promising Application as NOx Gas Sensor. *Appl. Surf. Sci.* **2022**, *592*, 153296. https://doi.org/https://doi.org/10.1016/j.apsusc.2022.153296.

(70)   Tian, W.; Liu, X.; Yu, W. Research Progress of Gas Sensor Based on Graphene and Its Derivatives: A Review. *Applied Sciences* . 2018. https://doi.org/10.3390/app8071118.

(71)   Krivetskiy, V.; Rumyantseva, M.; Gaskov, A. Design, Synthesis and Application of Metal Oxide-Based Sensing Elements: A Chemical Principles Approach. In *Metal Oxide Nanomaterials for Chemical Sensors*; Carpenter, M. A., Kolmakov, A., Mathur, S., Eds.; 2014; Vol. 7, pp 69–116. https://doi.org/10.1007/978-1-4614-5395-6.

(72)   Gurlo, A. Insights into the Mechanism of Gas Sensor Operation. In *Metal Oxide Nanomaterials for Chemical Sensors*; Carpenter, M. A., Kolmakov, A., Mathur, S., Eds.; 2014; pp 35–68. https://doi.org/10.1007/978-1-4614-5395-6.

(73)   Choopun, S. Metal-Oxide Nanowires for Gas Sensors; Hongsith, N., Ed.; IntechOpen: Rijeka, 2012; p Ch. 1. https://doi.org/10.5772/54385.

(74)   Kim, D.; Shin, W.; Hong, S.; Jeong, Y.; Jung, G.; Park, J.; Lee, J.-H. Effects of Electrode Structure on H_2S Sensing and Low-Frequency Noise Characteristics in In_2O_3-Based Resistor-Type Gas Sensors. *IEEE Sens. J.* **2022**, *22* (7), 6311–6320. https://doi.org/10.1109/JSEN.2022.3154417.

(75)   Khan, M. A.; Rao, M. V; Li, Q. Recent Advances in Electrochemical Sensors for Detecting Toxic Gases: NO2, SO2 and H2S. *Sensors* . 2019. https://doi.org/10.3390/s19040905.

(76)   Saruhan, B.; Lontio Fomekong, R.; Nahirniak, S. Review: Influences of Semiconductor Metal Oxide Properties on Gas Sensing Characteristics. *Front. Sensors* **2021**, *2*. https://doi.org/10.3389/fsens.2021.657931.

(77)   Li, W.; Chen, R.; Qi, W.; Cai, L.; Sun, Y.; Sun, M.; Li, C.; Yang, X.; Xiang, L.; Xie, D.; Ren, T. Reduced Graphene Oxide/Mesoporous ZnO NSs Hybrid Fibers for Flexible, Stretchable, Twisted, and Wearable NO2 E-Textile Gas Sensor. *ACS Sensors* **2019**, *4* (10), 2809–2818. https://doi.org/10.1021/acssensors.9b01509.

(78)   Zhou, X.; Xue, Z.; Chen, X.; Huang, C.; Bai, W.; Lu, Z.; Wang, T. Nanomaterial-Based Gas Sensors Used for Breath Diagnosis. *J. Mater. Chem. B* **2020**, *8* (16), 3231–3248. https://doi.org/10.1039/C9TB02518A.

(79)   Chan, M.-J.; Li, Y.-J.; Wu, C.-C.; Lee, Y.-C.; Zan, H.-W.; Meng, H.-F.; Hsieh, M.-H.; Lai, C.-S.; Tian, Y.-C. Breath Ammonia Is a Useful Biomarker Predicting Kidney Function in Chronic Kidney Disease Patients. *Biomedicines* . 2020. https://doi.org/10.3390/biomedicines8110468.

(80)   Shan, B.; Broza, Y. Y.; Li, W.; Wang, Y.; Wu, S.; Liu, Z.; Wang, J.; Gui, S.; Wang, L.; Zhang, Z.; Liu, W.; Zhou, S.; Jin, W.; Zhang, Q.; Hu, D.; Lin, L.; Zhang, Q.; Li, W.; Wang, J.; Liu, H.; Pan, Y.; Haick, H. Multiplexed Nanomaterial-Based Sensor Array for Detection of COVID-19 in Exhaled Breath. *ACS Nano* **2020**, *14* (9), 12125–12132. https://doi.org/10.1021/acsnano.0c05657.

(81)   Tat, T.; Chen, K.; Nashalian, A.; Chen, J. Wearable Physical Sensors. In *Wearable Physical, Chemical and Biological Sensors*; Moráles-Narvaez, E., Dincer, C., Eds.; 2022; pp 183–217.

(82)   Steccanella, L.; Bloisi, D. D.; Castellini, A.; Farinelli, A. Waterline and Obstacle Detection in Images from Low-Cost Autonomous Boats for Environmental Monitoring. *Rob. Auton. Syst.* **2020**, *124*, 103346. https://doi.org/https://doi.org/10.1016/j.robot.2019.103346.

(83)   Heo, S. Y.; Kim, J.; Gutruf, P.; Banks, A.; Wei, P.; Pielak, R.; Balooch, G.; Shi, Y.; Araki, H.; Rollo, D.; Gaede, C.; Patel, M.; Kwak, J. W.; Peña-Alcántara, A. E.; Lee, K.-T.; Yun, Y.; Robinson, J. K.; Xu, S.; Rogers, J. A. Wireless, Battery-Free, Flexible, Miniaturized Dosimeters Monitor Exposure to Solar Radiation and to Light for Phototherapy. *Sci. Transl. Med.* **2018**, *10* (470), 1643. https://doi.org/10.1126/scitranslmed.aau1643.

(84)   Zhang, D.; Wang, D.; Xu, Z.; Zhang, X.; Yang, Y.; Guo, J.; Zhang, B.; Zhao, W. Diversiform Sensors and Sensing Systems Driven by Triboelectric and Piezoelectric Nanogenerators. *Coord. Chem. Rev.* **2021**, *427*, 213597. https://doi.org/https://doi.org/10.1016/j.ccr.2020.213597.

(85)   Luo, J.; Gao, W.; Wang, Z. L. The Triboelectric Nanogenerator as an Innovative Technology toward Intelligent Sports. *Adv. Mater.* **2021**, *33* (17), 2004178. https://doi.org/https://doi.org/10.1002/adma.202004178.

(86)   Zhong, J.; Li, Z.; Takakuwa, M.; Inoue, D.; Hashizume, D.; Jiang, Z.; Shi, Y.; Ou, L.; Nayeem, M. O. G.; Umezu, S.; Fukuda, K.; Someya, T. Smart Face Mask Based on an Ultrathin Pressure Sensor for Wireless Monitoring of Breath Conditions. *Adv. Mater.* **2022**, *34* (6), 2107758. https://doi.org/https://doi.org/10.1002/adma.202107758.

(87)   Franssila, S. *Introduction to Microfabrication*, Second Edi.; John Wiley & Sons Ltd, 2010. https://doi.org/10.1002/9781119990413.

(88)   Hong, F.; Blaikie, R. Plasmonic Lithography: Recent Progress. *Adv. Opt. Mater.* **2019**, *7* (14), 1801653. https://doi.org/https://doi.org/10.1002/adom.201801653.

(89)   Circuitnow. 5 Important Events in the History of Circuit Boards.

(90)   Cui, Z. *Printed Electronics*; Cui, Z., Ed.; John Wiley & Sons Singapore Pte. Ltd., 2016.

(91)   Ridley, B. A.; Nivi, B.; Jacobson, J. M. All-Inorganic Field Effect Transistors Fabricated by Printing. *Science (80-.).* **1999**, *286* (5440), 746–749. https://doi.org/10.1126/science.286.5440.746.

(92)   Nagar, B. Printed Graphene for Energy Storage and Sensing Applications, 2019.

(93)   Suganuma, K. *Introduction to Printed Electronics*; 2014; Vol. 74.

(94)   Nag, A.; Mukhopadhyay, S. C.; Kosel, J. *Printed Flexible Sensors*; 2019; Vol. 33.

(95)   Wu, Y.; Liu, P.; Ong, B. S.; Srikumar, T.; Zhao, N.; Botton, G.; Zhu, S. Controlled Orientation of Liquid-Crystalline Polythiophene Semiconductors for High-Performance Organic Thin-Film Transistors. *Appl. Phys. Lett.* **2005**, *86* (14), 142102. https://doi.org/10.1063/1.1894597.

(96)   Ong, B. S.; Wu, Y.; Liu, P.; Gardner, S. High-Performance Semiconducting Polythiophenes for Organic Thin-Film Transistors. *J. Am. Chem. Soc.* **2004**, *126* (11), 3378–3379. https://doi.org/10.1021/ja039772w.

(97)   Ortiz, R. P.; Facchetti, A.; Marks, T. J. High-k Organic, Inorganic, and Hybrid Dielectrics for Low-Voltage Organic Field-Effect Transistors. *Chem. Rev.* **2010**, *110* (1), 205–239. https://doi.org/10.1021/cr9001275.

(98)   Park, J. H.; Yoo, Y. B.; Lee, K. H.; Jang, W. S.; Oh, J. Y.; Chae, S. S.; Baik, H. K. Low-Temperature, High-Performance Solution-Processed Thin-Film Transistors with Peroxo-Zirconium Oxide Dielectric. *ACS Appl. Mater. Interfaces* **2013**, *5* (2), 410–417. https://doi.org/10.1021/am3022625.

(99)   Kim, J.; Kumar, R.; Bandodkar, A. J.; Wang, J. Advanced Materials for Printed Wearable Electrochemical Devices: A Review. *Adv. Electron. Mater.* **2017**, *3* (1), 1600260. https://doi.org/https://doi.org/10.1002/aelm.201600260.

(100)   Kim, J.; Kumar, R.; Bandodkar, A. J.; Wang, J. Advanced Materials for Printed Wearable Electrochemical Devices: A Review. *Advanced Electronic Materials*. Blackwell Publishing Ltd January 1, 2017. https://doi.org/10.1002/aelm.201600260.

(101)   Sfragano, P. S.; Laschi, S.; Palchetti, I. Sustainable Printed Electrochemical Platforms for Greener Analytics. *Front. Chem.* **2020**, *8*. https://doi.org/10.3389/fchem.2020.00644.

(102)   SunChemical. Advanced Materials.

(103)   Dawkins, R. C.; Wen, D.; Hart, J. N.; Vepsäläinen, M. A Screen-Printed Ag/AgCl Reference Electrode with Long-Term Stability for Electroanalytical Applications. *Electrochim. Acta* **2021**, *393*, 139043. https://doi.org/https://doi.org/10.1016/j.electacta.2021.139043.

(104)   Ke, S.-H.; Guo, P.-W.; Pang, C.-Y.; Tian, B.; Luo, C.-S.; Zhu, H.-P.; Wu, W. Screen-Printed Flexible Strain Sensors with Ag Nanowires for Intelligent and Tamper-Evident Packaging Applications. *Adv. Mater. Technol.* **2020**, *5* (5), 1901097. https://doi.org/https://doi.org/10.1002/admt.201901097.

(105)   Bandodkar, A. J.; Jeerapan, I.; You, J.-M.; Nuñez-Flores, R.; Wang, J. Highly Stretchable Fully-Printed CNT-Based Electrochemical Sensors and Biofuel Cells: Combining Intrinsic and Design-Induced Stretchability. *Nano Lett.* **2016**, *16* (1), 721–727. https://doi.org/10.1021/acs.nanolett.5b04549.

(106)   Shitanda, I.; Kato, S.; Hoshi, Y.; Itagaki, M.; Tsujimura, S. Flexible and High-Performance Paper-Based Biofuel Cells Using Printed Porous Carbon Electrodes. *Chem. Commun.* **2013**, *49* (94), 11110–11112. https://doi.org/10.1039/C3CC46644B.

(107)   Hyun, W. J.; Secor, E. B.; Hersam, M. C.; Frisbie, C. D.; Francis, L. F. High-Resolution Patterning of Graphene by Screen Printing with a Silicon Stencil for Highly Flexible Printed Electronics. *Adv. Mater.* **2015**, *27* (1), 109–115. https://doi.org/https://doi.org/10.1002/adma.201404133.

(108)   Honeychurch, K. C.; Hart, J. P. Screen-Printed Electrochemical Sensors for Monitoring Metal Pollutants. *TrAC - Trends Anal. Chem.* **2003**, *22* (7), 456–469. https://doi.org/10.1016/S0165-9936(03)00703-9.

(109)   Vu, Q. K.; Tran, Q. H.; Vu, N. P.; Anh, T.-L.; Dang, T. T. Le; Matteo, T.; Nguyen, T. H. H. A Label-Free Electrochemical Biosensor Based on Screen-Printed Electrodes Modified with Gold Nanoparticles for Quick Detection of Bacterial Pathogens. *Mater. Today Commun.* **2021**, *26*, 101726. https://doi.org/https://doi.org/10.1016/j.mtcomm.2020.101726.

(110)   Sher, M.; Faheem, A.; Asghar, W.; Cinti, S. Nano-Engineered Screen-Printed Electrodes: A Dynamic Tool for Detection of Viruses. *TrAC Trends Anal. Chem.* **2021**, *143*, 116374. https://doi.org/https://doi.org/10.1016/j.trac.2021.116374.

(111)   Seiko Epson Corporation. Micro Piezo Inkjet Technology.

(112)   Tortorich, R. P.; Shamkhalichenar, H.; Choi, J. W. Inkjet-Printed and Paper-Based Electrochemical Sensors. *Appl. Sci.* **2018**, *8* (2). https://doi.org/10.3390/app8020288.

(113)   Kamyshny, A.; Magdassi, S. Metallic Nanoinks for Inkjet Printing of Conductive 2D and 3D Structures. *Nanomaterials for 2D and 3D Printing*. April 10, 2017, pp 119–160. https://doi.org/https://doi.org/10.1002/9783527685790.ch7.

(114)   Godard, N.; Mahjoub, M. A.; Girod, S.; Schenk, T.; Glinšek, S.; Defay, E. On the Importance of Pyrolysis for Inkjet-Printed Oxide Piezoelectric Thin Films. *J. Mater. Chem. C* **2020**, *8* (11), 3740–3747. https://doi.org/10.1039/C9TC05228C.

(115)   Wikipedia. Wetting.

(116)   Lemarchand, J.; Bridonneau, N.; Battaglini, N.; Carn, F.; Mattana, G.; Piro, B.; Zrig, S.; Noël, V. Challenges, Prospects, and Emerging Applications of Inkjet-Printed Electronics: A Chemist's Point of View. *Angew. Chemie Int. Ed.* **2022**, *61* (20), e202200166. https://doi.org/https://doi.org/10.1002/anie.202200166.

(117)   Wolfgang Clemens. *White Paper: OE-A Roadmap for Organic and Printed Electronics, 3rd Edition*; 2009.

(118)   Rosati, G.; Ravarotto, M.; Scaramuzza, M.; De Toni, A.; Paccagnella, A. Silver Nanoparticles Inkjet-Printed Flexible Biosensor for Rapid Label-Free Antibiotic Detection in Milk. *Sensors Actuators B Chem.* **2019**, *280*, 280–289. https://doi.org/https://doi.org/10.1016/j.snb.2018.09.084.

(119)   Rosati, G.; Ravarotto, M.; Sanavia, M.; Scaramuzza, M.; De Toni, A.; Paccagnella, A. Inkjet Sensors Produced by Consumer Printers with Smartphone Impedance Readout. *Sens. Bio-Sensing Res.* **2019**, *26*, 100308. https://doi.org/https://doi.org/10.1016/j.sbsr.2019.100308.

(120)   Li, X.; Liu, B.; Pei, B.; Chen, J.; Zhou, D.; Peng, J.; Zhang, X.; Jia, W.; Xu, T. Inkjet Bioprinting of Biomaterials. *Chem. Rev.* **2020**, *120* (19), 10793–10833. https://doi.org/10.1021/acs.chemrev.0c00008.

(121)   FUJIFILM Dimatix Inc. *Dimatix Materials Printer DMP-2800 Series User Manual*; 2006.

(122)   Soltman, D.; Subramanian, V. Inkjet-Printed Line Morphologies and Temperature Control of the Coffee Ring Effect. *Langmuir* **2008**, *24* (5), 2224–2231. https://doi.org/10.1021/la7026847.

(123)   Nautasign. HP Thermal Inkjet vs piezo printheads the technology behind HP Latex printing https://www.youtube.com/watch?v=wnfkOHUup2Q.

(124)   Atul pasare. How inkjet printer work https://www.youtube.com/watch?v=9yeZSaigBj4.

(125)   Rosati, G.; Urban, M.; Zhao, L.; Yang, Q.; de Carvalho Castro e Silva, C.; Bonaldo, S.; Parolo, C.; Nguyen, E. P.; Ortega, G.; Fornasiero, P.; Paccagnella, A.; Merkoçi, A. A Plug, Print & Play Inkjet Printing and Impedance-Based Biosensing Technology Operating through a Smartphone for Clinical Diagnostics. *Biosens. Bioelectron.* **2022**, *196*, 113737. https://doi.org/https://doi.org/10.1016/j.bios.2021.113737.

(126)   NovaCentrix. Conductive Inks.

(127)   Mitsubishi Paper Mills Limited. Silver Nano.

(128)   Xerox Corporation. Xerox® ColorQube® 8880 Color Printer.

(129)   Lu, Y.; Shi, W.; Jiang, L.; Qin, J.; Lin, B. Rapid Prototyping of Paper-Based Microfluidics with Wax for Low-Cost, Portable Bioassay. *Electrophoresis* **2009**, *30* (9), 1497–1500. https://doi.org/https://doi.org/10.1002/elps.200800563.

(130)   Baptista-Pires, L.; Mayorga-Martínez, C. C.; Medina-Sánchez, M.; Montón, H.; Merkoçi, A. Water Activated Graphene Oxide Transfer Using Wax Printed Membranes for Fast Patterning of a Touch Sensitive Device. *ACS Nano* **2016**, *10* (1), 853–860. https://doi.org/10.1021/acsnano.5b05963.

(131)   Nagar, B.; Balsells, M.; de la Escosura-Muñiz, A.; Gomez-Romero, P.; Merkoçi, A. Fully Printed One-Step Biosensing Device Using Graphene/AuNPs Composite. *Biosens. Bioelectron.* **2019**, *129*, 238–244. https://doi.org/https://doi.org/10.1016/j.bios.2018.09.073.

(132)   Bariya, M.; Shahpar, Z.; Park, H.; Sun, J.; Jung, Y.; Gao, W.; Nyein, H. Y. Y.; Liaw, T. S.; Tai, L.-C.; Ngo, Q. P.; Chao, M.; Zhao, Y.; Hettick, M.; Cho, G.; Javey, A. Roll-to-Roll Gravure Printed Electrochemical Sensors for Wearable and Medical Devices. *ACS Nano* **2018**, *12* (7), 6978–6987. https://doi.org/10.1021/acsnano.8b02505.

(133)   Hernández-Rodríguez, J. F.; Della Pelle, F.; Rojas, D.; Compagnone, D.; Escarpa, A. Xurography-Enabled Thermally Transferred Carbon Nanomaterial-Based Electrochemical Sensors on Polyethylene Terephthalate–Ethylene Vinyl Acetate Films. *Anal. Chem.* **2020**, *92* (19), 13565–13572. https://doi.org/10.1021/acs.analchem.0c03240.

(134)   Nguyen, H. A. D.; Lee, J.; Kim, C. H.; Shin, K.-H.; Lee, D. An Approach for Controlling Printed Line-Width in High Resolution Roll-to-Roll Gravure Printing. *J. Micromechanics Microengineering* **2013**, *23* (9), 95010. https://doi.org/10.1088/0960-1317/23/9/095010.

(135)   Griffiths, K.; Dale, C.; Hedley, J.; Kowal, M. D.; Kaner, R. B.; Keegan, N. Laser-Scribed Graphene Presents an Opportunity to Print a New Generation of Disposable Electrochemical Sensors. *Nanoscale* **2014**, *6* (22), 13613–13622. https://doi.org/10.1039/C4NR04221B.

(136)   Lin, J.; Peng, Z.; Liu, Y.; Ruiz-Zepeda, F.; Ye, R.; Samuel, E. L. G.; Yacaman, M. J.; Yakobson, B. I.; Tour, J. M. Laser-Induced Porous Graphene Films from Commercial Polymers. *Nat. Commun.* **2014**, *5* (1), 5714. https://doi.org/10.1038/ncomms6714.

(137)   Ko, Y.; Lee, G.; Kim, M. J.; Lee, D. Y.; Nam, J.; Jang, A.-R.; Lee, J.-O.; Kim, K. S. Direct Pattern Growth of Carbon Nanomaterials by Laser Scribing on Spin-Coated Cu-PI Composite Films and Their Gas Sensor Application. *Materials (Basel).* **2021**, *14* (12). https://doi.org/10.3390/ma14123388.

(138)   Vaughan, E.; Larrigy, C.; Burke, M.; Sygellou, L.; Quinn, A. J.; Galiotis, C.; Iacopino, D. Visible Laser Scribing Fabrication of Porous Graphitic Carbon Electrodes: Morphologies, Electrochemical Properties, and Applications as Disposable Sensor Platforms. *ACS Appl. Electron. Mater.* **2020**, *2* (10), 3279–3288. https://doi.org/10.1021/acsaelm.0c00612.

(139)   Zhu, Y.; Cai, H.; Ding, H.; Pan, N.; Wang, X. Fabrication of Low-Cost and Highly Sensitive Graphene-Based Pressure Sensors by Direct Laser Scribing Polydimethylsiloxane. *ACS Appl. Mater. Interfaces* **2019**, *11* (6), 6195–6200. https://doi.org/10.1021/acsami.8b17085.

(140)   Yang, W.; Zhao, W.; Li, Q.; Li, H.; Wang, Y.; Li, Y.; Wang, G. Fabrication of Smart Components by 3D Printing and Laser-Scribing Technologies. *ACS Appl. Mater. Interfaces* **2020**, *12* (3), 3928–3935. https://doi.org/10.1021/acsami.9b17467.

(141)   Wan, Z.; Nguyen, N.-T.; Gao, Y.; Li, Q. Laser Induced Graphene for Biosensors. *Sustain. Mater. Technol.* **2020**, *25*, e00205. https://doi.org/https://doi.org/10.1016/j.susmat.2020.e00205.

(142)   Cheng, L.; Guo, W.; Cao, X.; Dou, Y.; Huang, L.; Song, Y.; Su, J.; Zeng, Z.; Ye, R. Laser-Induced Graphene for Environmental Applications: Progress and Opportunities. *Mater. Chem. Front.* **2021**, *5* (13), 4874–4891. https://doi.org/10.1039/D1QM00437A.

(143)   Rodrigues, J.; Zanoni, J.; Gaspar, G.; Fernandes, A. J. S.; Carvalho, A. F.; Santos, N. F.; Monteiro, T.; Costa, F. M. ZnO Decorated Laser-Induced Graphene Produced by Direct Laser Scribing. *Nanoscale Adv.* **2019**, *1* (8), 3252–3268. https://doi.org/10.1039/C8NA00391B.

(144)   Giacomelli, C.; Álvarez-Diduk, R.; Testolin, A.; Merkoçi, A. Selective Stamping of Laser Scribed RGO Nanofilms: From Sensing to Multiple Applications. *2D Mater.* **2020**, *7* (2), 24006. https://doi.org/10.1088/2053-1583/ab68a7.

(145)   Harish, V.; Tewari, D.; Gaur, M.; Yadav, A. B.; Swaroop, S.; Bechelany, M.; Barhoum, A. Review on Nanoparticles and Nanostructured Materials: Bioimaging, Biosensing, Drug Delivery, Tissue Engineering, Antimicrobial, and Agro-Food Applications. *Nanomaterials* . 2022. https://doi.org/10.3390/nano12030457.

(146)   Roduner, E. Size Matters: Why Nanomaterials Are Different. *Chem. Soc. Rev.* **2006**, *35* (7), 583–592. https://doi.org/10.1039/B502142C.

(147)   Guo, W.; Liu, Y.; Meng, X.; Pei, M.; Wang, J.; Wang, L. A Novel Signal Amplification Strategy of an Electrochemical Immunosensor for Human Chorionic Gonadotropin{,} Based on Nanocomposites of Multi-Walled Carbon Nanotubes–Ionic Liquid and Nanoporous Pd. *RSC Adv.* **2014**, *4* (101), 57773–57780. https://doi.org/10.1039/C4RA09791B.

(148)   Cao, X.; Ye, Y.; Liu, S. Gold Nanoparticle-Based Signal Amplification for Biosensing. *Anal. Biochem.* **2011**, *417* (1), 1–16. https://doi.org/https://doi.org/10.1016/j.ab.2011.05.027.

(149)   Ganguly, P.; Breen, A.; Pillai, S. C. Toxicity of Nanomaterials: Exposure, Pathways, Assessment, and Recent Advances. *ACS Biomater. Sci. Eng.* **2018**, *4* (7), 2237–2275. https://doi.org/10.1021/acsbiomaterials.8b00068.

(150)   Lewinski, N.; Colvin, V.; Drezek, R. Cytotoxicity of Nanoparticles. *Small* **2008**, *4* (1), 26–49. https://doi.org/https://doi.org/10.1002/smll.200700595.

(151)   Jia, G.; Wang, H.; Yan, L.; Wang, X.; Pei, R.; Yan, T.; Zhao, Y.; Guo, X. Cytotoxicity of Carbon Nanomaterials: Single-Wall Nanotube, Multi-Wall Nanotube, and Fullerene. *Environ. Sci. Technol.* **2005**, *39* (5), 1378–1383. https://doi.org/10.1021/es048729l.

(152)   Martín, C.; Kostarelos, K.; Prato, M.; Bianco, A. Biocompatibility and Biodegradability of 2D Materials: Graphene and Beyond. *Chem. Commun.* **2019**, *55* (39), 5540–5546. https://doi.org/10.1039/C9CC01205B.

(153)   Polsky, R.; Gill, R.; Kaganovsky, L.; Willner, I. Nucleic Acid-Functionalized Pt Nanoparticles: Catalytic Labels for the Amplified Electrochemical Detection of Biomolecules. *Anal. Chem.* **2006**, *78* (7), 2268–2271. https://doi.org/10.1021/ac0519864.

(154)   Weber, B.; Mahapatra, S.; Ryu, H.; Lee, S.; Fuhrer, A.; Reusch, T. C. G.; Thompson, D. L.; Lee, W. C. T.; Klimeck, G.; Hollenberg, L. C. L.; Simmons, M. Y. Ohm's Law Survives to the Atomic Scale. *Science (80-.).* **2012**, *335* (6064), 64–67. https://doi.org/10.1126/science.1214319.

(155)   Liao, Y.; Zhang, C.; Wang, X.; Li, X.-G.; Ippolito, S. J.; Kalantar-zadeh, K.; Kaner, R. B. Carrier Mobility of Single-Walled Carbon Nanotube-Reinforced Polyaniline Nanofibers. *J. Phys. Chem. C* **2011**, *115* (32), 16187–16192. https://doi.org/10.1021/jp2053585.

(156)   Mir, S. H.; Yadav, V. K.; Singh, J. K. Recent Advances in the Carrier Mobility of Two-Dimensional Materials: A Theoretical Perspective. *ACS Omega* **2020**, *5* (24), 14203–14211. https://doi.org/10.1021/acsomega.0c01676.

(157)   Geim, A. K.; Novoselov, K. S. The Rise of Graphene. *Nat. Mater.* **2007**, *6* (3), 183–191. https://doi.org/10.1038/nmat1849.

(158)   Dürkop, T.; Getty, S. A.; Cobas, E.; Fuhrer, M. S. Extraordinary Mobility in Semiconducting Carbon Nanotubes. *Nano Lett.* **2004**, *4* (1), 35–39. https://doi.org/10.1021/nl034841q.

(159)   Liu, H.; Li, Y.; Dai, K.; Zheng, G.; Liu, C.; Shen, C.; Yan, X.; Guo, J.; Guo, Z. Electrically Conductive Thermoplastic Elastomer Nanocomposites at Ultralow Graphene Loading Levels for Strain Sensor Applications. *J. Mater. Chem. C* **2016**, *4* (1), 157–166. https://doi.org/10.1039/C5TC02751A.

(160)   Yao, S.; Zhu, Y. Wearable Multifunctional Sensors Using Printed Stretchable Conductors Made of Silver Nanowires. *Nanoscale* **2014**, *6* (4), 2345–2352. https://doi.org/10.1039/C3NR05496A.

(161)   Pantano, M. F.; Kuljanishvili, I. Advances in Mechanical Characterization of 1D and 2D Nanomaterials: Progress and Prospects. *Nano Express* **2020**, *1* (2), 22001. https://doi.org/10.1088/2632-959x/abb43e.

(162)   Gul, S.; Khan, S. B.; Rehman, I. U.; Khan, M. A.; Khan, M. I. A Comprehensive Review of Magnetic Nanomaterials Modern Day Theranostics. *Front. Mater.* **2019**, *6*. https://doi.org/10.3389/fmats.2019.00179.

(163)   Gong, S.; Cheng, W. One-Dimensional Nanomaterials for Soft Electronics. *Adv. Electron. Mater.* **2017**, *3* (3), 1600314. https://doi.org/https://doi.org/10.1002/aelm.201600314.

(164)   Samal, R.; Rout, C. S. Chapter 12 - Wearable and Flexible Sensors Based on 2D and Nanomaterials. In *Woodhead Publishing Series in Electronic and Optical Materials*; Hywel, M., Rout, C. S., Late, D. J. B. T.-F. and S. A. of 2D M., Eds.; Woodhead Publishing, 2019; pp 437–463. https://doi.org/https://doi.org/10.1016/B978-0-08-102577-2.00012-9.

(165)   Makhlouf, A. S. H.; Barhoum, A. *Emerging Applications of Nanoparticles and Architectural Nanostructures*, 1st Editio.; 2018.

(166)   Yang, Q.; Nguyen, E. P.; Silva, C. de C. C.; Rosati, G.; Merkoçi, A. Signal Enhancement Strategies. In *Wearable Physical, Chemical and Biological Sensors*; Moráles-Narvaez, E., Dincer, C., Eds.; 2022.

(167)   Quesada-González, D.; Stefani, C.; González, I.; de la Escosura-Muñiz, A.; Domingo, N.; Mutjé, P.; Merkoçi, A. Signal Enhancement on Gold Nanoparticle-Based Lateral Flow Tests Using Cellulose Nanofibers. *Biosens. Bioelectron.* **2019**, *141*, 111407. https://doi.org/https://doi.org/10.1016/j.bios.2019.111407.

(168)   Zamora-Gálvez, A.; Ait-Lahcen, A.; Mercante, L. A.; Morales-Narváez, E.; Amine, A.; Merkoçi, A. Molecularly Imprinted Polymer-Decorated Magnetite Nanoparticles for Selective Sulfonamide Detection. *Anal. Chem.* **2016**, *88* (7), 3578–3584. https://doi.org/10.1021/acs.analchem.5b04092.

(169)   Bujes-Garrido, J.; Izquierdo-Bote, D.; Heras, A.; Colina, A.; Arcos-Martínez, M. J. Determination of Halides Using Ag Nanoparticles-Modified Disposable Electrodes. A First Approach to a Wearable Sensor for Quantification of Chloride Ions. *Anal. Chim. Acta* **2018**, *1012*, 42–48. https://doi.org/https://doi.org/10.1016/j.aca.2018.01.063.

(170)   Gong, S.; Schwalb, W.; Wang, Y.; Chen, Y.; Tang, Y.; Si, J.; Shirinzadeh, B.; Cheng, W. A Wearable and Highly Sensitive Pressure Sensor with Ultrathin Gold Nanowires. *Nat. Commun.* **2014**, *5* (1), 3132. https://doi.org/10.1038/ncomms4132.

(171)   Yamada, T.; Hayamizu, Y.; Yamamoto, Y.; Yomogida, Y.; Izadi-Najafabadi, A.; Futaba, D. N.; Hata, K. A Stretchable Carbon Nanotube Strain Sensor for Human-Motion Detection. *Nat. Nanotechnol.* **2011**, *6* (5), 296–301. https://doi.org/10.1038/nnano.2011.36.

(172)   Yang, Z.; Dou, X. Emerging and Future Possible Strategies for Enhancing 1D Inorganic Nanomaterials-Based Electrical Sensors towards Explosives Vapors Detection. *Adv. Funct. Mater.* **2016**, *26* (15), 2406–2425. https://doi.org/https://doi.org/10.1002/adfm.201504846.

(173)   Yanagi, K. Chapter 3 - Differentiation of Carbon Nanotubes with Different Chirality; Tanaka, K., Iijima, S. B. T.-C. N. and G. (Second E., Eds.; Elsevier: Oxford, 2014; pp 19–38. https://doi.org/https://doi.org/10.1016/B978-0-08-098232-8.00003-6.

(174)   Mannoor, M. S.; Tao, H.; Clayton, J. D.; Sengupta, A.; Kaplan, D. L.; Naik, R. R.; Verma, N.; Omenetto, F. G.; McAlpine, M. C. Graphene-Based Wireless Bacteria Detection on Tooth Enamel. *Nat. Commun.* **2012**, *3* (1), 763. https://doi.org/10.1038/ncomms1767.

(175)   Dankerl, M.; Hauf, M. V; Lippert, A.; Hess, L. H.; Birner, S.; Sharp, I. D.; Mahmood, A.; Mallet, P.; Veuillen, J.-Y.; Stutzmann, M.; Garrido, J. A. Graphene Solution-Gated Field-Effect Transistor Array for Sensing Applications. *Adv. Funct. Mater.* **2010**, *20* (18), 3117–3124. https://doi.org/https://doi.org/10.1002/adfm.201000724.

(176)   Hess, L. H.; Lyuleeva, A.; Blaschke, B. M.; Sachsenhauser, M.; Seifert, M.; Garrido, J. A.; Deubel, F. Graphene Transistors with Multifunctional Polymer Brushes for Biosensing Applications. *ACS Appl. Mater. Interfaces* **2014**, *6* (12), 9705–9710. https://doi.org/10.1021/am502112x.

(177)   Mas-Ballesté, R.; Gómez-Navarro, C.; Gómez-Herrero, J.; Zamora, F. 2D Materials: To Graphene and Beyond. *Nanoscale* **2011**, *3* (1), 20–30. https://doi.org/10.1039/C0NR00323A.

(178)   Eda, G.; Yamaguchi, H.; Voiry, D.; Fujita, T.; Chen, M.; Chhowalla, M. Photoluminescence from Chemically Exfoliated MoS2. *Nano Lett.* **2011**, *11* (12), 5111–5116. https://doi.org/10.1021/nl201874w.

(179)   Xue, F.; Chen, L.; Wang, L.; Pang, Y.; Chen, J.; Zhang, C.; Wang, Z. L. MoS2 Tribotronic Transistor for Smart Tactile Switch. *Adv. Funct. Mater.* **2016**, *26* (13), 2104–2109. https://doi.org/https://doi.org/10.1002/adfm.201504485.

(180)   Singh, E.; Singh, P.; Kim, K. S.; Yeom, G. Y.; Nalwa, H. S. Flexible Molybdenum Disulfide (MoS2) Atomic Layers for Wearable Electronics and Optoelectronics. *ACS Appl. Mater. Interfaces* **2019**, *11* (12), 11061–11105. https://doi.org/10.1021/acsami.8b19859.

(181)   Bao, S.-J.; Li, C. M.; Zang, J.-F.; Cui, X.-Q.; Qiao, Y.; Guo, J. New Nanostructured TiO2 for Direct Electrochemistry and Glucose Sensor Applications. *Adv. Funct. Mater.* **2008**, *18* (4), 591–599. https://doi.org/https://doi.org/10.1002/adfm.200700728.

(182)   Zhang, J.; Li, C. M. Nanoporous Metals: Fabrication Strategies and Advanced Electrochemical Applications in Catalysis, Sensing and Energy Systems. *Chem. Soc. Rev.* **2012**, *41* (21), 7016–7031. https://doi.org/10.1039/C2CS35210A.

(183)   Maroneze, C. M.; dos Santos, G. P.; de Moraes, V. B.; da Costa, L. P.; Kubota, L. T. Multifunctional Catalytic Platform for Peroxidase Mimicking, Enzyme Immobilization and Biosensing. *Biosens. Bioelectron.* **2016**, *77*, 746–751. https://doi.org/https://doi.org/10.1016/j.bios.2015.10.042.

(184)   Wang, L.; Jackman, J. A.; Ng, W. B.; Cho, N.-J. Flexible, Graphene-Coated Biocomposite for Highly Sensitive, Real-Time Molecular Detection. *Adv. Funct. Mater.* **2016**, *26* (47), 8623–8630. https://doi.org/https://doi.org/10.1002/adfm.201603550.

(185)   Ali, H.; Khan, E.; Ilahi, I. Environmental Chemistry and Ecotoxicology of Hazardous Heavy Metals: Environmental Persistence, Toxicity, and Bioaccumulation. *J. Chem.* **2019**, *2019*, 6730305. https://doi.org/10.1155/2019/6730305.

(186)   Gwenzi, W.; Mupatsi, N. M.; Mtisi, M.; Mungazi, A. A. Sources and Health Risks of Rare Earth Elements in Waters. In *Water Pollution and Remediation: Heavy Metals*; Inamuddin, Ahamed, M. I., Lichtfouse, E., Eds.; Springer. https://doi.org/https://doi.org/10.1007/978-3-030-52421-0.

(187)   Sanz-Ramos, M.; Bladé, E.; Dolz, J.; Sánchez-Juny, M. Revisiting the Hydraulics of the Aznalcóllar Mine Disaster. *Mine Water Environ.* **2022**, *41* (2), 335–356. https://doi.org/10.1007/s10230-022-00863-w.

(188)   Masindi, V. Environmental Contamination by Heavy Metals; Aglan, K. L. M. E.-H. E.-D. M. S. E.-R. F., Ed.; IntechOpen: Rijeka, 2018; p Ch. 7. https://doi.org/10.5772/intechopen.76082.

(189)   Kutralam-Muniasamy, G.; Pérez-Guevara, F.; Martínez, I. E.; Shruti, V. C. Overview of Microplastics Pollution with Heavy Metals: Analytical Methods, Occurrence, Transfer Risks and Call for Standardization. *J. Hazard. Mater.* **2021**, *415*, 125–755. https://doi.org/https://doi.org/10.1016/j.jhazmat.2021.125755.

(190)   Vats, P.; Kaur, U. J.; Rishi, P. Heavy Metal-Induced Selection and Proliferation of Antibiotic Resistance: A Review. *J. Appl. Microbiol.* **2022**, *132* (6), 4058–4076. https://doi.org/https://doi.org/10.1111/jam.15492.

(191)   Jomova, K.; Valko, M. Advances in Metal-Induced Oxidative Stress and Human Disease. *Toxicology* **2011**, *283* (2), 65–87. https://doi.org/https://doi.org/10.1016/j.tox.2011.03.001.

(192)   Wan, H.; Sun, Q.; Li, H.; Sun, F.; Hu, N.; Wang, P. Screen-Printed Gold Electrode with Gold Nanoparticles Modification for Simultaneous Electrochemical Determination of Lead and Copper. *Sensors Actuators B Chem.* **2015**, *209*, 336–342. https://doi.org/https://doi.org/10.1016/j.snb.2014.11.127.

(193)   Jan, A. T.; Azam, M.; Siddiqui, K.; Ali, A.; Choi, I.; Haq, Q. M. R. Heavy Metals and Human Health: Mechanistic Insight into Toxicity and Counter Defense System of Antioxidants. *Int. J. Mol. Sci.* **2015**, *16* (12), 29592–29630. https://doi.org/10.3390/ijms161226183.

(194)   Aragay, G.; Pons, J.; Merkoçi, A. Recent Trends in Macro-, Micro-, and Nanomaterial-Based Tools and Strategies for Heavy-Metal Detection. *Chem. Rev.* **2011**, *111* (5), 3433–3458. https://doi.org/10.1021/cr100383r.

(195)   World Health Organization. Guidelines for drinking-water quality, 4th ed., incorporating the 1st addendum (chapters) https://www.who.int/publications/i/item/9789241549950.

(196)   United States Evironmental Protection Agency. National Primary Drinking Water Regulations https://www.epa.gov/ground-water-and-drinking-water/national-primary-drinking-water-regulations#Inorganic.

(197)   Yu, L.; Liou, I. W.; Biggins, S. W.; Yeh, M.; Jalikis, F.; Chan, L.-N.; Burkhead, J. Copper Deficiency in Liver Diseases: A Case Series and Pathophysiological Considerations. *Hepatol. Commun.* **2019**, *3* (8), 1159–1165. https://doi.org/https://doi.org/10.1002/hep4.1393.

(198)   Youssef, A. A.; Wood, B.; Baron, D. N. Serum Copper: A Marker of Disease Activity in Rheumatoid Arthritis. *J. Clin. Pathol.* **1983**, *36* (1), 14–17. https://doi.org/10.1136/jcp.36.1.14.

(199)   Schaefer, M.; Schellenberg, M.; Merle, U.; Weiss, K. H.; Stremmel, W. Wilson Protein Expression, Copper Excretion and Sweat Production in Sweat Glands of Wilson Disease Patients and Controls. *BMC Gastroenterol.* **2008**, *8* (1), 29. https://doi.org/10.1186/1471-230X-8-29.

(200)   Sunderman, F. W. J.; Hohnadel, D. C.; Evenson, M. A.; Wannamaker, B. B.; Dahl, D. S. Excretion of Copper in Sweat of Patients with Wilson's Disease during Sauna   Bathing. *Ann. Clin. Lab. Sci.* **1974**, *4* (5), 407–412.

(201)   Agarwal, A.; Avarebeel, S.; Choudhary, N. S.; Goudar, M.; Tejaswini, C. . Correlation of Trace Elements in Patients of Chronic Liver Disease with Respect to Child- Turcotte- Pugh Scoring System. *J. Clin. Diagnostic Res.* **2017**, *11* (9), OC25 LP-OC28. https://doi.org/10.7860/JCDR/2017/26519/10655.

(202)   Vierling, J. M. Copper Metabolism in Primary Biliary Cirrhosis. *Semin Liver Dis* **1981**, *1* (04), 293–308.

(203)   Nangliya, V.; Sharma, A.; Yadav, D.; Sunder, S.; Nijhawan, S.; Mishra, S. Study of Trace Elements in Liver Cirrhosis Patients and Their Role in Prognosis of Disease. *Biol. Trace Elem. Res.* **2015**, *165* (1), 35–40. https://doi.org/10.1007/s12011-015-0237-3.

(204)   Siquier-Coll, J.; Bartolomé, I.; Perez-Quintero, M.; Grijota, F. J.; Muñoz, D.; Maynar-Mariño, M. Effects of Exposure to High Temperatures on Serum, Urine and Sweat Concentrations of Iron and Copper. *J. Therm. Biol.* **2020**, *89*, 102536. https://doi.org/https://doi.org/10.1016/j.jtherbio.2020.102536.

(205)   Borrill, A. J.; Reily, N. E.; Macpherson, J. V. Addressing the Practicalities of Anodic Stripping Voltammetry for Heavy Metal Detection: A Tutorial Review. *Analyst* **2019**, *144* (23), 6834–6849. https://doi.org/10.1039/C9AN01437C.

(206)   Zheng, J.; Rahim, M. A.; Tang, J.; Allioux, F.-M.; Kalantar-Zadeh, K. Post-Transition Metal Electrodes for Sensing Heavy Metal Ions by Stripping Voltammetry. *Adv. Mater. Technol.* **2022**, *7* (1), 2100760. https://doi.org/https://doi.org/10.1002/admt.202100760.

(207)   Holmes, J.; Pathirathna, P.; Hashemi, P. Novel Frontiers in Voltammetric Trace Metal Analysis: Towards Real Time, on-Site, in Situ Measurements. *TrAC Trends Anal. Chem.* **2019**, *111*, 206–219. https://doi.org/https://doi.org/10.1016/j.trac.2018.11.003.

(208)   Zuo, Y.; Xu, J.; Zhu, X.; Duan, X.; Lu, L.; Yu, Y. Graphene-Derived Nanomaterials as Recognition Elements for Electrochemical Determination of Heavy Metal Ions: A Review. *Microchim. Acta* **2019**, *186* (3), 171. https://doi.org/10.1007/s00604-019-3248-5.

(209)   Lau, O.-W.; Cheng, O.-M. Determination of Zinc in Environmental Samples by Anodic Stripping Voltammetry. *Anal. Chim. Acta* **1998**, *376* (2), 197–207. https://doi.org/https://doi.org/10.1016/S0003-2670(98)00531-5.

(210)   Fernández, E.; Vidal, L.; Costa-García, A.; Canals, A. Mercury Determination in Urine Samples by Gold Nanostructured Screen-Printed Carbon Electrodes after Vortex-Assisted Ionic Liquid Dispersive

Liquid–Liquid Microextraction. *Anal. Chim. Acta* **2016**, *915*, 49–55. https://doi.org/https://doi.org/10.1016/j.aca.2016.02.028.

(211)   Wikipedia. Standard electrode potential (data page).

(212)   Lu, Y.; Liang, X.; Niyungeko, C.; Zhou, J.; Xu, J.; Tian, G. A Review of the Identification and Detection of Heavy Metal Ions in the Environment by Voltammetry. *Talanta* **2018**, *178*, 324–338. https://doi.org/https://doi.org/10.1016/j.talanta.2017.08.033.

(213)   Economou, A. Screen-Printed Electrodes Modified with "Green" Metals for Electrochemical Stripping Analysis of Toxic Elements. *Sensors* **2018**, *18* (4). https://doi.org/10.3390/s18041032.

(214)   Gao, W.; Nyein, H. Y. Y.; Shahpar, Z.; Fahad, H. M.; Chen, K.; Emaminejad, S.; Gao, Y.; Tai, L.-C.; Ota, H.; Wu, E.; Bullock, J.; Zeng, Y.; Lien, D.-H.; Javey, A. Wearable Microsensor Array for Multiplexed Heavy Metal Monitoring of Body Fluids. *ACS Sensors* **2016**, *1* (7), 866–874. https://doi.org/10.1021/acssensors.6b00287.

(215)   Kudr, J.; Zitka, O.; Klimanek, M.; Vrba, R.; Adam, V. Microfluidic Electrochemical Devices for Pollution Analysis–A Review. *Sensors Actuators B Chem.* **2017**, *246*, 578–590. https://doi.org/https://doi.org/10.1016/j.snb.2017.02.052.

(216)   Economou, A.; Voulgaropoulos, A. On-Line Stripping Voltammetry of Trace Metals at a Flow-through Bismuth-Film Electrode by Means of a Hybrid Flow-Injection/Sequential-Injection System. *Talanta* **2007**, *71* (2), 758–765. https://doi.org/https://doi.org/10.1016/j.talanta.2006.05.021.

(217)   Kefala, G.; Economou, A. Polymer-Coated Bismuth Film Electrodes for the Determination of Trace Metals by Sequential-Injection Analysis/Anodic Stripping Voltammetry. *Anal. Chim. Acta* **2006**, *576* (2), 283–289. https://doi.org/https://doi.org/10.1016/j.aca.2006.06.006.

(218)   Gholizadeh, A.; Sardar, S.; Francisco, K.; Maher, A.; Miskewitz, R.; Javanmard, M. Towards *In-Situ* Environmental Monitoring: On-Chip Sample Preparation and Detection of Lead in Sediment Samples Using Graphene Oxide Sensor. *IEEE Sens. J.* **2020**, *20* (22), 13787–13795. https://doi.org/10.1109/JSEN.2020.3006021.

(219)   Cai, W.; Li, Y.; Gao, X.; Guo, H.; Zhao, H.; Wang, P. An Automated Electronic Tongue for In-Situ Quick Monitoring of Trace Heavy Metals in Water Environment. *AIP Conf. Proc.* **2009**, *1137* (1), 493–496. https://doi.org/10.1063/1.3156593.

(220)   Zou, Z.; Jang, A.; MacKnight, E.; Wu, P.-M.; Do, J.; Bishop, P. L.; Ahn, C. H. Environmentally Friendly Disposable Sensors with Microfabricated On-Chip Planar Bismuth Electrode for in Situ Heavy Metal Ions Measurement. *Sensors Actuators B Chem.* **2008**, *134* (1), 18–24. https://doi.org/https://doi.org/10.1016/j.snb.2008.04.005.

(221)   Chen, C.; Zhang, J.; Du, Y.; Yang, X.; Wang, E. Microfabricated On-Chip Integrated Au–Ag–Au Three-Electrode System for in Situ Mercury Ion Determination. *Analyst* **2010**, *135* (5), 1010–1014. https://doi.org/10.1039/B924545F.

(222)   Tercier-Waeber, M.-L.; Abdou, M.; Fighera, M.; Kowal, J.; Bakker, E.; van der Wal, P. In Situ Voltammetric Sensor of Potentially Bioavailable Inorganic Mercury in Marine Aquatic Systems Based on Gel-Integrated Nanostructured Gold-Based Microelectrode Arrays. *ACS Sensors* **2021**, *6* (3), 925–937. https://doi.org/10.1021/acssensors.0c02111.

(223)   Henríquez, C.; Laglera, L. M.; Alpizar, M. J.; Calvo, J.; Arduini, F.; Cerdà, V. Cadmium Determination in Natural Water Samples with an Automatic Multisyringe Flow Injection System Coupled

to a Flow-through Screen Printed Electrode. *Talanta* **2012**, *96*, 140–146. https://doi.org/https://doi.org/10.1016/j.talanta.2012.01.032.

(224)   Tormin, T. F.; Cunha, R. R.; da Silva, R. A. B.; Munoz, R. A. A.; Richter, E. M. Combination of Screen-Printed Electrodes and Batch Injection Analysis: A Simple, Robust, High-Throughput, and Portable Electrochemical System. *Sensors Actuators B Chem.* **2014**, *202*, 93–98. https://doi.org/https://doi.org/10.1016/j.snb.2014.04.096.

(225)   Shen, L.-L.; Zhang, G.-R.; Li, W.; Biesalski, M.; Etzold, B. J. M. Modifier-Free Microfluidic Electrochemical Sensor for Heavy-Metal Detection. *ACS Omega* **2017**, *2* (8), 4593–4603. https://doi.org/10.1021/acsomega.7b00611.

(226)   Medina-Sánchez, M.; Cadevall, M.; Ros, J.; Merkoçi, A. Eco-Friendly Electrochemical Lab-on-Paper for Heavy Metal Detection. *Anal. Bioanal. Chem.* **2015**, *407* (28), 8445–8449. https://doi.org/10.1007/s00216-015-9022-6.

(227)   Chałupniak, A.; Merkoçi, A. Graphene Oxide–Poly(Dimethylsiloxane)-Based Lab-on-a-Chip Platform for Heavy-Metals Preconcentration and Electrochemical Detection. *ACS Appl. Mater. Interfaces* **2017**, *9* (51), 44766–44775. https://doi.org/10.1021/acsami.7b12368.

(228)   Wang, N.; Kanhere, E.; Kottapalli, A. G. P.; Miao, J.; Triantafyllou, M. S. Flexible Liquid Crystal Polymer-Based Electrochemical Sensor for *in-Situ* Detection of Zinc(II) in Seawater. *Microchim. Acta* **2017**, *184* (8), 3007–3015. https://doi.org/10.1007/s00604-017-2280-6.

(229)   Lv, Z.-L.; Qi, G.-M.; Jiang, T.-J.; Guo, Z.; Yu, D.-Y.; Liu, J.-H.; Huang, X.-J. A Simplified Electrochemical Instrument Equipped with Automated Flow-Injection System and Network Communication Technology for Remote Online Monitoring of Heavy Metal Ions. *J. Electroanal. Chem.* **2017**, *791*, 49–55. https://doi.org/https://doi.org/10.1016/j.jelechem.2017.03.012.

(230)   Barros Azeredo, N. F.; Ferreira Santos, M. S.; Sempionatto, J. R.; Wang, J.; Angnes, L. Screen-Printed Technologies Combined with Flow Analysis Techniques: Moving from Benchtop to Everywhere. *Anal. Chem.* **2022**, *94* (1), 250–268. https://doi.org/10.1021/acs.analchem.1c02637.

(231)   Park, J. Y.; Hui, X.; Sharifuzzaman, M.; Sharma, S.; Xuan, X.; Zhang, S.; Ko, S. G.; Yoon, S. H. High-Performance Flexible Electrochemical Heavy Metal Sensor Based on Layer-by-Layer Assembly of Ti3C2Tx/MWNTs Nanocomposites for Noninvasive Detection of Copper and Zinc Ions in Human Biofluids. *ACS Appl. Mater. Interfaces* **2020**, *12* (43), 48928–48937. https://doi.org/10.1021/acsami.0c12239.

(232)   Faheem, A.; Cinti, S. Non-Invasive Electrochemistry-Driven Metals Tracing in Human Biofluids. *Biosens. Bioelectron.* **2022**, *200*, 113904. https://doi.org/https://doi.org/10.1016/j.bios.2021.113904.

(233)   Bariya, M.; Li, L.; Ghattamaneni, R.; Ahn, C. H.; Nyein, H. Y. Y.; Tai, L. C.; Javey, A. Glove-Based Sensors for Multimodal Monitoring of Natural Sweat. *Sci. Adv.* **2020**, *6* (35), 1–10. https://doi.org/10.1126/sciadv.abb8308.

(234)   Ghaffari, R.; Rogers, J. A.; Ray, T. R. Recent Progress, Challenges, and Opportunities for Wearable Biochemical Sensors for Sweat Analysis. *Sensors Actuators B Chem.* **2021**, *332*, 129447. https://doi.org/https://doi.org/10.1016/j.snb.2021.129447.

(235)   Mohan, A. M. V.; Rajendran, V.; Mishra, R. K.; Jayaraman, M. Recent Advances and Perspectives in Sweat Based Wearable Electrochemical Sensors. *TrAC Trends Anal. Chem.* **2020**, *131*, 116024. https://doi.org/https://doi.org/10.1016/j.trac.2020.116024.

(236)   Brothers, M. C.; DeBrosse, M.; Grigsby, C. C.; Naik, R. R.; Hussain, S. M.; Heikenfeld, J.; Kim, S. S. Achievements and Challenges for Real-Time Sensing of Analytes in Sweat within Wearable Platforms. *Acc. Chem. Res.* **2019**, *52* (2), 297–306. https://doi.org/10.1021/acs.accounts.8b00555.

(237)   Jo, S.; Sung, D.; Kim, S.; Koo, J. A Review of Wearable Biosensors for Sweat Analysis. *Biomed. Eng. Lett.* **2021**, *11* (2), 117–129. https://doi.org/10.1007/s13534-021-00191-y.

(238)   Qiao, L.; Benzigar, M. R.; Subramony, J. A.; Lovell, N. H.; Liu, G. Advances in Sweat Wearables: Sample Extraction, Real-Time Biosensing, and Flexible Platforms. *ACS Appl. Mater. Interfaces* **2020**, *12* (30), 34337–34361. https://doi.org/10.1021/acsami.0c07614.

(239)   Xu, J.; Fang, Y.; Chen, J. Wearable Biosensors for Non-Invasive Sweat Diagnostics. *Biosensors* . 2021. https://doi.org/10.3390/bios11080245.

(240)   Kim, J.; Campbell, A. S.; de Ávila, B. E.-F.; Wang, J. Wearable Biosensors for Healthcare Monitoring. *Nat. Biotechnol.* **2019**, *37* (4), 389–406. https://doi.org/10.1038/s41587-019-0045-y.

(241)   Bagheri, N.; Mazzaracchio, V.; Cinti, S.; Colozza, N.; Di Natale, C.; Netti, P. A.; Saraji, M.; Roggero, S.; Moscone, D.; Arduini, F. Electroanalytical Sensor Based on Gold-Nanoparticle-Decorated Paper for Sensitive Detection of Copper Ions in Sweat and Serum. *Anal. Chem.* **2021**, *93* (12), 5225–5233. https://doi.org/10.1021/acs.analchem.0c05469.

(242)   Nyein, H. Y. Y.; Bariya, M.; Kivimäki, L.; Uusitalo, S.; Liaw, T. S.; Jansson, E.; Ahn, C. H.; Hangasky, J. A.; Zhao, J.; Lin, Y.; Happonen, T.; Chao, M.; Liedert, C.; Zhao, Y.; Tai, L.-C.; Hiltunen, J.; Javey, A. Regional and Correlative Sweat Analysis Using High-Throughput Microfluidic Sensing Patches toward Decoding Sweat. *Sci. Adv.* **2019**, *5* (8), eaaw9906. https://doi.org/10.1126/sciadv.aaw9906.

(243)   Zhao, G.; Tong, X.; Hu, Z.; Xiao, X.; Li, D. Electrochemical Costripping Models and Mutual Interferences of Mutli-Transition Metal Systems on the Surface of Boron-Doped Diamond. *Electrochim. Acta* **2008**, *53* (12), 4283–4292. https://doi.org/10.1016/j.electacta.2008.01.017.

(244)   Wang, J. Stripping Analysis at Bismuth Electrodes: A Review. *Electroanalysis* **2005**, *17* (15–16), 1341–1346. https://doi.org/https://doi.org/10.1002/elan.200403270.

(245)   Wang, J.; Lu, J.; Hocevar, S. B.; Farias, P. A. M.; Ogorevc, B. Bismuth-Coated Carbon Electrodes for Anodic Stripping Voltammetry. *Anal. Chem.* **2000**, *72* (14), 3218–3222. https://doi.org/10.1021/ac000108x.

(246)   Zhai, Z.; Huang, N.; Zhuang, H.; Liu, L.; Yang, B.; Wang, C.; Gai, Z.; Guo, F.; Li, Z.; Jiang, X. A Diamond/Graphite Nanoplatelets Electrode for Anodic Stripping Voltammetric Trace Determination of Zn(II), Cd(II), Pb(II) and Cu(II). *Appl. Surf. Sci.* **2018**, *457* (June), 1192–1201. https://doi.org/10.1016/j.apsusc.2018.06.266.

(247)   Toghill, K. E.; Compton, R. G. Metal Nanoparticle Modified Boron Doped Diamond Electrodes for Use in Electroanalysis. *Electroanalysis* **2010**, *22* (17–18), 1947–1956. https://doi.org/10.1002/elan.201000072.

(248)   Toghill, K. E.; Xiao, L.; Wildgoose, G. G.; Compton, R. G. Electroanalytical Determination of Cadmium(II) and Lead(II) Using an Antimony Nanoparticle Modified Boron-Doped Diamond Electrode. *Electroanalysis* **2009**, *21* (10), 1113–1118. https://doi.org/10.1002/elan.200904547.

(249)   Mališić, M.; Janošević, A.; Šljukić Paunković, B.; Stojković, I.; Ćirić-Marjanović, G. Exploration of MnO2/Carbon Composites and Their Application to Simultaneous Electroanalytical Determination of Pb(II) and Cd(II). *Electrochim. Acta* **2012**, *74*, 158–164. https://doi.org/https://doi.org/10.1016/j.electacta.2012.04.049.

(250)   Gutiérrez, J. M.; Moreno-Barón, L.; Céspedes, F.; Muñoz, R.; del Valle, M. Resolution of Heavy Metal Mixtures from Highly Overlapped ASV Voltammograms Employing a Wavelet Neural Network. *Electroanalysis* **2009**, *21* (3–5), 445–451. https://doi.org/https://doi.org/10.1002/elan.200804419.

(251)   Ramos, A. F.; Palomares, A. M.; Diaz, O. A.; Díaz, M. A. Simultaneous Quantification of Pb (II), Cd (II), Hg (II), As (II) and Cr (III) in Water Using Deep Learning and Voltammetric Electronic Tongue. *SSRN* **2022**.

(252)   Liu, N.; Ye, W.; Liu, G.; Zhao, G. Improving the Accuracy of Stripping Voltammetry Detection of Cd2+ and Pb2+ in the Presence of Cu2+ and Zn2+ by Machine Learning: Understanding and Inhibiting the Interactive Interference among Multiple Heavy Metals. *Anal. Chim. Acta* **2022**, *1213*, 339956. https://doi.org/https://doi.org/10.1016/j.aca.2022.339956.

(253)   Zhao, G.; Liu, G. Interference Effects of Cu({II}) and Pb({II}) on the Stripping Voltammetric Detection of Cd({II}): Improvement in the Detection Precision and Interference Correction. *J. Electrochem. Soc.* **2018**, *165* (9), H488--H495. https://doi.org/10.1149/2.0701809jes.

(254)   Švancara, I.; Pravda, M.; Hvizdalová, M.; Vytřas, K.; Kalcher, K. Voltammetric Investigations on Carbon Paste Electrodes as Supports for Mercury Films. *Electroanalysis* **1994**, *6* (8), 663–671. https://doi.org/https://doi.org/10.1002/elan.1140060809.

(255)   Florence, T. M. Anodic Stripping Voltammetry with a Glassy Carbon Electrode Mercury-Plated in Situ. *J. Electroanal. Chem. Interfacial Electrochem.* **1970**, *27* (2), 273–281. https://doi.org/https://doi.org/10.1016/S0022-0728(70)80189-9.

(256)   de Oliveira, M. F.; Saczk, A. A.; Okumura, L. L.; Fernandes, A. P.; de Moraes, M.; Stradiotto, N. R. Simultaneous Determination of Zinc, Copper, Lead, and Cadmium in Fuel Ethanol by Anodic Stripping Voltammetry Using a Glassy Carbon–Mercury-Film Electrode. *Anal. Bioanal. Chem.* **2004**, *380* (1), 135–140. https://doi.org/10.1007/s00216-004-2733-8.

(257)   Fernández, L. L.; Bastos-Arrieta, J.; Palet, C.; Baeza, M. Composite Electrodes Based on Carbon Materials Decorated with Hg Nanoparticles for the Simultaneous Detection of Cd(II), Pb(II) and Cu(II). *Chemosensors* **2022**, *10* (4). https://doi.org/10.3390/chemosensors10040148.

(258)   Aragay, G.; Puig-Font, A.; Cadevall, M.; Merkoçi, A. Surface Characterizations of Mercury-Based Electrodes with the Resulting Micro and Nano Amalgam Wires and Spheres Formations May Reveal Both Gained Sensitivity and Faced Nonstability in Heavy Metal Detection. *J. Phys. Chem. C* **2010**, *114* (19), 9049–9055. https://doi.org/10.1021/jp102123w.

(259)   Zhang, D.; Xiang, Q. Nafion-Assisted Electrophoretic Deposition and Its Application in Bismuth Film Electrodes for Metal Ion Detection. *Ind. Eng. Chem. Res.* **2021**, *60* (30), 11056–11062. https://doi.org/10.1021/acs.iecr.0c04616.

(260)   Serrano, N.; Alberich, A.; Díaz-Cruz, J. M.; Ariño, C.; Esteban, M. Coating Methods, Modifiers and Applications of Bismuth Screen-Printed Electrodes. *TrAC Trends Anal. Chem.* **2013**, *46*, 15–29. https://doi.org/https://doi.org/10.1016/j.trac.2013.01.012.

(261)   Hočevar, S. B.; Švancara, I.; Vytřas, K.; Ogorevc, B. Novel Electrode for Electrochemical Stripping Analysis Based on Carbon Paste Modified with Bismuth Powder. *Electrochim. Acta* **2005**, *51* (4), 706–710. https://doi.org/https://doi.org/10.1016/j.electacta.2005.05.023.

(262)   Ouyang, R.; Xu, L.; Wen, H.; Cao, P.; Jia, P.; Lei, T.; Zhou, X.; Tie, M.; Fu, X.; Zhao, Y.; Chang, H.; Miao, Y. A Novel Indium Doped Bismuth Nanofilm for Simultaneous Stripping Determination of Zn(II), Cd(II) and Pb(II) in River Water. *Int. J. Electrochem. Sci.* **2018**, *13*, 1423 – 1440. https://doi.org/10.20964/2018.02.02.

(263)   Li, Y.; Sun, G.; Zhang, Y.; Ge, C.; Bao, N.; Wang, Y. A Glassy Carbon Electrode Modified with Bismuth Nanotubes in a Silsesquioxane Framework for Sensing of Trace Lead and Cadmium by Stripping Voltammetry. *Microchim. Acta* **2014**, *181* (7), 751–757. https://doi.org/10.1007/s00604-013-1082-8.

(264)   Lee, K. Y.; Ambrosi, A.; Pumera, M. 3D-Printed Metal Electrodes for Heavy Metals Detection by Anodic Stripping Voltammetry. *Electroanalysis* **2017**, *29* (11), 2444–2453. https://doi.org/https://doi.org/10.1002/elan.201700388.

(265)   Wang, W.; Bao, N.; Yuan, W.; Si, N.; Bai, H.; Li, H.; Zhang, Q. Simultaneous Determination of Lead, Arsenic, and Mercury in Cosmetics Using a Plastic Based Disposable Electrochemical Sensor. *Microchem. J.* **2019**, *148*, 240–247. https://doi.org/https://doi.org/10.1016/j.microc.2019.05.011.

(266)   Simm, A. O.; Banks, C. E.; Compton, R. G. Sonically Assisted Electroanalytical Detection of Ultratrace Arsenic. *Anal. Chem.* **2004**, *76* (17), 5051–5055. https://doi.org/10.1021/ac049331a.

(267)   Sullivan, C.; Lu, D.; Brack, E.; Drew, C.; Kurup, P. Voltammetric Codetection of Arsenic(III) and Copper(II) in Alkaline Buffering System with Gold Nanostar Modified Electrodes. *Anal. Chim. Acta* **2020**, *1107*, 63–73. https://doi.org/https://doi.org/10.1016/j.aca.2020.02.015.

(268)   Hassan, S. S.; Sirajuddin; Solangi, A. R.; Kazi, T. G.; Kalhoro, M. S.; Junejo, Y.; Tagar, Z. A.; Kalwar, N. H. Nafion Stabilized Ibuprofen–Gold Nanostructures Modified Screen Printed Electrode as Arsenic(III) Sensor. *J. Electroanal. Chem.* **2012**, *682*, 77–82. https://doi.org/https://doi.org/10.1016/j.jelechem.2012.07.006.

(269)   Hocevar, S. B.; Švancara, I.; Ogorevc, B.; Vytřas, K. Antimony Film Electrode for Electrochemical Stripping Analysis. *Anal. Chem.* **2007**, *79* (22), 8639–8643. https://doi.org/10.1021/ac070478m.

(270)   Tesarova, E.; Baldrianova, L.; Hocevar, S. B.; Svancara, I.; Vytras, K.; Ogorevc, B. Anodic Stripping Voltammetric Measurement of Trace Heavy Metals at Antimony Film Carbon Paste Electrode. *Electrochim. Acta* **2009**, *54* (5), 1506–1510. https://doi.org/https://doi.org/10.1016/j.electacta.2008.09.030.

(271)   Dal Borgo, S.; Jovanovski, V.; Hocevar, S. B. Antimony Film Electrode for Stripping Voltammetric Measurement of Hg(II) in the Presence of Cu(II). *Electrochim. Acta* **2013**, *88*, 713–717. https://doi.org/https://doi.org/10.1016/j.electacta.2012.10.122.

(272)   Ashrafi, A. M.; Cerovac, S.; Mudrić, S.; Guzsvány, V.; Husáková, L.; Urbanová, I.; Vytřas, K. Antimony Nanoparticle-Multiwalled Carbon Nanotubes Composite Immobilized at Carbon Paste Electrode for Determination of Trace Heavy Metals. *Sensors Actuators B Chem.* **2014**, *191*, 320–325. https://doi.org/https://doi.org/10.1016/j.snb.2013.08.087.

(273)   Liu, X.; Yao, Y.; Ying, Y.; Ping, J. Recent Advances in Nanomaterial-Enabled Screen-Printed Electrochemical Sensors for Heavy Metal Detection. *TrAC - Trends Anal. Chem.* **2019**, *115*, 187–202. https://doi.org/10.1016/j.trac.2019.03.021.

(274)   Tan, Z.; Wu, W.; Feng, C.; Wu, H.; Zhang, Z. Simultaneous Determination of Heavy Metals by an Electrochemical Method Based on a Nanocomposite Consisting of Fluorinated Graphene and Gold Nanocage. *Microchim. Acta* **2020**, *187* (7), 414. https://doi.org/10.1007/s00604-020-04393-6.

(275)   Wang, W.-J.; Lu, X.-Y.; Kong, F.-Y.; Li, H.-Y.; Wang, Z.-X.; Wang, W. A Reduced Graphene Oxide Supported Au-Bi Bimetallic Nanoparticles as an Enhanced Sensing Platform for Simultaneous Voltammetric Determination of Pb (II) and Cd (II). *Microchem. J.* **2022**, *175*, 107078. https://doi.org/https://doi.org/10.1016/j.microc.2021.107078.

(276)   Vicentini, F. C.; Silva, T. A.; Pellatieri, A.; Janegitz, B. C.; Fatibello-Filho, O.; Faria, R. C. Pb(II) Determination in Natural Water Using a Carbon Nanotubes Paste Electrode Modified with Crosslinked Chitosan. *Microchem. J.* **2014**, *116*, 191–196. https://doi.org/10.1016/j.microc.2014.05.008.

(277)   Promphet, N.; Rattanarat, P.; Rangkupan, R.; Chailapakul, O.; Rodthongkum, N. An Electrochemical Sensor Based on Graphene/Polyaniline/Polystyrene Nanoporous Fibers Modified Electrode for Simultaneous Determination of Lead and Cadmium. *Sensors Actuators, B Chem.* **2015**, *207* (PartA), 526–534. https://doi.org/10.1016/j.snb.2014.10.126.

(278)   Getachew, B. A.; Bergsman, D. S.; Grossman, J. C. Laser-Induced Graphene from Polyimide and Polyethersulfone Precursors as a Sensing Electrode in Anodic Stripping Voltammetry. *ACS Appl. Mater. Interfaces* **2020**, *12* (43), 48511–48517. https://doi.org/10.1021/acsami.0c11725.

(279)   Hu, J.; Li, Z.; Zhai, C.; Zeng, L.; Zhu, M. Photo-Assisted Simultaneous Electrochemical Detection of Multiple Heavy Metal Ions with a Metal-Free Carbon Black Anchored Graphitic Carbon Nitride Sensor. *Anal. Chim. Acta* **2021**, *1183*, 338951. https://doi.org/https://doi.org/10.1016/j.aca.2021.338951.

(280)   Manna, B.; Raj, C. R. Nanostructured Sulfur-Doped Porous Reduced Graphene Oxide for the Ultrasensitive Electrochemical Detection and Efficient Removal of Hg(II). *ACS Sustain. Chem. Eng.* **2018**, *6* (5), 6175–6182. https://doi.org/10.1021/acssuschemeng.7b04884.

(281)   Wei, Y.; Yang, R.; Chen, X.; Wang, L.; Liu, J. H.; Huang, X. J. A Cation Trap for Anodic Stripping Voltammetry: NH3-Plasma Treated Carbon Nanotubes for Adsorption and Detection of Metal Ions. *Anal. Chim. Acta* **2012**, *755*, 54–61. https://doi.org/10.1016/j.aca.2012.10.021.

(282)   Seenivasan, R.; Chang, W. J.; Gunasekaran, S. Highly Sensitive Detection and Removal of Lead Ions in Water Using Cysteine-Functionalized Graphene Oxide/Polypyrrole Nanocomposite Film Electrode. *ACS Appl. Mater. Interfaces* **2015**, *7* (29), 15935–15943. https://doi.org/10.1021/acsami.5b03904.

(283)   Huangfu, C.; Fu, L.; Li, Y.; Li, X.; Du, H.; Ye, J. Sensitive Stripping Determination of Cadmium(Ii) and Lead(Ii) on Disposable Graphene Modified Screen-Printed Electrode. *Electroanalysis* **2013**, *25* (9), 2238–2243. https://doi.org/10.1002/elan.201300239.

(284)   Yi, W.; He, Z.; Fei, J.; He, X. Sensitive Electrochemical Sensor Based on Poly(l-Glutamic Acid)/Graphene Oxide Composite Material for Simultaneous Detection of Heavy Metal Ions. *RSC Adv.* **2019**, *9* (30), 17325–17334. https://doi.org/10.1039/C9RA01891C.

(285)   Abdulla, M.; Ali, A.; Jamal, R.; Bakri, T.; Wu, W.; Abdiryim, T. Electrochemical Sensor of Double-Thiol Linked PProDOT@Si Composite for Simultaneous Detection of Cd(II), Pb(II), and Hg(II). *Polymers (Basel).* **2019**, *11* (5), 1–19. https://doi.org/10.3390/polym11050815.

(286)   Zuo, X.; Xia, Y.; Ji, Q.; Gao, X.; Yin, S.; Wang, M.; Wang, X.; Qiu, B.; Wei, A.; Sun, Z.; Liu, Z.; Zhu, J.; Cheng, Y.-J. Self-Templating Construction of 3D Hierarchical Macro-/Mesoporous Silicon from 0D Silica Nanoparticles. *ACS Nano* **2017**, *11* (1), 889–899. https://doi.org/10.1021/acsnano.6b07450.

(287)   Naguib, M.; Kurtoglu, M.; Presser, V.; Lu, J.; Niu, J.; Heon, M.; Hultman, L.; Gogotsi, Y.; Barsoum, M. W. Two-Dimensional Nanocrystals Produced by Exfoliation of Ti3AlC2. *Adv. Mater.* **2011**, *23* (37), 4248–4253. https://doi.org/https://doi.org/10.1002/adma.201102306.

(288)   Lukatskaya, M. R.; Mashtalir, O.; Ren, C. E.; Dall'Agnese, Y.; Rozier, P.; Taberna, P. L.; Naguib, M.; Simon, P.; Barsoum, M. W.; Gogotsi, Y. Cation Intercalation and High Volumetric Capacitance of Two-Dimensional Titanium Carbide. *Science (80-.).* **2013**, *341* (6153), 1502–1505. https://doi.org/10.1126/science.1241488.

(289)	Zhu, X.; Liu, B.; Hou, H.; Huang, Z.; Zeinu, K. M.; Huang, L.; Yuan, X.; Guo, D.; Hu, J.; Yang, J. Alkaline Intercalation of Ti3C2 MXene for Simultaneous Electrochemical Detection of Cd(II), Pb(II), Cu(II) and Hg(II). *Electrochim. Acta* **2017**, *248*, 46–57. https://doi.org/https://doi.org/10.1016/j.electacta.2017.07.084.

(290)	Chen, X.; Liu, Z.-G.; Zhao, Z.-Q.; Liu, J.-H.; Huang, X.-J. SnO2 Tube-in-Tube Nanostructures: Cu@C Nanocable Templated Synthesis and Their Mutual Interferences between Heavy Metal Ions Revealed by Stripping Voltammetry. *Small* **2013**, *9* (13), 2233–2239. https://doi.org/https://doi.org/10.1002/smll.201202673.

(291)	Zhang, Q. X.; Wen, H.; Peng, D.; Fu, Q.; Huang, X. J. Interesting Interference Evidences of Electrochemical Detection of Zn(II), Cd(II) and Pb(II) on Three Different Morphologies of MnO2 Nanocrystals. *J. Electroanal. Chem.* **2015**, *739*, 89–96. https://doi.org/10.1016/j.jelechem.2014.12.023.

(292)	Wei, Y.; Yang, R.; Yu, X.-Y.; Wang, L.; Liu, J.-H.; Huang, X.-J. Stripping Voltammetry Study of Ultra-Trace Toxic Metal Ions on Highly Selectively Adsorptive Porous Magnesium Oxide Nanoflowers. *Analyst* **2012**, *137* (9), 2183–2191. https://doi.org/10.1039/C2AN15939B.

(293)	Yao, X. Z.; Guo, Z.; Yuan, Q. H.; Liu, Z. G.; Liu, J. H.; Huang, X. J. Exploiting Differential Electrochemical Stripping Behaviors of Fe 3O4 Nanocrystals toward Heavy Metal Ions by Crystal Cutting. *ACS Appl. Mater. Interfaces* **2014**, *6* (15), 12203–12213. https://doi.org/10.1021/am501617a.

(294)	Hu, J.; Chen, G.; Lo, I. M. C. Removal and Recovery of Cr(VI) from Wastewater by Maghemite Nanoparticles. *Water Res.* **2005**, *39* (18), 4528–4536. https://doi.org/https://doi.org/10.1016/j.watres.2005.05.051.

(295)	Jing, H.; Guohua, C.; C., L. I. M. Selective Removal of Heavy Metals from Industrial Wastewater Using Maghemite Nanoparticle: Performance and Mechanisms. *J. Environ. Eng.* **2006**, *132* (7), 709–715. https://doi.org/10.1061/(ASCE)0733-9372(2006)132:7(709).

(296)	Li, W.-J.; Yao, X.-Z.; Guo, Z.; Liu, J.-H.; Huang, X.-J. Fe3O4 with Novel Nanoplate-Stacked Structure: Surfactant-Free Hydrothermal Synthesis and Application in Detection of Heavy Metal Ions. *J. Electroanal. Chem.* **2015**, *749*, 75–82. https://doi.org/https://doi.org/10.1016/j.jelechem.2015.04.038.

(297)	Wu, W.; Jia, M.; Wang, Z.; Zhang, W.; Zhang, Q.; Liu, G.; Zhang, Z.; Li, P. Simultaneous Voltammetric Determination of Cadmium(II), Lead(II), Mercury(II), Zinc(II), and Copper(II) Using a Glassy Carbon Electrode Modified with Magnetite (Fe3O4) Nanoparticles and Fluorinated Multiwalled Carbon Nanotubes. *Microchim. Acta* **2019**, *186* (2), 0–9. https://doi.org/10.1007/s00604-018-3216-5.

(298)	Chu, Y.; Gao, F.; Gao, F.; Wang, Q. Enhanced Stripping Voltammetric Response of Hg2+, Cu2+, Pb2+ and Cd2+ by ZIF-8 and Its Electrochemical Analytical Application. *J. Electroanal. Chem.* **2019**, *835*, 293–300. https://doi.org/https://doi.org/10.1016/j.jelechem.2019.01.053.

(299)	Mettakoonpitak, J.; Mehaffy, J.; Volckens, J.; Henry, C. S. AgNP/Bi/Nafion-Modified Disposable Electrodes for Sensitive Zn(II), Cd(II), and Pb(II) Detection in Aerosol Samples. *Electroanalysis* **2017**, *29* (3), 880–889. https://doi.org/10.1002/elan.201600591.

(300)	Li, P.-H.; Li, Y.-X.; Chen, S.-H.; Li, S.-S.; Jiang, M.; Guo, Z.; Liu, J.-H.; Huang, X.-J.; Yang, M. Sensitive and Interference-Free Electrochemical Determination of Pb(II) in Wastewater Using Porous Ce-Zr Oxide Nanospheres. *Sensors Actuators B Chem.* **2018**, *257*, 1009–1020. https://doi.org/https://doi.org/10.1016/j.snb.2017.11.061.

(301)	James, S. L. Metal-Organic Frameworks. *Chem. Soc. Rev.* **2003**, *32* (5), 276–288. https://doi.org/10.1039/B200393G.

(302)   Pan, Y.; Liu, Y.; Zeng, G.; Zhao, L.; Lai, Z. Rapid Synthesis of Zeolitic Imidazolate Framework-8 (ZIF-8) Nanocrystals in an Aqueous System. *Chem. Commun.* **2011**, *47* (7), 2071–2073. https://doi.org/10.1039/C0CC05002D.

(303)   Chen, H.-H.; Huang, J.-F. EDTA Assisted Highly Selective Detection of As3+ on Au Nanoparticle Modified Glassy Carbon Electrodes: Facile in Situ Electrochemical Characterization of Au Nanoparticles. *Anal. Chem.* **2014**, *86* (24), 12406–12413. https://doi.org/10.1021/ac504044w.

(304)   Huang, J.-F.; Chen, H.-H. Gold-Nanoparticle-Embedded Nafion Composite Modified on Glassy Carbon Electrode for Highly Selective Detection of Arsenic(III). *Talanta* **2013**, *116*, 852–859. https://doi.org/https://doi.org/10.1016/j.talanta.2013.07.063.

(305)   Czop, E.; Economou, A.; Bobrowski, A. A Study of in Situ Plated Tin-Film Electrodes for the Determination of Trace Metals by Means of Square-Wave Anodic Stripping Voltammetry. *Electrochim. Acta* **2011**, *56* (5), 2206–2212. https://doi.org/https://doi.org/10.1016/j.electacta.2010.12.017.

(306)   Rattanarat, P.; Dungchai, W.; Cate, D.; Volckens, J.; Chailapakul, O.; Henry, C. S. Multilayer Paper-Based Device for Colorimetric and Electrochemical Quantification of Metals. *Anal. Chem.* **2014**, *86* (7), 3555–3562. https://doi.org/10.1021/ac5000224.

(307)   Lu, L.; Zhou, L.; Chen, J.; Yan, F.; Liu, J.; Dong, X.; Xi, F.; Chen, P. Nanochannel-Confined Graphene Quantum Dots for Ultrasensitive Electrochemical Analysis of Complex Samples. *ACS Nano* **2018**, *12* (12), 12673–12681. https://doi.org/10.1021/acsnano.8b07564.

(308)   Zhou, L.; Hou, H.; Wei, H.; Yao, L.; Sun, L.; Yu, P.; Su, B.; Mao, L. In Vivo Monitoring of Oxygen in Rat Brain by Carbon Fiber Microelectrode Modified with Antifouling Nanoporous Membrane. *Anal. Chem.* **2019**, *91* (5), 3645–3651. https://doi.org/10.1021/acs.analchem.8b05658.

(309)   Cheng, B.; Zhou, L.; Lu, L.; Liu, J.; Dong, X.; Xi, F.; Chen, P. Simultaneous Label-Free and Pretreatment-Free Detection of Heavy Metal Ions in Complex Samples Using Electrodes Decorated with Vertically Ordered Silica Nanochannels. *Sensors Actuators B Chem.* **2018**, *259*, 364–371. https://doi.org/https://doi.org/10.1016/j.snb.2017.12.083.

(310)   Liu, Z.-G.; Chen, X.; Jia, Y.; Liu, J.-H.; Huang, X.-J. Role of Fe(III) in Preventing Humic Interference during As(III) Detection on Gold Electrode: Spectroscopic and Voltammetric Evidence. *J. Hazard. Mater.* **2014**, *267*, 153–160. https://doi.org/https://doi.org/10.1016/j.jhazmat.2013.12.054.

(311)   Peng, W.; Li, H.; Liu, Y.; Song, S. A Review on Heavy Metal Ions Adsorption from Water by Graphene Oxide and Its Composites. *J. Mol. Liq.* **2017**, *230*, 496–504. https://doi.org/https://doi.org/10.1016/j.molliq.2017.01.064.

(312)   Tibbetts, D. F.; Davis, J.; Compton, R. G. Sonoelectroanalytical Detection of Lead at a Bare Copper Electrode. *Fresenius. J. Anal. Chem.* **2000**, *368* (4), 415–417. https://doi.org/10.1007/s002160000523.

(313)   Ucun Ozel, H.; Gemici, B. T.; Gemici, E.; Ozel, H. B.; Cetin, M.; Sevik, H. Application of Artificial Neural Networks to Predict the Heavy Metal Contamination in the Bartin River. *Environ. Sci. Pollut. Res.* **2020**, *27* (34), 42495–42512. https://doi.org/10.1007/s11356-020-10156-w.

(314)   Xu, G.; Li, X.; Cheng, C.; Yang, J.; Liu, Z.; Shi, Z.; Zhu, L.; Lu, Y.; Low, S. S.; Liu, Q. Fully Integrated Battery-Free and Flexible Electrochemical Tag for on-Demand Wireless in Situ Monitoring of Heavy Metals. *Sensors Actuators B Chem.* **2020**, *310*, 127809. https://doi.org/https://doi.org/10.1016/j.snb.2020.127809.

(315)   Pungjunun, K.; Yakoh, A.; Chaiyo, S.; Siangproh, W.; Praphairaksit, N.; Chailapakul, O. Smartphone-Based Electrochemical Analysis Integrated with NFC System for the   Voltammetric Detection

of Heavy Metals Using a Screen-Printed Graphene Electrode. *Mikrochim. Acta* **2022**, *189* (5), 191. https://doi.org/10.1007/s00604-022-05281-x

Chapter 2

Chapter 2. Autonomous Sensing Boat for HMIs Detection in Natural Waters
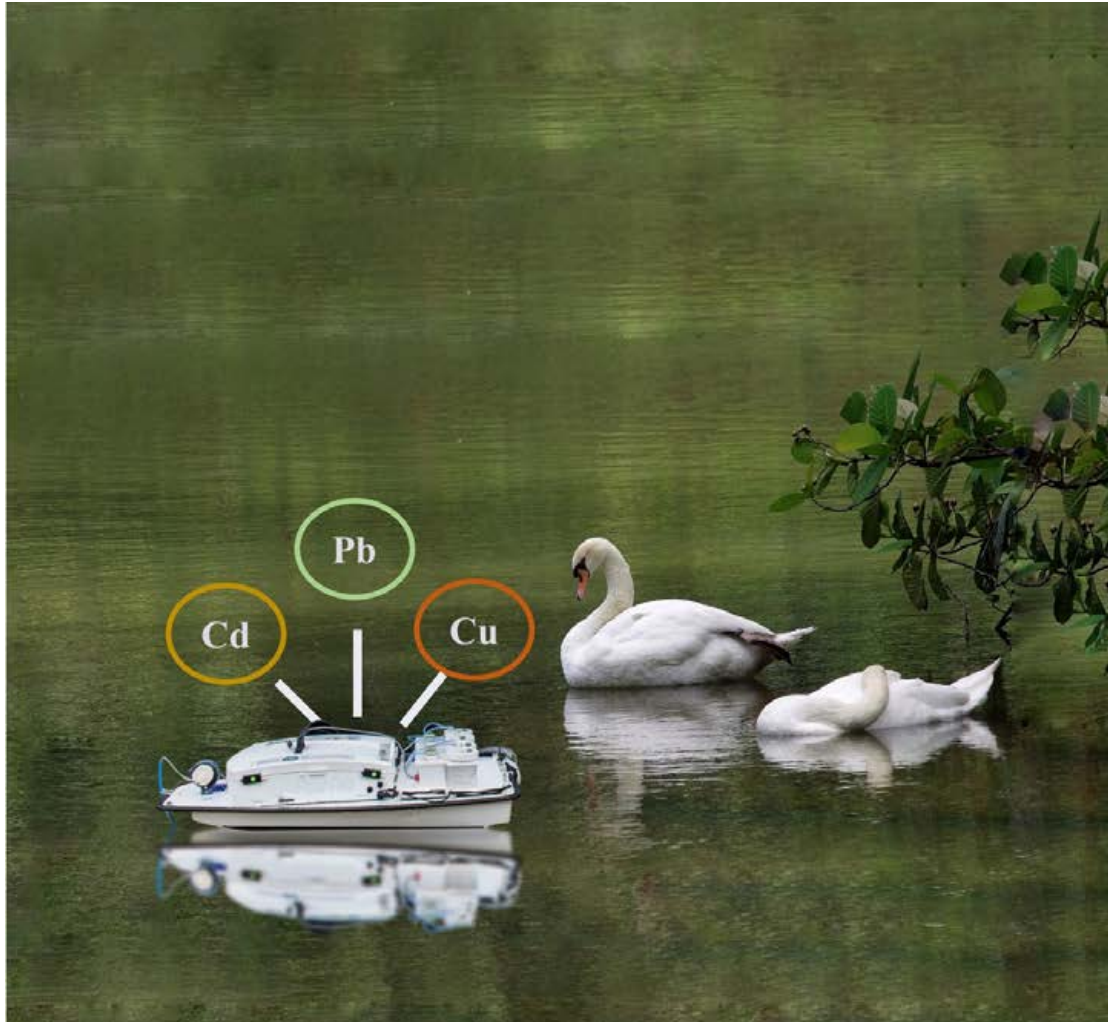

Figure 2.1 Autonomous sensing boat for HMIs detection in natural waters

Determination of the levels of HMIs would support the assessment of sources and pathways of water pollution. However, traditional spatial assessment by manual sampling and off-site detection in the laboratory is expensive and time-consuming and requires trained personnel as discussed in Chapter 1. Aiming to fill the gap between *in-situ* automatic measurements and laboratory-based techniques, we developed an autonomous sensing boat for HMIs detection using SWASV. A fluidic sensing system was developed to integrate into the boat as the critical sensing component and could detect ≤1 ppb Pb^{2+}, ≤6 ppb Cu^{2+}, and ≤71 ppb Cd^{2+} ions simultaneously in the laboratory. Once its integration was completed, the autonomous sensing boat was tested in the field, demonstrating its ability to distinguish the highest concentration of Pb^{2+} in the effluent of a galena-enriched mine compared to those at other sites in the stream (Osor Stream, Girona, Spain).

2.1 Introduction

Freshwater, a necessity for humans and other life forms, has been continuously compromised by the inclusion of heavy metal (HM) pollutants from various natural and anthropogenic processes.[1] HM pollutants in water adversely affect humans, animals, and plants due to their tendency to bioaccumulate, their biomagnification, and their environmental persistence.[2] They pose a serious threat to humans and other living organisms. According to the World Health Organization (WHO) guidelines in table 1.3.1, Pb, Cd, Cr, and other HMs must be controlled in food sources to ensure public safety.[3] The maximum permitted concentrations of Pb^{2+}, Cd^{2+}, and Cu^{2+} are 10 ppb, 3 ppb, and 2 ppm, respectively. Monitoring HM pollutants in natural waters below these low concentrations is an urgent need.

Various techniques can determine HMs quantitatively such as atomic absorption spectrometry (AAS),[4] inductively coupled plasma mass spectrometry (ICP-MS),[5] inductively coupled plasma atomic emission spectrometry (ICP-AES),[6] *etc.* They are highly accurate and quite costly and have complicated sample handling that requires bulky equipment with specialized personnel.

On the contrary, electrochemical techniques are promising due to portability, simplicity, and fast detection as discussed in subsections 1.2 and 1.3 and other review studies.[7,8] Square-wave anodic stripping voltammetry (SWASV) is one of the most typical techniques for HM detection. Herein, firstly the HM cations (M^{n+}) are concentrated and reduced on the electrode surface (to M^0) by applying a negative potential. Then, they are re-oxidized (to M^{n+}) by applying a reverse potential in square-wave pulses; in the meantime, the current and potential during the reoxidation process are recorded as a voltammogram. Consequently, the HM species and concentration could be known by the peak potential and current intensity, respectively. [9]

In-situ HM detection in a body of natural water, avoiding any pretreatment and maintaining the most original characteristics of HMs, has shown advantages compared to the traditional approaches for HM distribution assessment in waters involving manual sampling, off-site

detection, and possible contamination.[10–15] To further decrease the labor errors and cost from on-site HM measurements, several automatic sensing probes based on anodic stripping voltammetry have been reported; however, they still suffer from the low portability caused by the large size and lack of remote operation and automation, requiring humans on deck to control the movements of sensing probes between different testing sites, which induces high costs, especially in large lakes and rivers.[16–18] A fully autonomous sensing tool for *in-situ* HM measurements in natural waters has rarely been reported.

To fill this gap, we developed an autonomous sensing boat with a programmable data collection campaign to assess the spatial distribution of HM pollutants in natural waters. With the aim of automatic sampling and detection, a low-cost fluidic HM sensing system (FSS), as the key sensing component, was fabricated (Figure 2.2a). The autonomous boat was constructed on the basis of the commercial vehicle and adapted for the integration of the FSS and the corresponding electronic controlling unit (Figure 2.2b-c). Then, the sensing performance with respect to Cd^{2+}, Pb^{2+}, and Cu^{2+} of the FSS was investigated in both deionized water and river water in the laboratory. Finally, the autonomous sensing boat was examined in a mining effluent (in Osor Stream, Girona, Spain).
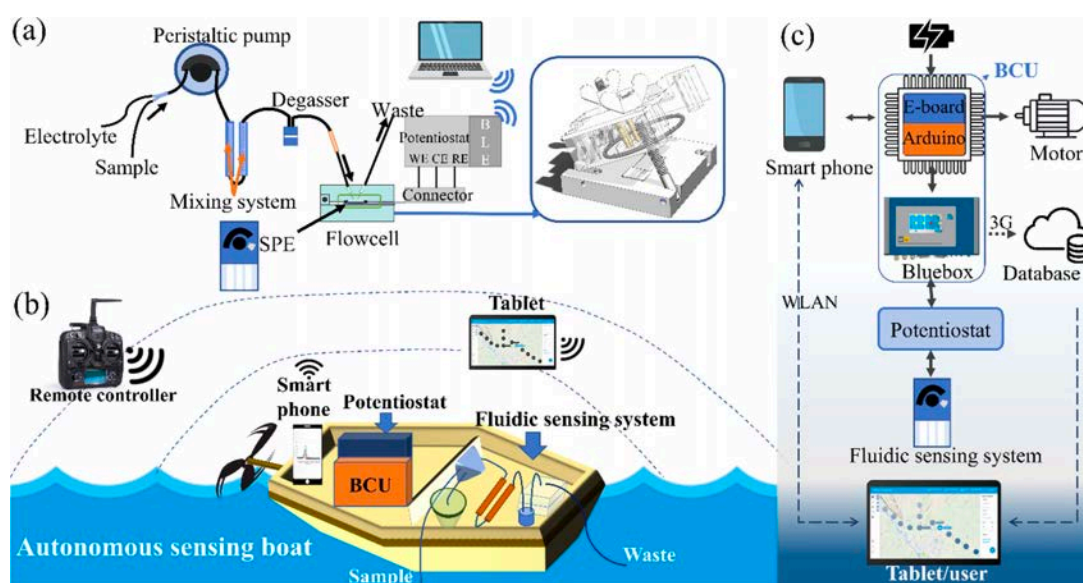

Figure 2.2 Schematic representation of (a) the FSS, including the sample, pre-stored supporting electrolyte, peristaltic pump, mixing system, degasser, flow cell (SPE inside), potentiostat, and laptop. The inset shows the open flow cell containing an SPE. (b) Autonomous sensing boat with the FSS extracting *in situ* water samples and mixing them with a supporting electrolyte in an encapsulated container (green container) in a separate compartment in case of a leakage. (c) Block diagram of the electronic controlling unit describing the architecture and connectivity of the main components.

2.2   Experimental Section

2.2.1 Reagents and Equipment

Hydrochloric acid (37%, 3203312.5L) and standard heavy metal solutions (Cd, Cu, and Pb at 1000 ppm, AAS grade) were acquired from Sigma-Aldrich. Degassers (bubble trap), tubings (three-stop Tygon), and connectors were from Darwin Microfluidics. The peristaltic pump was a model Perimax12 pump from SPETEC. The mini-potentiostat was a model EmStatBlue instrument from Palmsens. The autonomous surface vehicle (Lutra Prop Series, 1.5 m in length) powered by a lithium polymer battery (4 S, 16 Ah, 10 C, 16 V) was acquired from Platypus LLC.[19] Bluebox (BlueboxT4) was developed by GO Systemelektronik.[20] The software for HM analysis is PStrace 5.8.

2.2.2 Standard Solutions

Deionized water (18.2 MΩ cm at 25 °C, Milli-Q) was mixed with 37% HCl to prepare HCl dilutions. An individual HM solution was prepared by mixing deionized water with a single HM standard solution (1000 ppm). Mixed HM solutions were prepared with the addition of Cd^{2+}, Pb^{2+}, and Cu^{2+} simultaneously in deionized water.

2.2.3 SPCE Fabrication

Screen-printed carbon electrodes (SPCEs) were fabricated by a screen printing technique with a DEK248 printer machine (DEK, Weymouth, U.K.).[9] PET as the substrate was first cleaned with deionized water, ethanol spraying, and nitrogen purging. They were then pre-heated at 110 °C for 30 min to evaporate the cleaning solvents and prevent any deformation in the following steps. The SPCEs were fabricated in four steps. (1) Ag paste (C2180423D2 SILVER PASTE-349288, Sun Chemical) was printed to form conductive connections. (2) Then the reference electrode was printed using Ag/AgCl paste (Loctite EDAG AV458, Henkel). (3) The carbon paste was used for patterning working and counter electrodes (C2030519P4 CARBON SENSOR PASTE-267508, Sun Chemical). (4) Finally, the insulating layer was printed (D2070423P5 DIELECT PASTE GRAY, Sun Chemical). The deposited ink in each step was cured at 110 °C for 30 min in an oven after every printing process.

2.2.4 SWASV

Detecting HM ions by SWASV included three steps, *i.e.*, deposition, equilibrium, and stripping. During the deposition step, the peristaltic pump was switched on (with the range of flow rates of 1–7.5 mL/min), and a constant negative potential (deposition potential usually from −1.2 to −1 V) was applied to the WE for a deposition period (from 60 to 400 s). Then, during the equilibrium (20 s), the peristaltic pump was stopped, leaving the tested solution to be still on the surface of WE. Afterward, the potential was scanned to 0 V in square-wave pulses in a stripping step with the parameters below:

Table 2.1 The applied parameters of square-wave pulses in the stripping step

Pulse frequency	Amplitude	Potential Step
25 Hz	30 mV	6 mV

2.2.5 DATA Processing

The integral area (A) of the HM peak was denoted as the output signal instead of the peak intensity for the peak splitting that occurred when testing mixed heavy metal solutions. The limit of detection (LOD) was defined as 3 times the standard deviation of the minimum concentration with measurable results. Likewise, the limit of quantification (LOQ) was defined as 10 times the standard deviation of the minimum concentration with measurable results.[21]

2.3 Results and Discussion

2.3.1 Setup of the FSS and the Autonomous Sensing Boat

For automatic, *in-situ* sampling, mixing, and detection, a FSS was developed on the basis of the working principle of SWASV, as the key role in the sensing boat. The architecture of FSS is shown in Figure 2.2a with the full image in Figure 2.3a. The sample and pre-stored electrolyte were driven by a peristaltic pump toward the flow cell during measurements. The design of two separate inlets and the pre-stored electrolyte was intended for direct sampling. After mixing and degassing, the mixture was kept on the SPCE surface in the flow cell, where the working electrode reduced HM cations (M^{n+}) in continuous flow during the SWASV deposition step. Afterward, the testing flow was stopped during equilibrium and stripping, in which the deposited HMs on the working electrode were re-oxidized, and the voltammogram was recorded in a portable computer *via* the potentiostat.

To ensure a homogeneous mixture between the pre-stored electrolyte and the sample, we created a mixing system (Figure 2.3b) consisting of two in-series syringes filled with PDMS particles whose diameters were approximately 2 mm. The performance of this setup is shown in an online video (Movie S1.avi) in our published supporting information,[22] and one can observe how two solutions with different colors (blue and pink) were completely mixed at the end of the process. Besides, to further ensure the mixing quality, the sensing signals were compared between the automatic mixing system in the FSS and manual mixing in the next section of *HMIs Sensing Performance of the FSS and the Automatic Sensing Boat*.
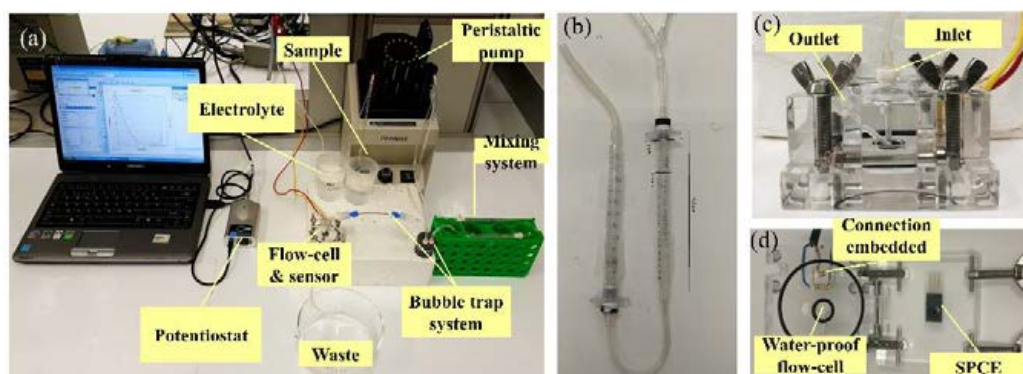

Figure 2.3. Photo of (a) the fluidic sensing system for optimization, individual detection, and simultaneous detection in the laboratory, (b) homemade mixers (12 cm × 4 cm) including two

syringes (d= 6 mm) with PDMS particles filling inside. (c) the encapsulated flowcell with the size of 6 cm × 6 cm ×3 cm including 4 screws, two pieces of PMMA, one inlet, and one outlet, and (d) the open flowcell with two o-rings with diameters of 4.2 cm, and 8 mm respectively, which limits the flow and provides a stable chamber (~ 100 μL) for electrochemical reaction and customized embedded electronic connection with SPCE and mini-potentiostat.

Due to the motion generated during the natural movement of the boat when sailing, bubbles can be introduced in the FSS, which significantly affects measurements.[23] To overcome it, a degasser was placed into the FSS before the electrochemical flow cell. To test the degassing performance, a pink-colored solution, acting as the sample, was mixed with some air intentionally (shown in an video of Movie S2.avi in our published supporting information).[22] After flowing out of the degasser, the injected air disappeared, showing the successful removal of all the bubbles inserted into the system.

The flow cell was customized as a robust electrochemical cell for HM analysis. It was designed on the basis of the FIA, mainly composed of two pieces of PMMA that enclose the SPCE with four screws (Figure 2.3c). When the SPCE and o-ring on the cover were compacted, a fixed cell was created (~100 μL), providing stable conditions for the electrochemical reaction and preventing possible leakage. The embedded electric contacts connected the SPCE with the potentiostat (Figure 2.3d), transmitting the obtained voltammogram to a data analyzer (*e.g.*, portable computer, smartphone or tablet) when the analysis had reached completion.

Once the assembly of the FSS had been completed, an autonomous boat reported in a previous study was used to equip this system.[19] The boat was originally designed to be commanded by a user *via* a tablet to navigate and monitor indicators in natural waters automatically (*e.g.*, waterline and temperature) through corresponding sensors. It was constructed by adding a Bluebox[20] (sensor control, GO Systemelektronik) to the original boat control unit (BCU) of the commercial vehicle (Lutra series, Platypus), which already includes a smartphone providing GPS data, an E-board for engine control, and operator interface (OI) software in the computer for programming the moving path. However, the proprietary E-board cannot communicate with the added Bluebox directly, interfering with data transmission from the sensor to the user. To overcome this, an Arduino Due was integrated on the E-board as the interface with Bluebox.

To further accomplish automatic sampling and *in-situ* HM analysis, we transformed this architecture by adding the developed FSS inside the upgraded one (Figure 2.2c and Figure 2.4). The mini-potentiostat and peristaltic pump of the FSS was connected to the Bluebox controlling the electrochemical reaction by working potential and sample flow. At the end of the measurement, the obtained voltammograms were analyzed by the Bluebox as the peak potential, current intensity, and integral area, which were stored with a timestamp and the corresponding GPS position in the MYSQL database by 3G technology.
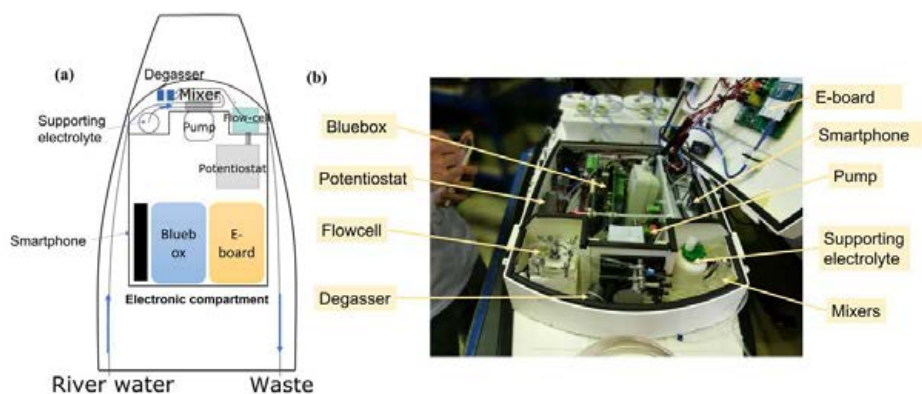
Figure 2.4 (a) Schematic illustration and a digital photograph of the autonomous boat for HMIs detection.

In addition to the upgraded hardware, to ensure a direct user interaction with the boat and data transmission, a user-friendly operator interface (OI) is necessary. First (to make it more comfortable during the testing of the campaign in a natural environment), an application of a graphic user interface (GUI), based on the open-source OI of a commercial boat, was transferred to the tablet. The smartphone read remote commands emitted by GUI and transmitted them to the E-board for engine control so that the GUI allowed users to directly program the data collection campaign (*i.e.*, defining the path that the boat should execute, the speed at which the boat should move, and the time at which to perform the sampling). Simultaneously, the GUI also allowed the user to receive the data from sensors and the status information from the battery *via* a smartphone and a boat control unit (BCU) even during a mission execution, which strongly assisted operators in regulating the boat behaviors promptly. Moreover, to improve the interaction of the user with the obtained data in the database, a Web application (named WAQUIN)[24] and a mobile application (named WASCO)[25] were developed to allow the user to access in real time with a device using a connection to the Internet (*e.g.*, smartphone, tablet, or computer), and the HM information of natural waters varying with different time and locations can be even visualized by WAQUIN/WASCO software.

In this way, the user can interact with the sensing boat, program its data collection campaign, and instruct it to drive in the desired area to perform the required measurements. After any campaign, the complete set of data (including calibration data, time, position, and voltammograms) can be transferred from the boat to users for detailed data processing.

2.3.2 HMIs Sensing Performance of the FSS and the Automatic Sensing Boat

2.3.2.1 Optimization of Important Parameters

With the concern of the sensor served in the boat for the long-time monitoring, durability and robustness are key parameters to be considered in our study. Compared to the widely reported Bi-based electrodes, carbon-based electrodes are selected in this sense, for their inertness matches our objective in this project. Moreover, when using the Bi-based electrodes,

the oxidative stripping peak of Cu is close to that of Bi, which can result in the peak overlapping issue.[26–28]

To achieve the best sensing performance, key parameters (*i.e.*, supporting electrolyte, concentration, deposition potential, flow time, and flow rate) of the FSS were optimized.

The supporting electrolytes play important roles in HMIs detection. They were optimized by detecting Cd^{2+} ions (80 ppb) using HNO_3 (0.05 M), HCl (0.05 M), and H_2SO_4 (0.025 M). Cd^{2+} ions rather than Pb^{2+} or Cu^{2+} were selected because Cd^{2+} is considered more sensitive to the influence of acids due to its reduction potential closer to that of H^+.[29] The highest signal was obtained using HCl in Figure 2.5a, and HCl was therefore chosen as the supporting electrolyte.

The concentration of HCl affects HMIs hydrolysis which is critical for deposition and stripping processes. The FSS was tested using 80 ppb Cd^{2+} in HCl solutions at a variety of concentrations. More concentrated HCl causes more free ions, which is beneficial for detection until saturation (Figure 2.5b). The concentration of HCl would also influence the simultaneous HM detection. To study it, mixed HMIs of 20 ppb Cu^{2+}, 20 ppb Pb^{2+}, and 80 ppb Cd^{2+} in different concentrations of HCl (0.01 - 0.20 M) were detected. As shown in Figure 2.5c-d, 0.05 M of HCl supported the best signals of Pb^{2+} and Cu^{2+} with obvious separation between their peaks and a detectable signal of Cd^{2+}. Thus, 0.05M of HCl was applied as the supporting electrolyte.
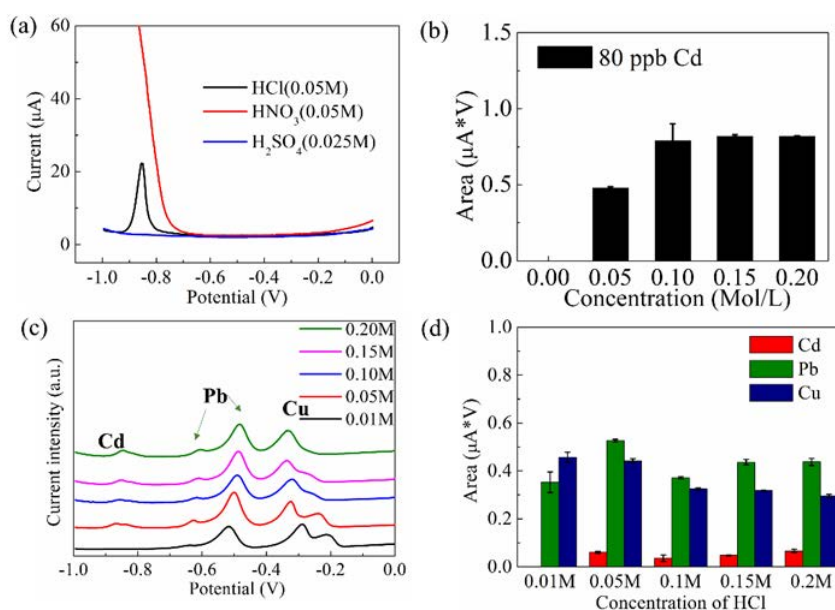

Figure 2.5 (a) Voltammograms and (b)diagram of integral peak area of 80ppb Cd in different supporting electrolytes. (c) Voltammograms and (d) diagrams of Cd^{2+}, Pb^{2+}, and Cu^{2+} in mixed solution with 80 ppb Cd^{2+}, 20 ppb Cu^{2+}, and 20 ppb Cd^{2+} in different concentrations of HCl solutions.

Moreover, there is a general agreement between the increase in flow rate/time and the increase of sensing signals. However, the limited volume of HCL solution during *in-situ*

measurements would not support a high flow rate or long flow time. To investigate the optimum flow condition, Cd^{2+} at the concentration of 80 ppb was detected using different flow rates (Figure 2.6a,b). The sensing signal increased non-linearly with an increasing flow rate from 0 to 7.5 mL/min. An optimized flow rate of 3 mL/min was kept for all further measurements due to the following reasons (1) as it shows good Cd^{2+} sensing signals with the smallest standard deviation (Figure 2.6b) and further increase of flow rate does not show a linear response and (2) the autonomous boat has limited space, unable to be equipped with a big amount of supporting electrolyte. Hence, 3 ml/min was chosen as the optimized flow rate.

Similarly, different flow time (deposition time) from 60 to 400s for the detection of Cd^{2+} (80 ppb) was tested. The results showed a linear relationship between the deposition time and sensing signals. The deposition time of 200s was selected as it showed obvious signals with the smallest standard deviation (Figure 2.6c-d). Moreover, it is a good compromise considering the limited analysis time on the autonomous sensing boat. For example, the deposition time of 200s can handle a maximum of 30 measurements in 2 hours including the pre-calibration and *in-situ* measurements for 5 different tested sites (n=3).
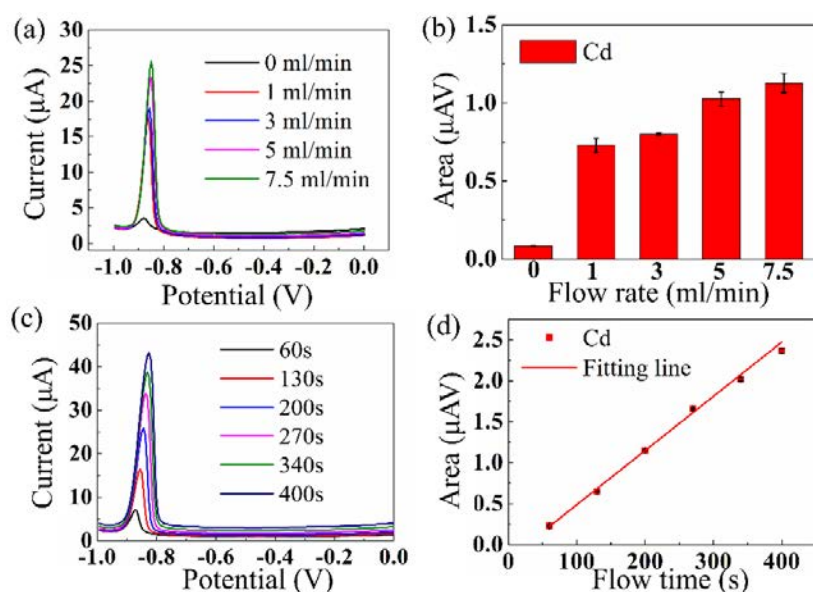

Figure 2.6 (a) Stripping voltammograms and (b) diagrams toward detecting 80 ppb Cd^{2+} with different flow rates. (c) Stripping voltammograms and (d) diagrams upon detecting 80 ppb Cd^{2+} with different flowtime.

Furthermore, applying more negative deposition potential would facilitate cations' deposition and enhance the sensing signals; however, it could induce the bubbles generating on the WE surface due to hydrogen evolution reaction.[30] The bubbles could cause damage to the sensor and irreproducible signals. As our observation, the negative potential (deposition potential ≤ -1.1 V) facilitated bubble generation within the flow cell. For the robustness of the whole system, more negative potentials were not applied in following experiments. On the

other hand, Cd^{2+} ions were undetectable when the deposition potential was below -0.9 V (Figure 2.7). The deposition potential of -1.0 V was therefore chosen.

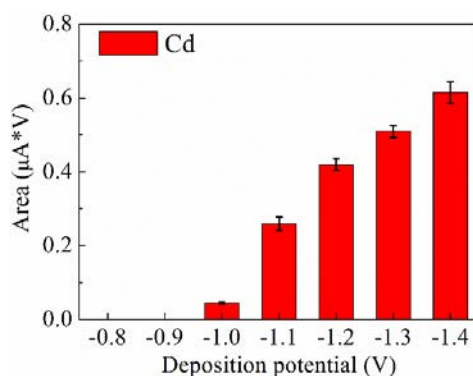Figure 2.7 Diagram of Cd in a mixed solution of 80ppb Cd^{2+}, 20ppb Cu^{2+} ,and 20 ppb Cd^{2+} ions with different deposition potential.

In summary, the optimized parameters are summarized in Table 2.2.

Table 2.2 Optimized parameters of the FSS for HMIs detection

Supporting electrolyte	Concentration	Deposition potential	Flowtime	Flowrate
HCl	0.05 M	-1.0 V	200s	3 ml/min

2.3.2.2　FSS Tested in Standard Heavy Metal Solutions in Deionized Water in Laboratory

First, to further ensure the automatic mixing system in the FSS has comparative HMIs sensing performance with the conventional manual mixing, Pb^{2+} standard solution (80 ppb) was pumped into the FSS without any electrochemical measurements. The solution entered from one inlet, with the supporting electrolyte being pumped into the other inlet, and when the mixed solution flowed out of the FSS, the solution was collected at the outlet (named Solution_Auto). To reach the same optimized concentration of HCl (0.05 M) with the Solution_Auto, the Pb^{2+} solution was acidified by HCl manually using a micropipette and a vortex mixer (Solution_Mano).

Then, these two solutions were tested by two SPCEs *via* direct dropping and the results are shown in Table 2.3. As expected, the sensing signals (Integral Area) showed that there is a negligible difference (3.3%) between the signals by manual and automatic mixing .

Table 2.3. Comparison of the sensing signals tested by SPCE for the solutions before and after the fluidic sensing system (n=5)

	Integral Area (μAV)
Solution_Mano	0.118±0.0100
Solution_Auto	0.122±0.0124

Then, the FSS was tested with individual HM standard solutions (Cd^{2+}, Pb^{2+}, and Cu^{2+}) separately (Figure 2.8). The responses toward Cd^{2+} and Cu^{2+} had linear relation with varied concentrations ($R^2 > 0.90$). Regarding Pb^{2+}, the linearity obtained was not as good as the other two ($R^2 = 0.90$, Figure 2.8), which could be caused by the inhomogeneous deposition of Pb^{2+} onto the carbon paste electrode surface as reported elsewhere.[31] The estimated LOD was at the ppb level: 7 ppb for Cd^{2+}, 1 ppb for Pb^{2+}, and 0.3 ppb for Cu^{2+}. The LOQ of Cd^{2+}, Pb^{2+}, and Cu^{2+} were 23, 6, and 1 ppb, respectively.
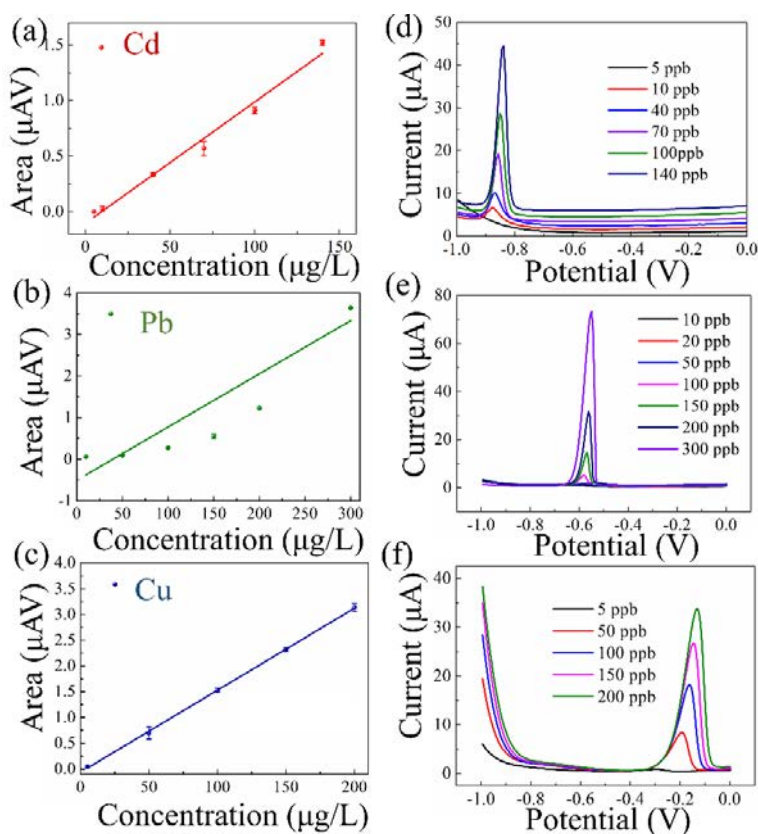

Figure 2.8. The calibration lines and stripping voltammograms of Cd (a, d), Pb (b,e) and Cu (c,f), respectively in individual HM detection. The fitting lines of Cd, Pb and Cu are $y_{Area}=0.010 \, x_{Conc.}-0.10$ ($R^2=0.98$), $y_{Area}=0.013 \, x_{Conc.}-0.50$ ($R^2=0.91$), and $y_{Area}=0.016 \, x_{Conc.}-0.063$ ($R^2=0.99$), respectively.

To investigate the sensing performance toward multi-HM contaminants, the FSS was tested in the standard solutions containing mixed Cd^{2+}, Pb^{2+}, and Cu^{2+}. Compared with individual measurements, as expected, the simultaneous detection demonstrated the difference in sensitivity and LOD due to the mutual interference. The presence of Pb^{2+} and Cu^{2+} ions decreased the Cd^{2+} sensitivity drastically with a LOD of 71 ppb (Figure 2.9). It could be attributed to the more negative potential required for Cd^{2+} ions to deposit compared to Pb^{2+} and Cu^{2+}, which induces substance loss on the WE and the ions' competition when co-depositing as we have discussed in Chapter 1.3. However, Pb^{2+} and Cu^{2+} were negligibly

affected showing the LOD of 1 and 6 ppb, respectively, both being below the minimum concentration required by WHO guidelines (10 ppb and 2 ppm for Pb and Cu, respectively).
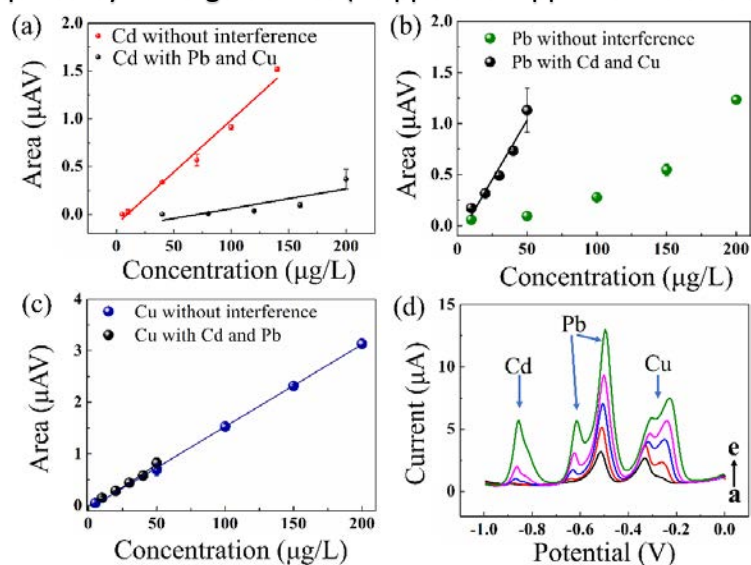

Figure 2.9. The calibration curves of (a) Cd^{2+} (b) Pb^{2+} and (c) Cu^{2+} with and without the other two HMs as interferents, and (d) the corresponding stripping voltammograms.

The robustness of the FSS is crucial for the sensing boat; therefore, the FSS was investigated in terms of repeatability, stability, and reproducibility. The reproducibility (relative standard deviation, RSD) of nine different SPCEs upon the simultaneous detection of Cd^{2+}, Pb^{2+}, and Cu^{2+} were 19.57%, 3.86%, and 4.73%, respectively. The repeatability toward Cd^{2+}, Pb^{2+}, and Cu^{2+} are acceptable (RSD < 20%) in 28 continuous measurements. Moreover, the FSS showed the sensing signals dependence with time, demonstrating good stability within 2 h (RSD < 20%).

2.3.2.3   HMIs Detection by the FSS in Real Sample

First, we tested the FSS in real river sample spike with of 180 ppb Cd^{2+}, Cu^{2+} and Pb^{2+}. We observed that the river water matrix may decrease some sensing signals compared to the ones in deionized water which are shown in Table 2.4.

Table 2.4. Sensing signals of Cd^{2+}, Pb^{2+} and Cu^{2+} in their mixed standard solution (deionized water) and spiked Ter River water with the same known concentration (180 ppb).

	Cd	Pb	Cu
Deionized water	0.023 ± 0.0059	2.51 ± 0.15	2.84 ± 0.12
River water	0.031 ± 0.0044	0.98 ± 0.019	1.58 ± 0.13

To overcome the inaccuracy, the calibration in deionized water was discarded; instead, the standard addition method was harnessed, in which the surface water from a specific testing site, would be spiked with a series of standard heavy metal solutions with different and known concentrations to construct the calibration corresponding to the water matrix at the testing area. For this reason, the surface water from the target river or lake (with its unique condition

e.g. pH, organic matters, and other ions) is highly recommended to be used to do pre-calibration first to achieve better accuracy. Hence, using the calibration in the desired water matrix could diminish the variation from the matrix effect.

Hence, the FSS was conducted with real surface water by spiking known concentrations of Cd^{2+}, Pb^{2+}, and Cu^{2+} (Ter River, Vic, Spain) as a standard addition calibration. The FSS demonstrated good linear responses to the varying concentration (Figure 2.10 a–c) with the LOD of Cd^{2+}, Pb^{2+}, and Cu^{2+} at 99, 0.3, and 3 ppb, respectively.
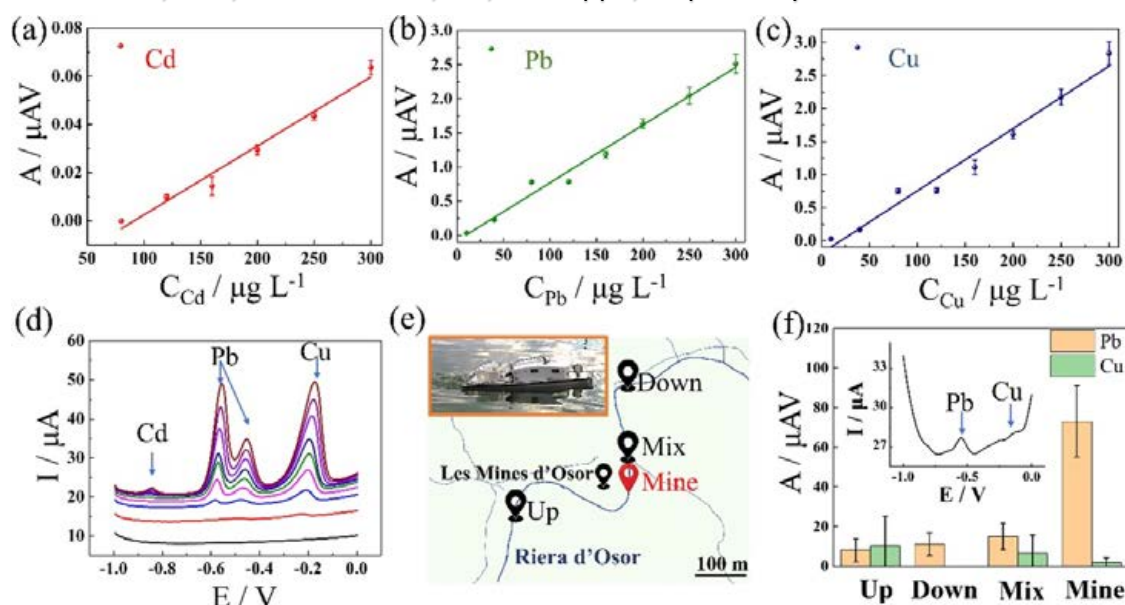

Figure 2.10 (a–c) Plots of peak area vs concentration in simultaneous measurements for Cd^{2+}, Pb^{2+}, and Cu^{2+}, respectively, in a spiked river sample in the laboratory. (d) Corresponding stripping voltammograms of the simultaneous measurements in spiked river samples in the laboratory. (e) Schematic illustration of the boat navigating in a campaign experiment. The inset shows a digital photograph of the boat navigating an area in a river. (f) Determination of Pb^{2+} and Cu^{2+} in a campaign experiment. The inset shows a voltammogram obtained in a mine effluent sample, in which a Pb peak centered at −0.5 V can be clearly distinguished.

As such, we involved the measured sensing signals of 180 ppb Pb^{2+}, Cu^{2+}, and Cd^{2+} in the same water matrix (Ter River water) in Table 2.4. Since the water matrix calibration was already achieved (Figure 2.10), the calculated concentration was compared to its theoretical value. The recovery of Cd^{2+}, Pb^{2+}, and Cu^{2+} is 109%, 113%, and 104%, respectively.

Table 2.5. The recovery of Cd^{2+}, Pb^{2+}, and Cu^{2+} (180 ppb) spiked with Ter River water by the FSS.

	Calibration Equation	R^2	Tested signals (μAV) (Y)	Calculated Conc.(ppb) (X)	Spiking Conc.(ppb)	Accuracy
Cd	y=0.00029x-0.025	0.930	0.031±0.0044	197.5	180	109%

Pb	y=0.0085x-0.76	0.984	0.98±0.019	204.4	180	113%
Cu	y=0.0094x-0.19	0.969	1.58±0.13	188.3	180	104%

* The sensing range of Cd was used as 120-300 ppb to reach better R^2 (> 0.90)

Lastly, with the question how the automatic sensing boat performed in the natural environment, we conducted campaign experiments in a stream affected by the input of an abandoned mine effluent (Osor Stream, Ter River, Girona, Spain). Figure 2.10e shows the programmable boat path from the upstream to downstream in the stream course. Intuitively, the inset of Figure 2.10e is the scenario of the boat (approximately 1.5 m in length) navigating under a programmed path automatically, and an online video (Movie S3.avi) shows the boat navigating in a larger body of water (Ebro River, Spain) in our published supporting information.[22]

To further test the HM sensing ability, the automatic sensing boat was instructed to drive into the mine effluent (Figure 2.10e), which was influenced by the drainage from the enriched-galena Osor mine (Les Mines d'Osor, 41°57′0″ north, 2°35′30″ east). Unfortunately, the *in-situ* analysis was disturbed because the dynamic hydro morphology in the mine effluent (*e.g.*, changing water flow and whirlpool) consumed much more time and power of the automatic boat, which is beyond expectation. The disturbance could be ascribed to the fact that the navigation routine in the GUI was not optimized on the basis of the specific river condition, and the boat has relatively low intelligence to respond to sudden uncertainties at this stage, which leaves an open challenge for future research. Alternatively, in our study, we instructed the sensing boat to collect samples from several sampling sites (up, mix, mine, and down) and analyzed them by the same sensing boat on shore.

The voltammogram (Figure 2.10f, inset) of the mine effluent sample showed one clear peak centered at −0.6 V that can be identified as Pb^{2+} by its peak potential, and a negligible peak at −0.2 V could be attributed to Cu^{2+}. Figure 2.10f demonstrates enhancement in the Pb signal in the mine sample compared to the results from the rest of the stream (up, mix, and down), whereas Cu^{2+} in the mine sample possessed similar sensing signals to those in other samples. It indicates that in the mine effluent there are more concentrated Pb^{2+} ions; however, Cu^{2+} ions have similar concentrations in all testing sites. These results are consistent with a previous study of HMIs in Mine Osor, in which the concentration of various HMIs in the soil sample was characterized by ICP-MS. The results showed that the sample collected from the location (OS-6 in the previous study), adjacent to our testing site, had much higher (two orders of magnitude) concentrations of Pb^{2+}, Zn^{2+}, and Ba^{2+} than the rest of the HMIs (*e.g.*, Cd^{2+} and Cu^{2+}), which could originate from the F–Ba–Pb–Zn mine vein.[32] Hence, the detected Pb^{2+} ions with a higher concentration in the mine effluent could be attributed to the drainage and leaching from Mine Osor to surface water, and Cu^{2+}, not abundant in the mine, thus remains at a low concentration like the other sites. However, with regard to Cd^{2+}, it is difficult

to detect it, because the concentration of Cd^{2+} is not only relatively low in the mine effluent but also the high LOD toward Cd^{2+} of the FSS affected by mutual interference cannot reach the high sensitivity in the condition of multiple HMIs. Moreover, Zn^{2+} and Ba^{2+} as the interferents at high concentrations did not influence the detection without showing any peaks in the voltammogram for their stripping potential (−1.2 and −2.1 V for Zn^{2+} and Ba^{2+}, respectively) was beyond the working potential (from 0 to −1 V).[33,34]

These results suggest the autonomous sensing boat in our study has the ability to analyze the HMIs at different concentrations in contaminated water. Compared to the reported studies of an automatic on-site sensing probe based on ASV, the autonomous boat has advantages in being fully automated and high portable because of its compact design and small size. [16–18,35] Simultaneous detection can be realized with one SPCE sensor with estimated cost of €0.16 (calculated on the basis of material cost) in the FSS (approximately €2000 on material cost) without the need for photolithography, which may have a future impact in resource-limited regions.

Even though in this study, the *in-situ* measurement in Osor Stream was not operated successfully, a deeper exploration of the outdoor validation of this autonomous sensing boat and quantitative analysis has been summarized and published in our other study.[36]

2.4   Conclusion

In this work, the autonomous sensing boat integrated with the FSS was fabricated for HM spatial monitoring in waters based on SWASV. The FSS, as the most important component in the automatic boat, was first tested in the laboratory. The LODs toward Cd^{2+}, Pb^{2+}, and Cu^{2+} were at ppb level in both individual and simultaneous measurements. It was then adapted into an engineered autonomous boat. To investigate the performance, the autonomous sensing boat was tested during a campaign, and it could navigate under a programmable path automatically and distinguish the highest concentration of Pb^{2+} in the effluent of the galena-enriched mine compared to other sites in the stream. Even though at this stage there are some issues (*e.g.*, the high LOD toward Cd^{2+} caused by mutual interference and possible disturbance by uncertainties in the natural environment as an open challenge for the research community in the future), it is the first autonomous boat operating simultaneous multi-HMIs detection by ASV, which may have a future impact in environmental control. Moreover, compared to the reported *in-situ* and automatic sensing tools, it has the advantages of being small, automated, portable, and cost-effective, which sheds light on pollution control, especially in resource-limited regions.

Reference

(1)   Barton, J.; García, M. B. G.; Santos, D. H.; Fanjul-Bolado, P.; Ribotti, A.; McCaul, M.; Diamond, D.; Magni, P. Screen-Printed Electrodes for Environmental Monitoring of Heavy Metal Ions: A Review. *Microchim. Acta* **2016**, *183* (2), 503–517. https://doi.org/10.1007/s00604-015-1651-0.

(2)   Maria Csuros. *Environmental Sampling and Analysis for Technicians*, 1st Editio.; 1994.

(3)   World Health Organization. Guidelines for drinking-water quality, 4th ed., incorporating the 1st addendum (chapters) https://www.who.int/publications/i/item/9789241549950.

(4)   Zhou, G.; Luo, J.; Liu, C.; Chu, L.; Ma, J.; Tang, Y.; Zeng, Z.; Luo, S. A Highly Efficient Polyampholyte Hydrogel Sorbent Based Fixed-Bed Process for Heavy Metal Removal in Actual Industrial Effluent. *Water Res.* **2016**, *89*, 151–160. https://doi.org/https://doi.org/10.1016/j.watres.2015.11.053.

(5)   Bua, D. G.; Annuario, G.; Albergamo, A.; Cicero, N.; Dugo, G. Heavy Metals in Aromatic Spices by Inductively Coupled Plasma-Mass Spectrometry. *Food Addit. \& Contam. Part B* **2016**, *9* (3), 210–216. https://doi.org/10.1080/19393210.2016.1175516.

(6)   Zhao, Y.; Li, Z.; Ross, A.; Huang, Z.; Chang, W.; Ou-yang, K.; Chen, Y.; Wu, C. Determination of Heavy Metals in Leather and Fur by Microwave Plasma-Atomic Emission Spectrometry. *Spectrochim. Acta Part B At. Spectrosc.* **2015**, *112*, 6–9. https://doi.org/https://doi.org/10.1016/j.sab.2015.06.017.

(7)   Aragay, G.; Pons, J.; Merkoçi, A. Recent Trends in Macro-, Micro-, and Nanomaterial-Based Tools and Strategies for Heavy-Metal Detection. *Chem. Rev.* **2011**, *111* (5), 3433–3458. https://doi.org/10.1021/cr100383r.

(8)   Bansod, B. K.; Kumar, T.; Thakur, R.; Rana, S.; Singh, I. A Review on Various Electrochemical Techniques for Heavy Metal Ions Detection with Different Sensing Platforms. *Biosens. Bioelectron.* **2017**, *94* (March), 443–455. https://doi.org/10.1016/j.bios.2017.03.031.

(9)   Güell, R.; Aragay, G.; Fontàs, C.; Anticó, E.; Merkoçi, A. Sensitive and Stable Monitoring of Lead and Cadmium in Seawater Using Screen-Printed Electrode and Electrochemical Stripping Analysis. *Anal. Chim. Acta* **2008**, *627* (2), 219–224. https://doi.org/10.1016/j.aca.2008.08.017.

(10)   Long, F.; Zhu, A.; Shi, H.; Wang, H.; Liu, J. Rapid On-Site/*in-Situ* Detection of Heavy Metal Ions in Environmental Water Using a Structure-Switching DNA Optical Biosensor. *Sci. Rep.* **2013**, *3* (1), 2308. https://doi.org/10.1038/srep02308.

(11)   Guo, J.; Zhou, M.; Yang, C. Fluorescent Hydrogel Waveguide for On-Site Detection of Heavy Metal Ions. *Sci. Rep.* **2017**, *7* (1), 7902. https://doi.org/10.1038/s41598-017-08353-8.

(12)   Lin, Y.; Gritsenko, D.; Feng, S.; Teh, Y. C.; Lu, X.; Xu, J. Detection of Heavy Metal by Paper-Based Microfluidics. *Biosens. Bioelectron.* **2016**, *83*, 256–266. https://doi.org/https://doi.org/10.1016/j.bios.2016.04.061.

(13)   Biyani, M.; Biyani, R.; Tsuchihashi, T.; Takamura, Y.; Ushijima, H.; Tamiya, E.; Biyani, M. DEP-On-Go for Simultaneous Sensing of Multiple Heavy Metals Pollutants in Environmental Samples. *Sensors* . 2017. https://doi.org/10.3390/s17010045.

(14)   Xiao, M.; Liu, Z.; Xu, N.; Jiang, L.; Yang, M.; Yi, C. A Smartphone-Based Sensing System for On-Site Quantitation of Multiple Heavy Metal Ions Using Fluorescent Carbon Nanodots-Based Microarrays. *ACS Sensors* **2020**, *5* (3), 870–878. https://doi.org/10.1021/acssensors.0c00219.

(15) Borrill, A. J.; Reily, N. E.; Macpherson, J. V. Addressing the Practicalities of Anodic Stripping Voltammetry for Heavy Metal Detection: A Tutorial Review. *Analyst* **2019**, *144* (23), 6834–6849. https://doi.org/10.1039/C9AN01437C.

(16) Tercier-Waeber, M.-L.; Confalonieri, F.; Abdou, M.; Dutruch, L.; Bossy, C.; Fighera, M.; Bakker, E.; Graziottin, F.; van der Wal, P.; Schäfer, J. Advanced Multichannel Submersible Probe for Autonomous High-Resolution in Situ Monitoring of the Cycling of the Potentially Bioavailable Fraction of a Range of Trace Metals. *Chemosphere* **2021**, *282*, 131014. https://doi.org/https://doi.org/10.1016/j.chemosphere.2021.131014.

(17) Tercier-Waeber, M.-L.; Abdou, M.; Fighera, M.; Kowal, J.; Bakker, E.; van der Wal, P. In Situ Voltammetric Sensor of Potentially Bioavailable Inorganic Mercury in Marine Aquatic Systems Based on Gel-Integrated Nanostructured Gold-Based Microelectrode Arrays. *ACS Sensors* **2021**, *6* (3), 925–937. https://doi.org/10.1021/acssensors.0c02111.

(18) Wang, N.; Kanhere, E.; Kottapalli, A. G. P.; Miao, J.; Triantafyllou, M. S. Flexible Liquid Crystal Polymer-Based Electrochemical Sensor for *in-Situ* Detection of Zinc(II) in Seawater. *Microchim. Acta* **2017**, *184* (8), 3007–3015. https://doi.org/10.1007/s00604-017-2280-6.

(19) Steccanella, L.; Bloisi, D. D.; Castellini, A.; Farinelli, A. Waterline and Obstacle Detection in Images from Low-Cost Autonomous Boats for Environmental Monitoring. *Rob. Auton. Syst.* **2020**, *124*, 103346. https://doi.org/https://doi.org/10.1016/j.robot.2019.103346.

(20) GO Systemelektronik. The BlueBox System https://www.go-sys.de/en/bluebox/.

(21) Kang, W.; Pei, X.; Rusinek, C. A.; Bange, A.; Haynes, E. N.; Heineman, W. R.; Papautsky, I. Determination of Lead with a Copper-Based Electrochemical Sensor. *Anal. Chem.* **2017**, *89* (6), 3345–3352. https://doi.org/10.1021/acs.analchem.6b03894.

(22) Yang, Q.; Nagar, B.; Alvarez-Diduk, R.; Balsells, M.; Farinelli, A.; Bloisi, D.; Proia, L.; Espinosa, C.; Ordeix, M.; Knutz, T.; De Vito-Francesco, E.; Allabashi, R.; Merkoçi, A. Development of a Heavy Metal Sensing Boat for Automatic Analysis in Natural Waters Utilizing Anodic Stripping Voltammetry. *ACS ES&T Water* **2021**. https://doi.org/10.1021/acsestwater.1c00192.

(23) Pereiro, I.; Fomitcheva Khartchenko, A.; Petrini, L.; Kaigala, G. V. Nip the Bubble in the Bud: A Guide to Avoid Gas Nucleation in Microfluidics. *Lab Chip* **2019**, *19* (14), 2296–2314. https://doi.org/10.1039/C9LC00211A.

(24) Intcatch. Catchments public data.

(25) Google Play. Intcatch-WASCO mobile application.

(26) Wang, J.; Lu, J.; Hocevar, S. B.; Farias, P. A. M.; Ogorevc, B. Bismuth-Coated Carbon Electrodes for Anodic Stripping Voltammetry. *Anal. Chem.* **2000**, *72* (14), 3218–3222. https://doi.org/10.1021/ac000108x.

(27) Thanh, N. M.; Van Hop, N.; Luyen, N. D.; Phong, N. H.; Tam Toan, T. T. Simultaneous Determination of Zn(II), Cd(II), Pb(II), and Cu(II) Using Differential Pulse Anodic Stripping Voltammetry at a Bismuth Film-Modified Electrode. *Adv. Mater. Sci. Eng.* **2019**, *2019*, 1826148. https://doi.org/10.1155/2019/1826148.

(28) Brainina, K. .; Stozhko, N. Y.; Belysheva, G. M.; Inzhevatova, O. V; Kolyadina, L. I.; Cremisini, C.; Galletti, M. Determination of Heavy Metals in Wines by Anodic Stripping Voltammetry with Thick-Film Modified Electrode. *Anal. Chim. Acta* **2004**, *514* (2), 227–234. https://doi.org/https://doi.org/10.1016/j.aca.2004.03.047.

(29)   Zhai, Z.; Huang, N.; Zhuang, H.; Liu, L.; Yang, B.; Wang, C.; Gai, Z.; Guo, F.; Li, Z.; Jiang, X. A Diamond/Graphite Nanoplatelets Electrode for Anodic Stripping Voltammetric Trace Determination of Zn(II), Cd(II), Pb(II) and Cu(II). *Appl. Surf. Sci.* **2018**, *457* (June), 1192–1201. https://doi.org/10.1016/j.apsusc.2018.06.266.

(30)   Bondue, C. J.; Graf, M.; Goyal, A.; Koper, M. T. M. Suppression of Hydrogen Evolution in Acidic Electrolytes by Electrochemical CO2 Reduction. *J. Am. Chem. Soc.* **2021**, *143* (1), 279–285. https://doi.org/10.1021/jacs.0c10397.

(31)   Honeychurch, K. C.; Hart, J. P.; Cowell, D. C. Voltammetric Behavior and Trace Determination of Lead at a Mercury-Free Screen-Printed Carbon Electrode. *Electroanalysis* **2000**, *12* (3), 171–177. https://doi.org/https://doi.org/10.1002/(SICI)1521-4109(200002)12:3<171::AID-ELAN171>3.0.CO;2-Q.

(32)   Bori, J.; Vallès, B.; Navarro, A.; Riva, M. C. Ecotoxicological Risks of the Abandoned F–Ba–Pb–Zn Mining Area of Osor (Spain). *Environ. Geochem. Health* **2017**, *39* (3), 665–679. https://doi.org/10.1007/s10653-016-9840-2.

(33)   Jothimuthu, P.; Wilson, R. A.; Herren, J.; Pei, X.; Kang, W.; Daniels, R.; Wong, H.; Beyette, F.; Heineman, W. R.; Papautsky, I. Zinc Detection in Serum by Anodic Stripping Voltammetry on Microfabricated Bismuth Electrodes. *Electroanalysis* **2013**, *25* (2), 401–407. https://doi.org/https://doi.org/10.1002/elan.201200530.

(34)   Ridgway, S.; Wajrak, M. Development of an In-Field Method for the Detection of Barium in Various Water Samples Using Differential Pulse Anodic Stripping Voltammetry. *Int. J. Electrochem.* **2019**, *2019*, 5813492. https://doi.org/10.1155/2019/5813492.

(35)   Lv, Z.-L.; Qi, G.-M.; Jiang, T.-J.; Guo, Z.; Yu, D.-Y.; Liu, J.-H.; Huang, X.-J. A Simplified Electrochemical Instrument Equipped with Automated Flow-Injection System and Network Communication Technology for Remote Online Monitoring of Heavy Metal Ions. *J. Electroanal. Chem.* **2017**, *791*, 49–55. https://doi.org/https://doi.org/10.1016/j.jelechem.2017.03.012.

(36)   De Vito-Francesco, E.; Farinelli, A.; Yang, Q.; Nagar, B.; Álvarez, R.; Merkoçi, A.; Knutz, T.; Haider, A.; Stach, W.; Ziegenbalg, F.; Allabashi, R. An Innovative Autonomous Robotic System for On-Site Detection of Heavy Metal Pollution Plumes in Surface Water. *Environ. Monit. Assess.* **2022**, *194* (2), 122. https://doi.org/10.1007/s10661-021-09738-z.